

# **Enhancing Corrosion Performance of Laser Modified NiTi Shape Memory Alloy**

by

Andrew Michael

A thesis  
presented to the University of Waterloo  
in fulfillment of the  
thesis requirement of the degree of  
Master of Applied Science  
in  
Mechanical Engineering

Waterloo, Ontario, Canada, 2014

© Andrew Michael 2014

I hereby declare that I am the sole author of this thesis. This is a true copy of the thesis, including any required final revisions, as accepted by my examiners.

Andrew Michael

I understand that my thesis may be made electronically available to the public.

Andrew Michael

## Abstract

Laser processing of NiTi shape memory alloys (SMA) has been identified as having great potential in surface treatment, welding, and novel performance requirement applications. However, discrepancies arise regarding whether laser processing improves or degrades the corrosion performance of NiTi-based SMAs. This is a cause for concern over the reliability of the laser processed surfaces. Prior to full scale implementation, a better understanding of oxide evolution during laser processing is required.

The first part of this study concerned a systematic investigation of the surface of Ni-44.2 wt.% Ti SMA after the application of differing amounts of laser pulsing and thus energy input. Specific focus was directed on characterizing local changes in the surface oxide adjacent to laser spots. The sample local electrochemical characteristics were investigated by scanning electrochemical microscopy (SECM). The effect of laser processing on the regeneration kinetics of the redox-active mediator was analyzed through microelectrode current maps and approach curves in the feedback mode. Raman spectroscopy was used to determine the crystallinity of the oxide and potentiodynamic cyclic polarization was used to determine oxide stability. Results showed that for a small number of pulses (*i.e.* low total energy input) corrosion performance was determined primarily by topographical effects. However, increasing the number of pulses (*i.e.* higher total energy input) had a significant impact on the stability of the oxide in the heat-affected zone (HAZ) region due to the increase in crystallinity, which dictated where the corrosion initiated.

In the second part of this study, post-process surface treatments that could be applied to NiTi SMA after laser processing were systematically investigated. Specific focus was directed at characterizing the crystallinity of the newly formed oxides and the stability across the entire surface (containing laser-processed regions and retained base material). Raman spectroscopy and potentiodynamic cyclic polarization were used for this analysis. Results showed that the post-process surface treatments successfully restored the corrosion performance to pre-laser-processing conditions by eliminating crystallinity in the surface oxide and reducing inhomogeneity across the surface.

## **Acknowledgements**

I would like to thank my supervisor, Dr. N. Zhou, for his support, guidance, and insightful advice throughout my research. The autonomy to aim my own research and the direct connection to industrial applications kept me motivated to succeed.

I would also like to thank the current and past members of the microwelding group: Dr. Ibraheem Khan, Dr. Andrew Pequegnat, Sui Kei Tang, Jeff Wang and Boyd Panton, as well as all the students in the Center for Advanced Materials Joining. I would like to give a special thanks to Andrew for his help with revisions to my first journal paper, which can be found in chapter 4 of this thesis.

I would also like to thank the Mauzeroll Research group at McGill University in Montreal, Quebec for the collaboration they have done on the SECM analysis of the NiTi surfaces. I would like to give special thanks to Dr. Ushula Tefashe for his unrelenting dedication to collaboration project and his help with my first journal paper, which can be found in chapter 4 of this thesis.

This work had been supported by the Canadian Foundation for Innovation (CFI) and the Natural Science and Engineering Research Council of Canada (NSERC).

To my family.

But especially to my fiancée, whose undying support helped me achieve my goals

# Table of Contents

DECLARATION .....	II
ABSTRACT .....	III
ACKNOWLEDGEMENTS .....	IV
DEDICATION .....	V
TABLE OF CONTENTS .....	VI
LIST OF FIGURES.....	IX
LIST OF TABLES.....	XIII
LIST OF EQUATIONS.....	XIV
<b>CHAPTER 1:INTRODUCTION .....</b>	<b>1</b>
1.1 BACKGROUND.....	1
1.2 LASER PROCESSING OF NiTi .....	1
1.3 OBJECTIVES .....	3
1.4 THESIS OUTLINE .....	4
1.5 CONTRIBUTIONS .....	4
1.5.1 <i>Journal Publications</i> .....	4
1.5.2 <i>Refereed Conference Proceedings</i> .....	4
<b>CHAPTER 2:LITERATURE REVIEW .....</b>	<b>5</b>
2.1 NiTi SHAPE MEMORY ALLOY .....	5
2.1.1 <i>Physical Metallurgy</i> .....	5
2.1.2 <i>Reversible Phase Transformation</i> .....	6
2.1.3 <i>The Shape Memory Effect</i> .....	8
2.1.4 <i>Pseudoelasticity</i> .....	10
2.1.5 <i>Effects of Composition and Aging</i> .....	13
2.1.6 <i>Ternary SMAs</i> .....	14
2.2 NiTi SURFACE OXIDE FORMATION .....	15
2.2.1 <i>Heat Treatment</i> .....	17
2.2.2 <i>Chemical Etching</i> .....	19
2.2.3 <i>Mechanical Polishing</i> .....	20
2.2.4 <i>Laser Surface Melting</i> .....	20
2.2.5 <i>Boiling Water</i> .....	21
2.2.6 <i>Hydrogen Peroxide</i> .....	21
2.2.7 <i>Autoclave</i> .....	21

2.2.8 Electropolishing .....	22
2.2.9 Ion Implantation.....	22
2.3 CORROSION ANALYSIS.....	23
2.3.1 Fundamentals of SECM Analysis .....	24
2.3.2 Fundamentals of Potentiodynamic Cyclic Polarization Analysis.....	26
2.4 LASER FUNDAMENTALS .....	29
2.4.1 Pulsed Nd:YAG Laser Processing.....	31
2.4.2 Processing Parameters.....	32
2.4.3 Shielding Gas .....	34
2.4.4 Laser Beam Modes .....	34
<b>CHAPTER 3: EXPERIMENTAL METHODS.....</b>	<b>36</b>
3.1 MATERIAL SELECTION .....	36
3.2 LASER PROCESSING EQUIPMENT AND PARAMETERS .....	36
3.3 POST-PROCESS SURFACE TREATMENT .....	38
3.4 ANALYTICAL METHODS .....	39
3.4.1 Surface Analysis .....	39
3.4.2 Scanning Electrochemical Microscopy .....	39
3.4.3 Raman Spectroscopy .....	41
3.4.4 Cyclic Potentiodynamic Polarization.....	41
<b>CHAPTER 4: EVOLUTION OF SURFACE STRUCTURE AFTER LASER MODIFICATION.....</b>	<b>44</b>
4.1 EFFECTS OF SINGLE SPOT LASER PULSING.....	44
4.1.1 Surface Morphology.....	44
4.1.2 SECM images in the feedback mode.....	45
4.1.3 Feedback mode approach curves .....	48
4.1.4 Crystallinity of Surface Oxide .....	50
4.1.5 Corrosion Resistance.....	51
4.2 EFFECTS OF AN ARRAY OF PULSED LASER SPOTS .....	53
4.2.1 Topography of Overlapping Spots.....	54
4.2.2 Crystallinity of Surface Oxides.....	54
4.2.3 Corrosion Resistance.....	55
4.3 CHAPTER SUMMARY .....	57
<b>CHAPTER 5: POST-PROCESS SURFACE MODIFICATIONS .....</b>	<b>58</b>
5.1 MECHANICAL POLISHING.....	58
5.1.1 Topography of Mechanically Polished Surface.....	58
5.1.2 Crystallinity of Oxide formed by Mechanical Polishing .....	59

5.1.3 Corrosion Resistance of Mechanically Polished Surface.....	60
5.2 CHEMICAL ETCHING .....	62
5.2.1 Topography of Chemically Etched Surface.....	62
5.2.2 Crystallinity of Oxide formed by Chemical Etching.....	63
5.2.3 Corrosion Resistance of Chemically Etched Surface.....	64
5.2 BOILING WATER.....	65
5.3.1 Topography of Surfaces after Boiling Water Treatment.....	66
5.3.2 Crystallinity of Oxide formed by Boiling Water.....	67
5.3.3 Corrosion Resistance of Boiling Water Treated Surfaces.....	67
5.3 CHAPTER SUMMARY .....	69
<b>CHAPTER 6: CONCLUSIONS.....</b>	<b>71</b>
6.1 OXIDE EVOLUTION .....	71
6.2 POST-PROCESS MODIFICATIONS.....	71
6.3 RECOMMENDATIONS FOR FUTURE WORK.....	72
6.3.1 Alternative Sample Preparation.....	72
6.3.2 Improved Corrosion Test Procedure.....	73
6.3.3 Additional Testing Required.....	74
6.3.4 Additional Materials .....	75
REFERENCES.....	76
APPENDIX I: ADDITIONAL SECM ANALYSIS .....	87
APPENDIX II: EXPERIMENTAL DATA FOR RAMAN TESTS.....	88
APPENDIX III: EXPERIMENTAL DATA FOR CYCLIC POLARIZATION TESTS .....	93
GLOSSARY OF TERMS .....	103

## List of Figures

<i>Figure 1.1: Schematic diagram showing similarities between laser welding and laser modification of NiTi SMAs....</i>	1
<i>Figure 1.2: Cyclic polarization of a) base material and b) weld zone material with and without post-process heat treatments in Hanks' solution at 37.5 °C [20].</i>	3
<i>Figure 2.1: Binary Ti-Ni phase diagram with inset showing the metastable Ni-rich TiNi IMCs. Figure is adapted from [27, 34].</i>	6
<i>Figure 2.2: a) The B2 austenite phase (shaded box) and b) the B19' martensite phase. Ti is represented by blue spheres and Ni by red spheres. Figure adapted from [39].</i>	7
<i>Figure 2.3: Schematic representation of the atomic movements associated with martensitic transformation by a) slip and b) twinning. Figure adapted from [24].</i>	8
<i>Figure 2.4: Crystallographic of the shape memory effect [45].</i>	9
<i>Figure 2.5: A Typical DSC curve of NiTi SMA [50].</i>	10
<i>Figure 2.6: a) Stress-strain curve of pseudoelastic NiTi exhibiting the following regions: 1) elastic response of austenite, 2) pseudoelastic plateau caused by stress-induced transformation and 3) elastic and plastic deformation of martensite. b) Stress-strain curve of NiTi when the load is released in region 2). [51].</i>	11
<i>Figure 2.7: Plateau stress versus temperature plot. Dashed lines represent the linear Clausius-Clapeyron relation between <math>\sigma_{SIM}</math> (empty circles) and <math>\sigma_r</math> (solid circles) and temperature, when <math>T &gt; A_f</math>. Detwinning of martensite occurs below <math>A_f</math> and plastic deformation of austenite occurs above <math>M_d</math> causing deviations from the Clausius-Clapeyron relationship [52].</i>	12
<i>Figure 2.8: Stress-temperature conditions for NiTi SMAs exhibiting shape memory effect and pseudoelasticity. Adapted from [55].</i>	12
<i>Figure 2.9: Relationship between mole-fraction of Ni and the <math>M_s</math> temperature in binary NiTi SMAs [57].</i>	13
<i>Figure 2.10: Time-temperature-transformation (TTT) diagram showing the relationship between heat treatment temperature, time, and <math>A_f</math> transformation temperatures. Figure adapted from [53].</i>	14
<i>Figure 2.11: a) Cross-section of 3-mm NiTi wire, b) close-up view of oxide layer: 1) surface, 2) oxide, 3) bulk interface. Figure adapted from [67].</i>	16
<i>Figure 2.12: a) The longitudinal view of 1) NiTi SMA wire this is 2-5) progressively strained and 6) unloaded with resulting permanent damage to the oxide. b) A cross-sectional view of 1) NiTi SMA wire before straining and 2) during straining with resulting damage to the oxide layer. Figure adapted from [73].</i>	17
<i>Figure 2.13: Ti-Ni-O phase diagram computed at 530 °C. Figure adapted from [78].</i>	19
<i>Figure 2.14: The Ti/Ni ratio and Ni surface concentration for the following surface treatments: 1) MP, 2) MP and CE, 3-5) steam AC for 30, 60 and 120 minutes, 6) BW for 30 minutes, 7-9) water AC for 30, 99 and 180 minutes, 10) HPS for 22 hours, 11) EP, 12) EP and steam AC, 13) EP and dry heat, 14) EP and ethylene oxide, 15) EP and peracetic acid decontamination, 16) EP and hydrogen peroxide plasma and 17) EP and peracetic acid plasma. Figure adapted from [65, 91].</i>	23

Figure 2.15: Schematic showing the reactions that takes place at the ME tip a) in the bulk solution, b) at an insulating surface and b) at a conductive surface. ....24

Figure 2.16: a) Analytic cathodic and anodic rates and b) simulated experimental polarization curves derived from a). Figure adapted from [96]. ....27

Figure 2.17: Schematic of active-passive polarization behavior. Figure adapted from [96]. ....28

Figure 2.18: Cyclic polarization curve showing  $E_{break}$  and  $E_{prot}$  (schematic). Figure adapted from [96]. ....29

Figure 2.19: Schematic showing how a laser cavity produces a laser beam [101]. ....30

Figure 2.20: Schematic of Nd:YAG laser setup [32]. ....32

Figure 2.21: Schematic of pulsed Nd:YAG output [32]. ....33

Figure 2.22: Schematic of the propagation and convergence of a laser beam [101]. ....33

Figure 2.23: Comparison of a) conduction and b) keyhole welding modes [97]. ....35

Figure 3.1: Laser processing setup. NiTi strip was clamped in the fixture with Ar gas shielding the top and bottom to prevent oxidation. [50]. ....37

Figure 3.2: a) Laser processing schedule and b) schematic of 50 % overlap of laser processed spots. Figure adapted from [50]. ....38

Figure 3.3: a) The components of custom-made working electrode (Teflon cap, rubber gasket and brass rod), b) assembled working electrode and c) ASTM standard configuration of similar set-up [104]. ....42

Figure 3.4: a) Corrosion cell used for cyclic potentiodynamic polarization test compared with b) standard set-up for cyclic polarization testing of implants [105]. ....43

Figure 4.1: a) Surface topography maps and b) SECM feedback images of 1LP, 3LP, 4LP and 5LP samples. Dashed lines correspond to line scans in Figure 4.3. (SECM analysis courtesy of Dr. Ushula Tefashe, McGill University) ....45

Figure 4.2: Optical images of a laser processed sample a) with post-process Ni deposits on surface and b) after cleaning thoroughly with acetone, ethanol, and de-ionized water .....46

Figure 4.3: Line scans of dimensionless ME current and ME-NiTi distance across the center of a) 1LP, b) 3LP, c) 4LP and d) 5LP corresponding to dashed lines in Figure 4.1. ....47

Figure 4.4: Normalized SECM feedback approach curves measured for 5LP. Symbol lines are experimental approach curves, solid lines are the theoretical curves for finite electron transfer kinetics, while dashed lines are the theoretical curves for a totally conducting sample (upper curve) and for a totally insulating sample (bottom curve), respectively. Inset shows the area from which the SECM feedback approach curves were recorded, starting in the CE region, transitioning through the HAZ into the LP surface region. (SECM analysis courtesy of Dr. Ushula Tefashe, McGill University). ....48

Figure 4.5: Raman spectra for a) 1LP and b) 5LP with a resolution of  $\leq 1 \text{ cm}^{-1}$ . Inset shows the area from which the Raman spectra were taken, indicating the different HAZ regions observed in the 5LP sample. ....50

Figure 4.6: Representative potentiodynamic cyclic polarization curves for a) CE, b) 1LP and c) 5LP with corresponding optical images of resulting corrosion. ....52

<i>Figure 4.7: Schematic showing relative surface areas exposed during cyclic polarization testing. Green is the CE surface area, blue is the LP re-melt surface area, and red is the HAZ surface area. Areas in schematic are approximations. ....</i>	<i>53</i>
<i>Figure 4.8: Surface topography maps of CE, 1LPO and 5LPO samples.....</i>	<i>54</i>
<i>Figure 4.9: Raman spectra for a) 1LPO and b) 5LPO with a resolution of <math>\leq 1 \text{ cm}^{-1}</math>. Inset shows the area from which the Raman spectra were taken, indicating the different HAZ regions observed in both samples.....</i>	<i>55</i>
<i>Figure 4.10: Representative potentiodynamic cyclic polarization curves for a) CE, b) 1LPO and c) 5LPO with corresponding optical images.....</i>	<i>56</i>
<i>Figure 5.1: Surface topography maps of CE, LP and LPMP samples.....</i>	<i>59</i>
<i>Figure 5.2: Representative Raman spectra for the CE surface, untreated HAZ region, and the LPMP surface.....</i>	<i>60</i>
<i>Figure 5.3: Representative potentiodynamic cyclic polarization curves for CE, 5LPO and LPMP.....</i>	<i>61</i>
<i>Figure 5.4: Surface topography maps of CE, LP and LPCE samples. ....</i>	<i>63</i>
<i>Figure 5.5: Optical image of a) 5LPO sample and b) LPCE sample showing differences in reflectivity after CET. .</i>	<i>63</i>
<i>Figure 5.6: Representative Raman spectra of the CE surface, the untreated HAZ region, and the LPCE surface....</i>	<i>64</i>
<i>Figure 5.7: Representative potentiodynamic cyclic polarization curves for CE, 5LPO and LPCE .....</i>	<i>65</i>
<i>Figure 5.8: Surface topography maps of LPMP, LPMPBW, LPCE and LPCEBW samples. ....</i>	<i>66</i>
<i>Figure 5.9: Representative Raman spectra for the LPMP surface, the LPMPBW surface, the LPCE surface and the LPCEBW surface. ....</i>	<i>67</i>
<i>Figure 5.10: Representative potentiodynamic cyclic polarization curves for CE, LPMP and LPMPBW .....</i>	<i>68</i>
<i>Figure 5.11: Representative potentiodynamic cyclic polarization curves for CE, LPCE and LPCEBW .....</i>	<i>69</i>
<i>Figure 6.1: Laser inside of glove box containing argon atmosphere and soot sucker. ....</i>	<i>73</i>
<i>Figure 6.2: Cross-sectional image of processed sample with partial penetration identifying the LP and BM/HAZ regions. Figure is adapted from [22].....</i>	<i>74</i>
<i>Figure A-I.1: SECM feedback image of a typical CE surface. ....</i>	<i>87</i>
<i>Figure A-I.2: Surface areas of reactive regions estimated from SECM feedback maps for a) 1LP, b) 3LP, c) 4LP and d) 5LP. Black regions are conductive areas, white regions are insulating areas.....</i>	<i>87</i>
<i>Figure A-II.1: Raman spectra for CE samples 1 to 4. ....</i>	<i>88</i>
<i>Figure A-II.2: Raman spectra for 1LP samples 1 to 4 in the a) CE region, b) HAZ region and c) LP region. ....</i>	<i>88</i>
<i>Figure A-II.3: Raman spectra for 5LP samples 1 to 4 in the a) CE region, b) HAZ1 region, c) HAZ2 region, d) HAZ3 region and e) LP region. ....</i>	<i>89</i>
<i>Figure A-II.4: Raman spectra for 1LPO samples 1 to 4 in the a) CE region, b) outer HAZ region, c) LP region and d) the inner HAZ region.....</i>	<i>90</i>
<i>Figure A-II.5: Raman spectra for 5LPO samples 1 to 4 in the a) CE region, b) outer HAZ region, c) LP region and d) the inner HAZ region.....</i>	<i>91</i>
<i>Figure A-II.6: Raman spectra for LPMP samples 1 to 4. ....</i>	<i>91</i>
<i>Figure A-II.7: Raman spectra for LPCE samples 1 to 4.....</i>	<i>92</i>
<i>Figure A-II.8: Raman spectra for LPMPBW samples 1 to 4. ....</i>	<i>92</i>

*Figure A-II.9: Raman spectra for LPCEBW samples 1 to 4.....92*

*Figure A-III.1: Cyclic polarization curves for CE samples 1 to 4.....93*

*Figure A-III.2: Cyclic polarization curves for 1LP samples 1 to 4.....94*

*Figure A-III.3: Cyclic polarization curves for 5LP samples 1 to 4.....95*

*Figure A-III.4: Cyclic polarization curves for 1LPO samples 1 to 4.....96*

*Figure A-III.5: Cyclic polarization curves for 5LPO samples 1 to 4.....97*

*Figure A-III.6: Cyclic polarization curves for LPMP samples 1 to 4.....98*

*Figure A-III.7: Cyclic polarization curves for LPMPBW samples 1 to 4.....99*

*Figure A-III.8: Cyclic polarization curves for LPCE samples 1 to 4.....100*

*Figure A-III.9: Cyclic polarization curves for LPCEBW samples 1 to 4.....101*

## List of Tables

<i>Table 1: Effective heterogeneous first-order rate constant <math>k_{eff}</math> values determined from approach curves. (Analysis by of Dr. Ushula Tefashe, McGill University)</i> .....	49
<i>Table A-III.1: Cyclic Polarization Values for CE</i> .....	93
<i>Table A-III.2: Cyclic Polarization Values for 1LP</i> .....	94
<i>Table A-III.3: Cyclic Polarization Values for 5LP</i> .....	95
<i>Table A-III.4: Cyclic Polarization Values for 1LPO</i> .....	96
<i>Table A-III.5: Cyclic Polarization Values for 5LPO</i> .....	97
<i>Table A-III.6: Cyclic Polarization Values for LPMP</i> .....	98
<i>Table A-III.7: Cyclic Polarization Values for LPMPBW</i> .....	99
<i>Table A-III.8: Cyclic Polarization Values for LPCE</i> .....	100
<i>Table A-III.9: Cyclic Polarization Values for LPCEBW</i> .....	101

# List of Equations

(Equation 1)..... 11  
(Equation 2)..... 25  
(Equation 3)..... 25  
(Equation 4)..... 25  
(Equation 5)..... 25  
(Equation 6)..... 25  
(Equation 7)..... 25  
(Equation 8)..... 26  
(Equation 9)..... 26  
(Equation 10)..... 26  
(Equation 11)..... 39  
(Equation 12)..... 40  
(Equation 13)..... 43  
(Equation 14)..... 43

# Chapter 1: Introduction

## 1.1 Background

The shape memory effect (SME) and pseudoelastic (PE) properties of NiTi shape memory alloys (SMAs) have made them valuable engineering materials [1, 2]. The industries interested in applying shape memory alloys (SMA) range from biomedical to automotive and aerospace to microelectronics. In particular, the excellent biocompatibility of NiTi based SMAs makes them highly desirable for many biomedical applications [3-8]. The demand from industry is a move towards increasingly more complex systems on a micro-scale. This requires various laser modification techniques designed to combine different SMA properties into one system [9-13].

## 1.2 Laser Processing of NiTi

In this study, laser processing will refer to any technique that uses energy from a laser source to heat a NiTi SMA for the purposes of joining or modifying the surface or bulk of the material. Each of these techniques results in a melted pool surrounded by a heat-affected zone (HAZ) surrounded by retained base material, as shown in Figure 1.1. This study is not concerned with the dissimilar joining of NiTi. Dissimilar joining results in a mixed weld pool, as well as retained base materials containing drastically different compositions. This is a significantly more complex corrosion system and should be investigated in future research (see Section 6.3.4 Additional Materials).

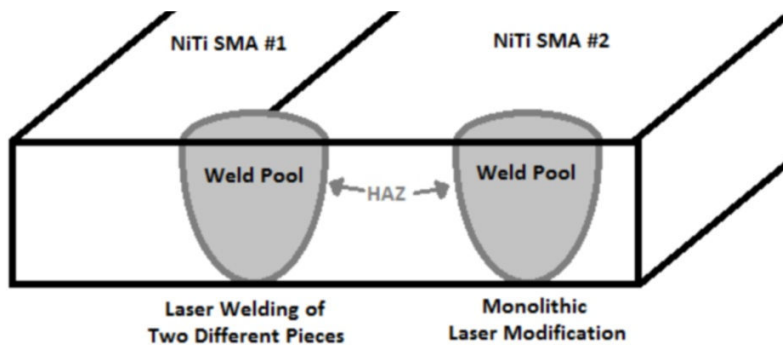


**Figure 1.1: Schematic diagram showing similarities between laser welding and laser modification of NiTi SMAs**

Previous studies that examined the effects of laser processing on the corrosion performance of NiTi SMAs differ in their findings. Some report that the corrosion performance of laser processed NiTi has been shown to be very good [14-16], while others report them to be slightly better than the base material [17- 19] or even somewhat worse than the base material [20-23].

Only a few of these studies actually attempt to characterize the surface after laser processing to determine how the oxide has changed in order to confirm the mechanisms behind these changes in corrosion performance [16, 20-22]. Cui et al. [16] characterized mechanically polished NiTi before and after laser processing using XPS and cyclic polarization. They found that laser processing increased the percent of Ti oxide present on the surface which increased corrosion resistance. Chan et al. [20] also characterized NiTi after laser processing by XPS and cyclic polarization, but they found little compositional differences between the processed region and the base material with only a slight decrease in the corrosion performance. However, another study by Chan et al. [21] observed grain recrystallization in the heat-affected zone (HAZ) after laser processing, which led to a decrease in its corrosion resistance. In a study by Pequegnat et al. [22] preferential corrosion was observed adjacent to overlapping pulsed laser spots. Therefore, it is necessary to determine the factors leading to these differing results in corrosion performance after laser processing.

Not only is it important to understand why the corrosion performance is altered after laser processing, it is also important to be able to restore the corrosion performance to pre-processed conditions. Chan et al. [20] investigated the use of post-process heat treatments to improve corrosion performance. They observed that the corrosion performance was enhanced slightly due to an increase in the thickness of the oxide layer, see Figure 1.2. However, this post-process heat treatment was only tested on the base material or weld zone separately, never in a combined system. Additional surface treatments for NiTi will be discussed in detail in Section 2.2 NiTi Surface Oxide Formation.

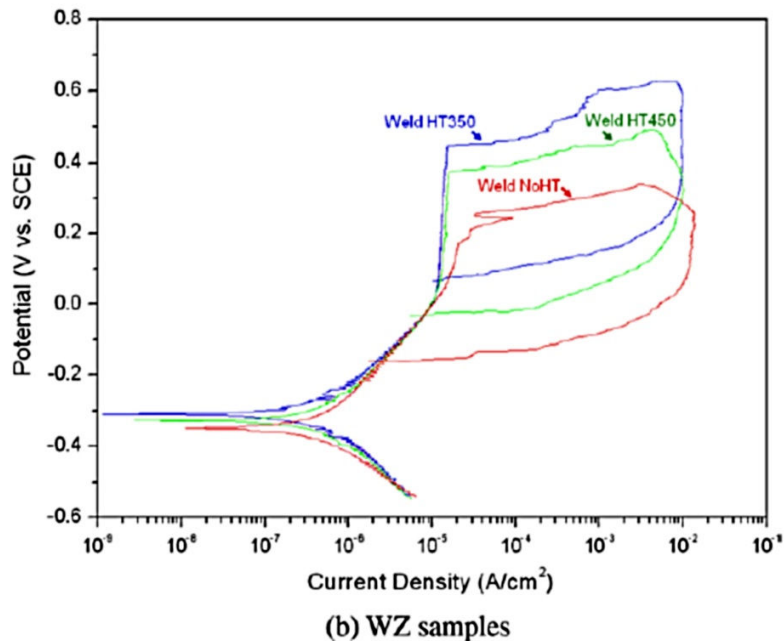
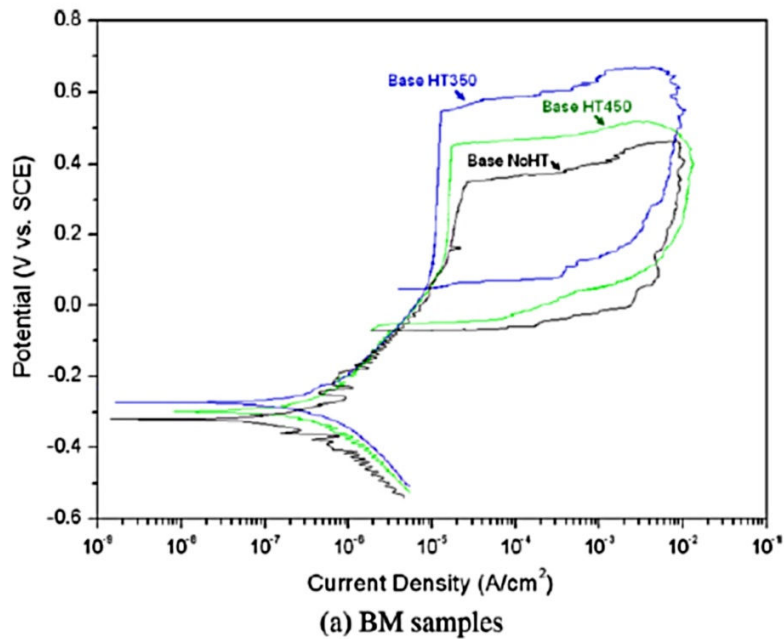


**Figure 1.2: Cyclic polarization of a) base material and b) weld zone material with and without post-process heat treatments in Hanks' solution at 37.5 °C [20].**

### 1.3 Objectives

The objective of this thesis is to methodically study the evolution of the surface constituents after laser modification and determine a means of modifying the surface structure post-laser processing. It is split into two main sub-objectives:

1. Identify the root cause for a decrease in corrosion resistance after laser modification.
2. Implement post-process procedures to restore corrosion performance to pre-processed capabilities.

## **1.4 Thesis Outline**

This dissertation is organized into six chapters. Chapter 2 reviews the material science of NiTi and the passive oxide that forms on the surface of NiTi alloys, as well as the common surface treatments currently employed to improve corrosion performance and laser fundamentals. Chapter 3 discusses experimental conditions and test set-ups and theory. Chapter 4 explores the evolution of the surface oxide after laser modification. Chapter 5 identifies post-process treatments that can restore the corrosion performance of NiTi after laser modification. Conclusions and recommendations for future work are presented in Chapter 6.

## **1.5 Contributions**

### **1.5.1 Journal Publications**

1. A. Pequegnat, A. Michael, J. Wang, K. Lian, Y. Zhou, M.I. Khan, Effects of laser processing on surface characteristics of NiTi shape memory alloys, Submitted to Corrosion Science Ms. Ref. No.: CORSCI-D-14-00269

### **1.5.2 Refereed Conference Proceedings**

2. B. Panton, A. Michael, A. Pequegnat, M. Daly, Y.N. Zhou, M.I. Khan, An innovative laser-processed NiTi self-biasing linear actuator, in: Proceedings of the ASME 2013 Conference on Smart Materials, Adaptive Structures and Intelligent Systems, Snowbird, Utah, USA, (2013)

# Chapter 2: Literature Review

## 2.1 NiTi Shape Memory Alloy

NiTi shape memory alloys (SMAs) are a subset of smart materials that are distinguished by their inherent capability of performing useful work harnessed from the thermo-mechanical reaction of the material to external stimuli. Several SMAs have been discovered, including but not limited to Cu-Zn-Al [24], Cu-Al-Ni [24], Au-Cd [24, 25] and In-Tl [26]. Some of the advantages of NiTi over other SMAs are its superior mechanical properties, which include better strength, ductility and recoverable strains [27, 28]. Also, NiTi exhibits higher electrical resistivity, stability of transformation temperatures, corrosion resistance and biocompatibility [24, 27, 29].

### 2.1.1 Physical Metallurgy

Figure 2.1 shows the Ti-Ni phase diagram. NiTi SMAs are considered an organized intermetallic compound (IMC) [30], with compositions close to 50 at.% Ni. NiTi SMAs are a stoichiometric IMC bounded by the  $Ti_2Ni$  and  $TiNi_3$  phases.  $Ti_2Ni$  IMC formation is undesirable due to its brittleness, which can lead to cracking in Ti-rich welds [31]. The constituent species are immiscible at room temperature; however, short heat treatment times at temperatures ranging from 300 °C to 600 °C can form Ni-rich metastable IMCs consisting of  $Ti_3Ni_4$  and  $Ti_2Ni_3$  [30, 32, 33]. The solubility of Ni increases significantly above 650 °C, permitting the production of Ni-rich SMAs through quenching [32]. NiTi is presently the only IMC known to possess SMA properties, but precipitation of the other Ni-rich IMCs into the NiTi matrix can modify the properties of the NiTi SMA [30].

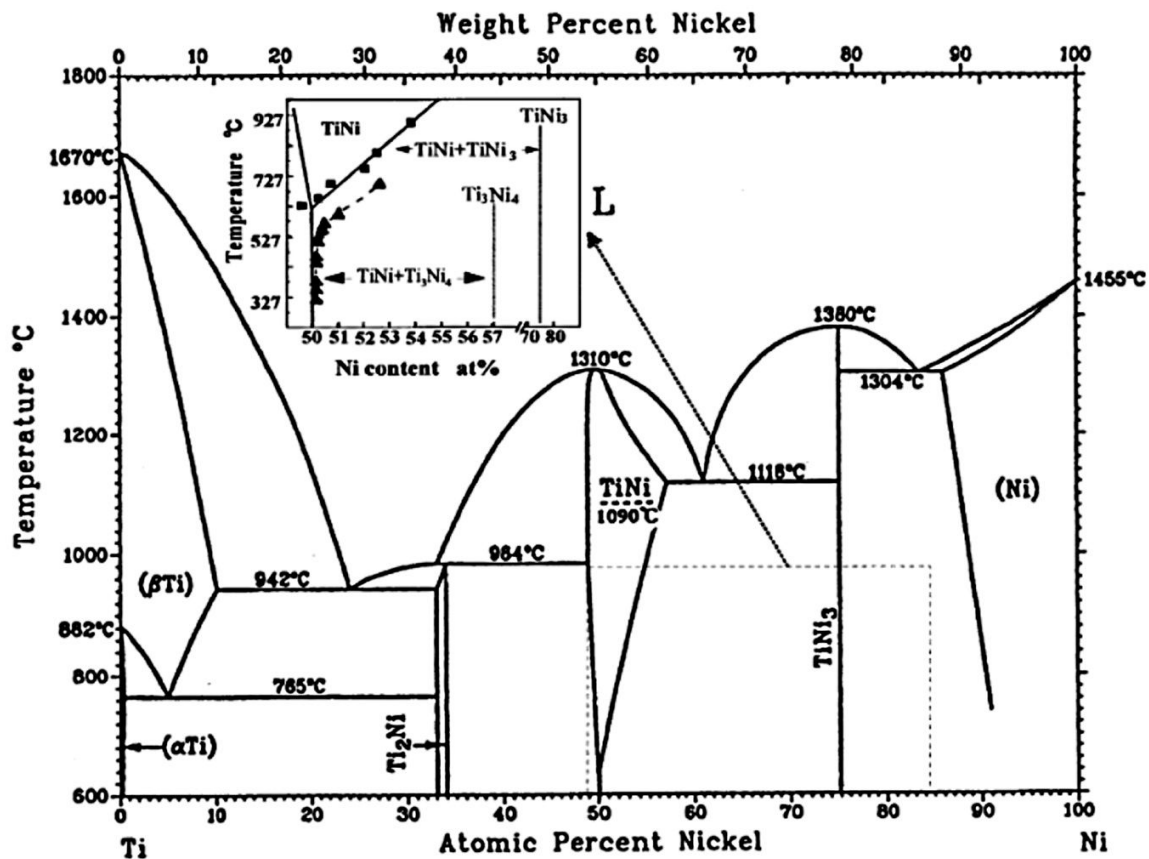
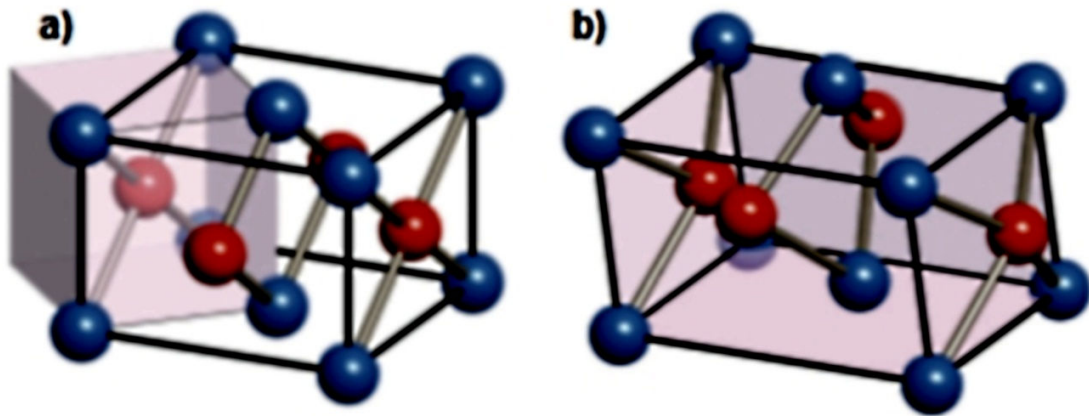


Figure 2.1: Binary Ti-Ni phase diagram with inset showing the metastable Ni-rich TiNi IMCs. Figure is adapted from [27, 34].

### 2.1.2 Reversible Phase Transformation

The exceptional shape memory properties of NiTi SMAs are due to a reversible solid-state phase transformation between martensite and austenite that occurs when the material is exposed to an external stimulus such as a change in temperature or applied stress. The martensitic transformation occurs between the parent B2 austenite phase and the B19' martensite phase [28, 35, 36]. The austenite phase has a simple cubic CsCl-type ordered structure with a lattice parameter of 0.3015 nm [37], shown in Figure 2.2a. Meanwhile, the martensite phase has a monoclinic structure with lattice parameters  $a = 0.2889$ ,  $b = 0.4120$  and  $c = 0.4622$  nm with a monoclinic angle  $\beta = 96.8^\circ$  [38], shown in Figure 2.2b. Since the transformation involves no diffusional atomic migration, it is very rapid [24].



**Figure 2.2: a) The B2 austenite phase (shaded box) and b) the B19' martensite phase. Ti is represented by blue spheres and Ni by red spheres. Figure adapted from [39].**

During thermally-induced martensitic transformation in steel alloys, atomic rearrangement is accommodated by irreversible dislocation motions. The crystallographic lattice undergoes an irreversible shearing deformation, which alters the volume and shape of the material on a macroscopic scale [40]. However, NiTi undergoes a reversible martensitic transformation. Twinning of the crystal lattice accommodates a change in shape, but no change in volume occurs [28, 35-38, 41, 42]. Twinned martensitic transformations of NiTi SMAs are considered reversible because the microstructures of the austenite and martensite phases can be cyclically restored with almost no buildup of lattice defects [40, 43]. In order for this transformation to be fully reversible, twinning must be the dominant accommodation process, as it is in NiTi SMAs [28]; whereas twinning can occur but slipping is dominant in steel alloys. The difference between slipping and twinning during a martensitic transformation is shown in Figure 2.3. During slip, the atomic planes slide past one another and form permanent dislocations in the crystal lattice. Conversely, twinning is the formation of a mirrored structure due to atomic displacement across a particular atomic plane [24]. Twinning occurs in NiTi SMAs because of a lack of symmetry and available slip-systems, which increases the driving force for generating twins after the martensitic phase transformation. Additionally, the twinned lattice can accommodate an externally applied stress by undergoing a recoverable detwinning process, in which the twinned lattices reorient themselves in response to the applied stress [24, 44]. This is possible because there are no bonds broken during the twinning process and thus the twins have low energy and are highly mobile.

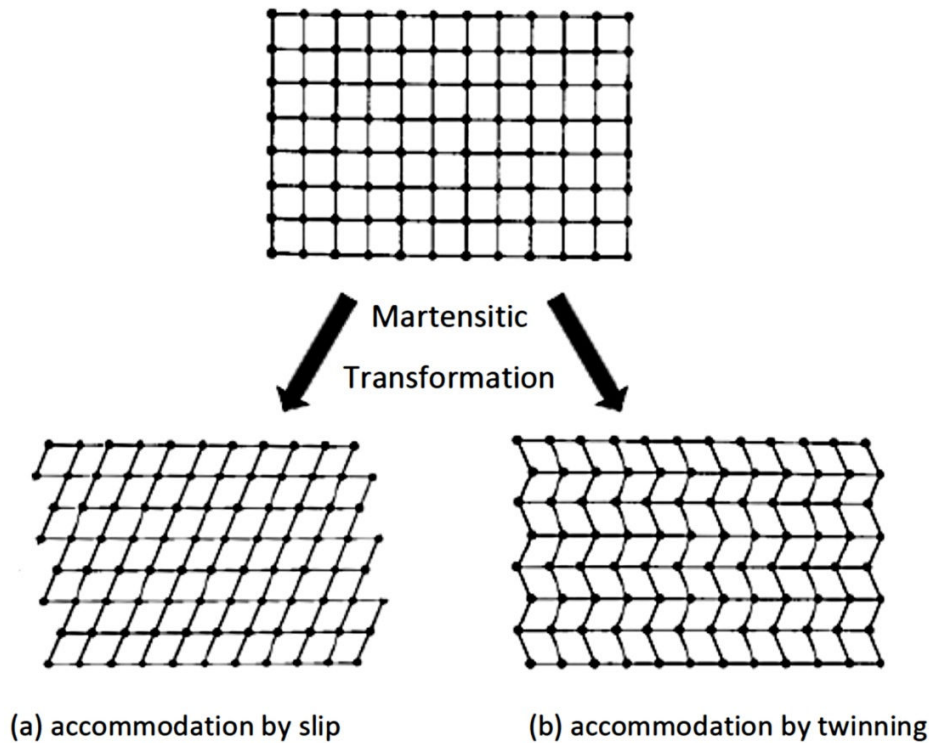


**Figure 2.3: Schematic representation of the atomic movements associated with martensitic transformation by a) slip and b) twinning. Figure adapted from [24].**

### 2.1.3 The Shape Memory Effect

When twinned martensite accommodates a large amount of strain and detwins a biased distribution of martensite variants, or in the extreme case, a single variant form [24]. Heating above the transformation temperature causes austenite to form. Austenite is a symmetrical, single variant structure and recovers the original shape [24]. This property of thermally induced phase transformation is known as the shape memory effect (SME), as illustrated in Figure 2.4. Shapes can be programmed into the NiTi SMA by way of a shape-setting technique where the material is fixed in a specific shape during a certain heat treatment procedure.

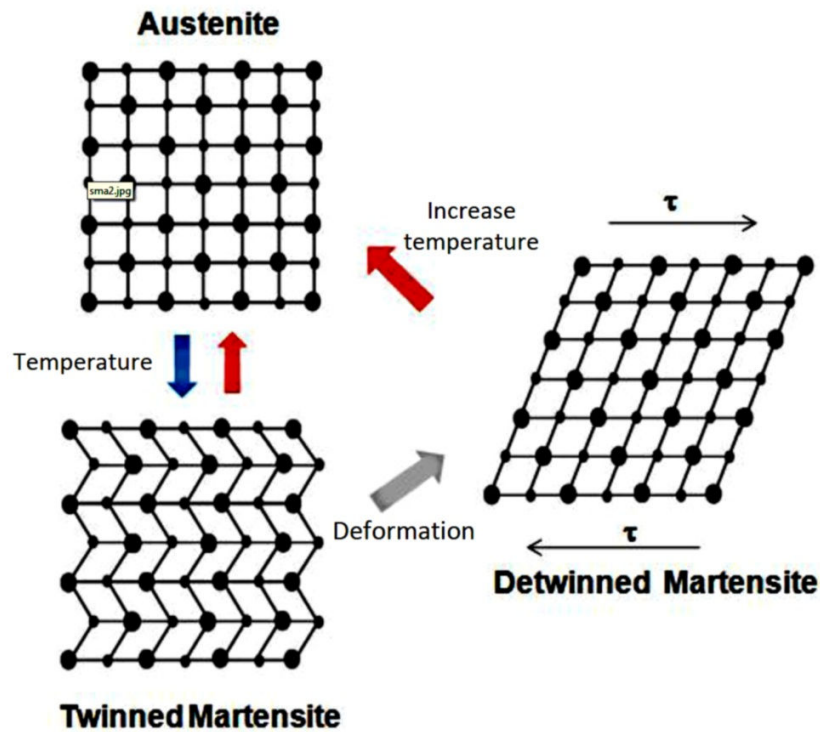


**Figure 2.4: Crystallographic of the shape memory effect [45].**

Cooling below the transformation temperature allows twinned martensite to be formed once again. This two-way phase transformation can occur at different temperatures between  $-150\text{ }^{\circ}\text{C}$  and  $200\text{ }^{\circ}\text{C}$ , determined by the composition of the SMA. The transformation is characterized by four temperatures: austenite start ( $A_s$ ), austenite finish ( $A_f$ ), martensite start ( $M_s$ ), and martensite finish ( $M_f$ ), which can be measured through DSC analysis [46]. These are the temperatures at which the martensite-to-austenite transformation and the reverse transformation begin and end. A hysteresis is observed between heating and cooling transformations, which is due to the frictional force encountered during lattice movement across interfaces and defects [24]. The magnitude of hysteresis is generally  $10\text{ }^{\circ}\text{C}$  to  $50\text{ }^{\circ}\text{C}$ , depending on the composition, processing history and stress state of the material [47-49]. A typical DSC curve of NiTi SMA is shown in Figure 2.5.

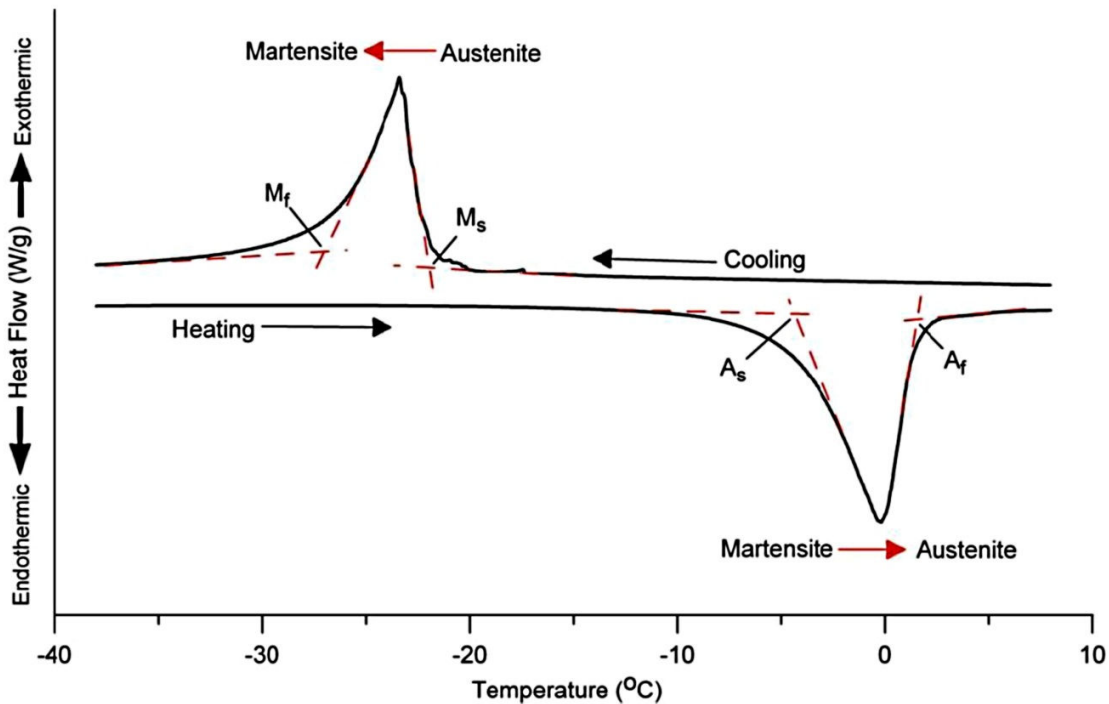
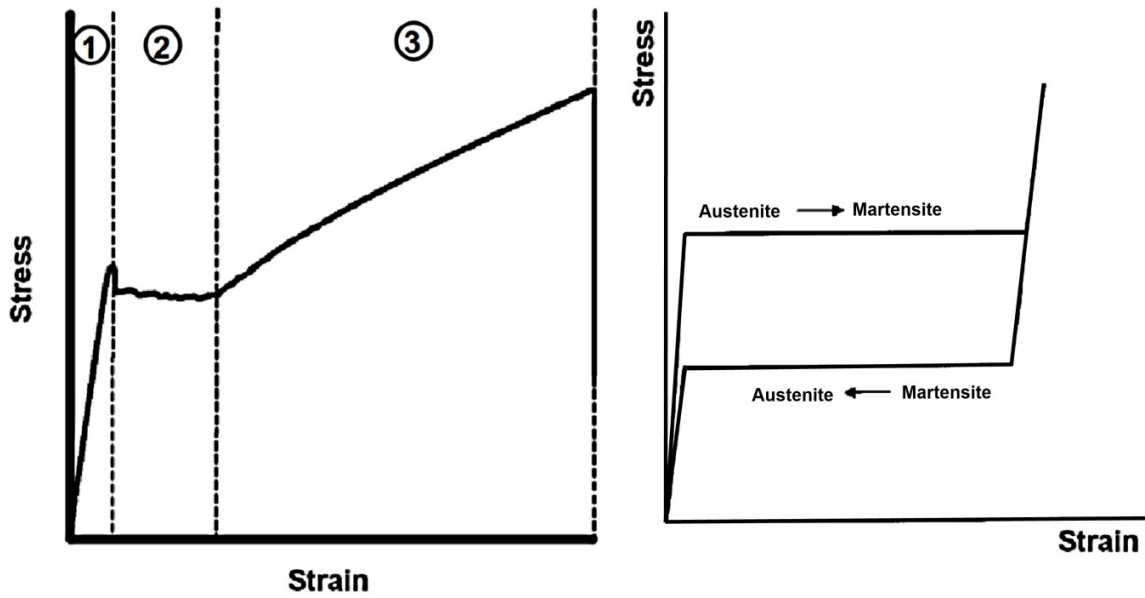


Figure 2.5: A Typical DSC curve of NiTi SMA [50].

### 2.1.4 Pseudoelasticity

When NiTi SMAs are in the austenite phase, it is possible for them to be converted to martensite by way of a stressing agent. When stress is the stabilizer, the martensite formed is known as stress-induced martensite (SIM). This transformation is called pseudoelasticity (PE), and the mechanical response is similar to detwinning. The principal action varies slightly and is divided into the three regions shown in Figure 2.6a. In region (1) the austenite is deformed elastically in accordance with Hooke's Law. At a critical stress ( $\sigma_{SIM}$ ), SIM is progressively formed at the expense of the parent phase until all of the parent phase is consumed. The result of this transformation is the plateau in region (2). Further straining results in the elastic and then plastic deformation of the detwinned martensite in region (3), which is again obeying Hooke's Law. If stress is removed in region (2), a reverse transformation takes place at a lower stress ( $\sigma_r$ ) due to a transformational hysteresis [46], shown in Figure 2.6b. This is similar to the hysteresis associated with thermally induced transformations.



**Figure 2.6: a) Stress-strain curve of pseudoelastic NiTi exhibiting the following regions: 1) elastic response of austenite, 2) pseudoelastic plateau caused by stress-induced transformation and 3) elastic and plastic deformation of martensite. b) Stress-strain curve of NiTi when the load is released in region 2). [51]**

The stable phase at the working temperature determines which functional property is active. Below  $M_f$ , the principal functional property is SME. PE is only observed above  $A_f$  but below the martensite deformation temperature ( $M_d$ ), which is the highest temperature that martensite can form from austenite as a result of an applied stress. As the temperature of NiTi increases above  $A_f$ , the thermodynamic stability of the austenite phase also increases, which causes a parallel increase in the stress needed to form SIM. This stress increase has been observed to vary linearly with temperature, as shown in Figure 2.7 and follows a Clausius-Clapeyron relation [52-54]. The Clausius-Clapeyron relationship is provided in equation (1) below [53]:

$$\frac{d\sigma}{dT} = \frac{-\Delta H}{T\varepsilon_0} \quad (\text{Equation 1})$$

where  $d\sigma$  is the change in  $\sigma_{SIM}$ ,  $dT$  is the change in test temperature,  $\Delta H$  is the latent heat of transformation and  $\varepsilon_0$  is the transformational strain. The left side of equation (1) is the stress rate, which varies from 3 to 20 MPa/°C, depending on the processing history of the material [53]. At temperatures above  $M_d$ , the specimen begins to fail before the onset of PE. Figure 2.8 illustrates the stress-temperature conditions for SME and PE in NiTi. At temperatures where

the transformation is partially completed, that is between  $M_s$  and  $M_f$  or  $A_s$  and  $A_f$ , the two phases will co-exist.

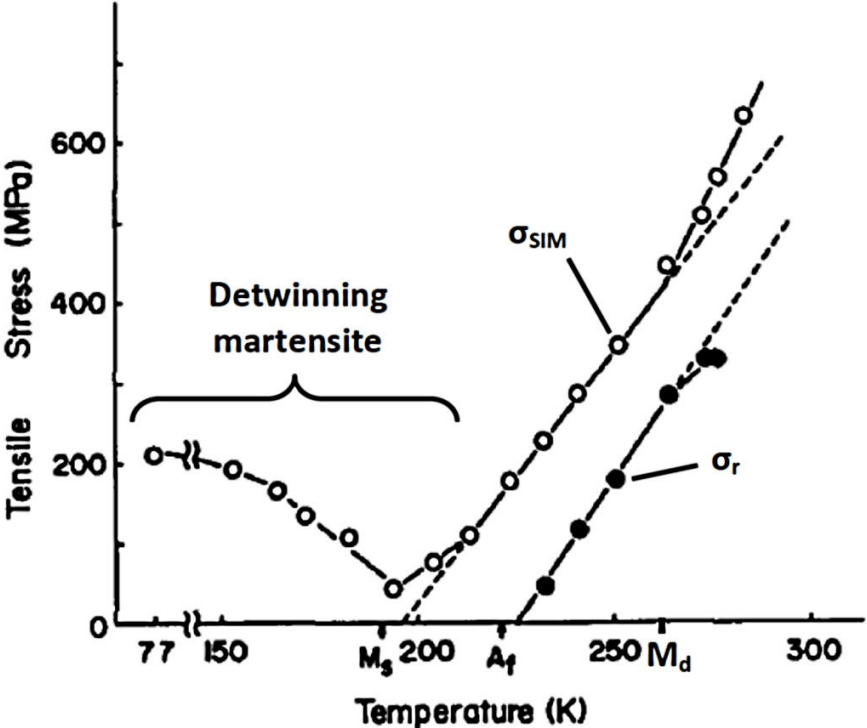


Figure 2.7: Plateau stress versus temperature plot. Dashed lines represent the linear Clausius-Clapeyron relation between  $\sigma_{SIM}$  (empty circles) and  $\sigma_r$  (solid circles) and temperature, when  $T > A_f$ . Detwinning of martensite occurs below  $A_f$  and plastic deformation of austenite occurs above  $M_d$  causing deviations from the Clausius-Clapeyron relationship [52].

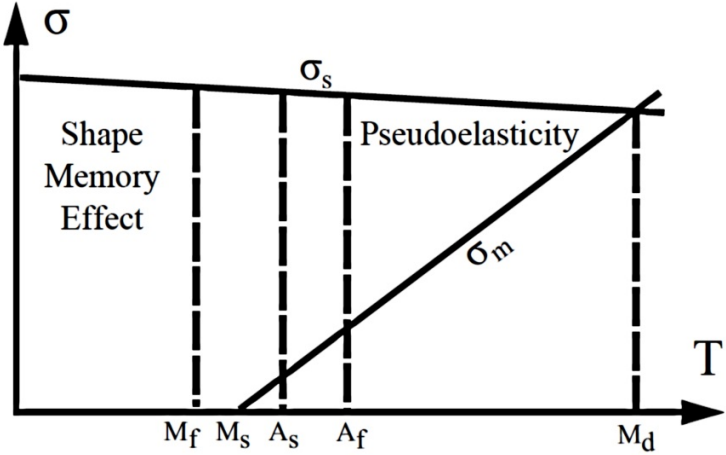
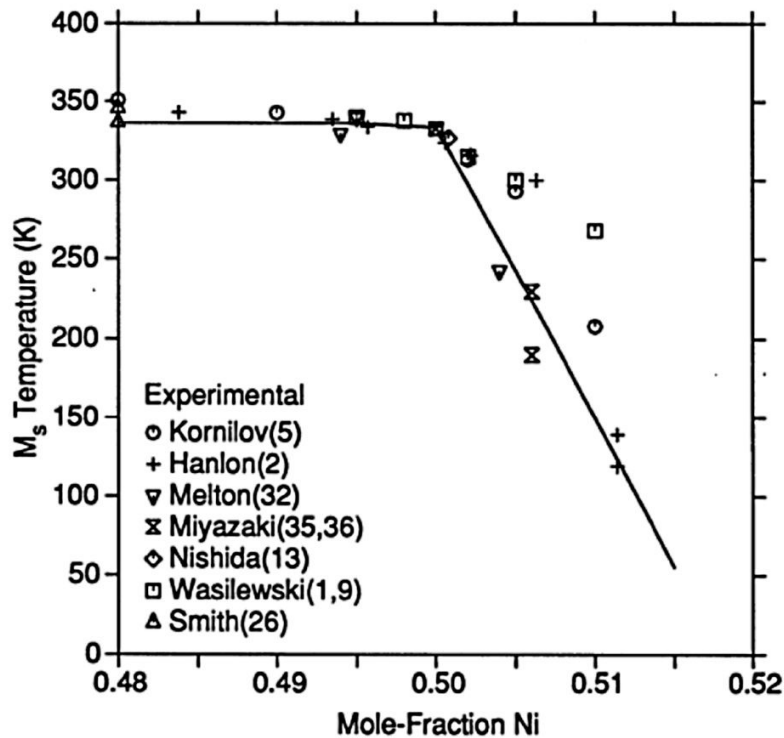


Figure 2.8: Stress-temperature conditions for NiTi SMAs exhibiting shape memory effect and pseudoelasticity. Adapted from [55].

### 2.1.5 Effects of Composition and Aging

The functional properties of NiTi SMA are very sensitive to alloy composition. The transformation temperatures are exceptionally sensitive to the mole fraction of Ni for concentrations above 50 at.%. However, for Ni concentrations below 50 at.%, the transformation temperature remains almost constant at approximately 65 °C due to the insolubility of Ti below 50 at.% (Figure 2.1). This relationship between composition and transformation temperature is shown in Figure 2.9. In addition to altering the transformation temperature, changes in composition indirectly control the amount of stress required to form SIM, because a lower  $A_f$  is associated with a more stable austenite phase [56]. Precise control over the final composition of the NiTi is critical to obtain the desired mechanical properties.



**Figure 2.9: Relationship between mole-fraction of Ni and the  $M_s$  temperature in binary NiTi SMAs [57].**

A time-temperature-transformation diagram developed by Pelton et al. [53] is shown in Figure 2.10 illustrating the relationship between Ni depletion and transformation temperature. As mentioned in Section 2.1.1 Physical Metallurgy, the formation of Ni-rich precipitates through post-process heat treatment is used to modify the functional properties of the NiTi SMA. These

precipitates deplete the NiTi matrix of Ni, causing significant increases in transformation temperatures. Increasing the transformation temperature by this method leads to a decrease in the  $\sigma_{SIM}$  due to a reduction in the stability of austenite [58].

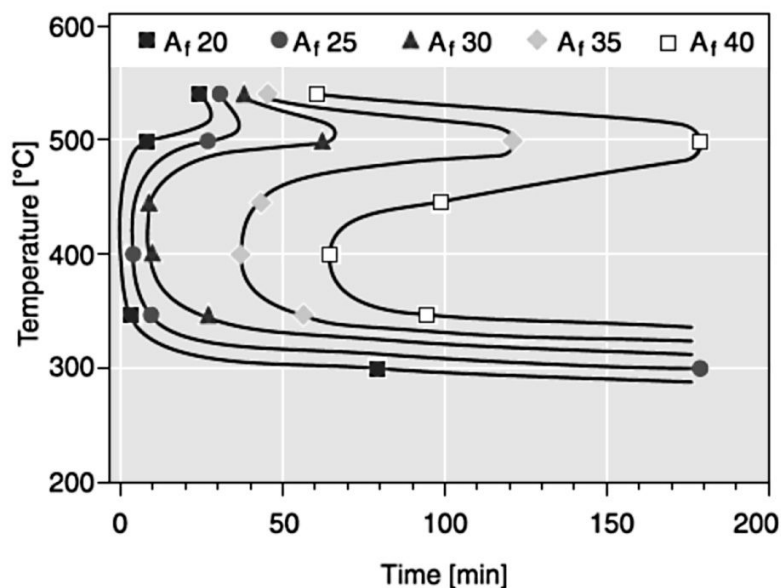


**Figure 2.10: Time-temperature-transformation (TTT) diagram showing the relationship between heat treatment temperature, time, and  $A_f$  transformation temperatures. Figure adapted from [53].**

### 2.1.6 Ternary SMAs

The addition of ternary species has been shown to beneficially modify the functional properties of the NiTi SMAs [59-61]. Chromium, cobalt, manganese and iron are austenite stabilizers, which significantly lower the  $M_s$  temperature. However, hafnium, gold, zirconium and palladium are martensite stabilizers, which raises the  $A_s$  temperature significantly. The addition of copper to a NiTi SMA has been shown to reduce the transformation hysteresis [48, 58]. While these ternary systems offer increased mechanical benefits, they can complicate the stability of the surface oxide, especially after laser modification processes. Ternary SMAs will not be investigated in this study, but should be analyzed in future research (see Section 6.3.4 Additional Materials).

## 2.2 NiTi Surface Oxide Formation

The corrosion resistance of NiTi SMAs is attributed to the passive oxide layer that forms on its surface. Due to the gain in free energy of formation ( $\Delta G_f$ ), formation of the Ti oxide supersedes that of the Ni oxide on the surface of NiTi SMAs. For instance, the  $\Delta G_f$  for  $\text{TiO}_2$  and NiO at room temperature is -940 kJ/mol and -211.7 kJ/mol respectively [62]. The  $\text{TiO}_2$  oxide found on NiTi SMAs is an n-type semiconductor with the same composition and defect density as the oxide found on CP Ti [63]. Titanium diffuses to the surface and reacts with oxygen; when the oxide gets thick enough, a Ni rich region will form between the oxide and the bulk material [64], as shown in Figure 2.11b (3).

This passive oxide layer also prevents the release of Ni ions from the bulk material, which is a potential allergen. Typically, Ni ion release from a NiTi SMA will be relatively high at first, but will drop off significantly after a few days [29, 65]. While formation of Ti oxides is preferred, the oxide layer is not inherently homogeneous. Depending on the processing history of the material, the surface species can contain different mixtures of Ti-based surface oxides, Ni-based oxides/hydroxides, and elemental Ni [29, 65], as can be seen in Figure 2.11b (1) and (2). Since these Ni ions are released early on, the oxide layer becomes depleted of Ni ions. Subsequent diffusion of Ni ions from the bulk material occurs through the Ti-rich oxide layer, which is a very slow process under typical biological conditions.

The breakdown potential and current density of NiTi SMAs measured by cyclic polarization tests is usually between those of Ti-6Al-4V and 316 SS, other typical biomaterials [66]. However, some variation in performance is observed, depending on how the surface oxide forms. Several critical factors affect the corrosion performance and the biocompatibility of the NiTi SMA surface oxide. The first factor is the homogeneity of the oxide. The more homogeneous the oxide is, the more stable it is [65]. The second factor is the crystallinity of the oxide layer. An amorphous oxide layer is very stable and prevents the diffusion of ions in both directions. A crystalline oxide allows for diffusion along grain boundaries and is therefore much less stable. Another factor is the surface roughness, which should always be taken into consideration when dealing with corrosion performance. Smoother surfaces have few initiation sites for corrosion to take place.

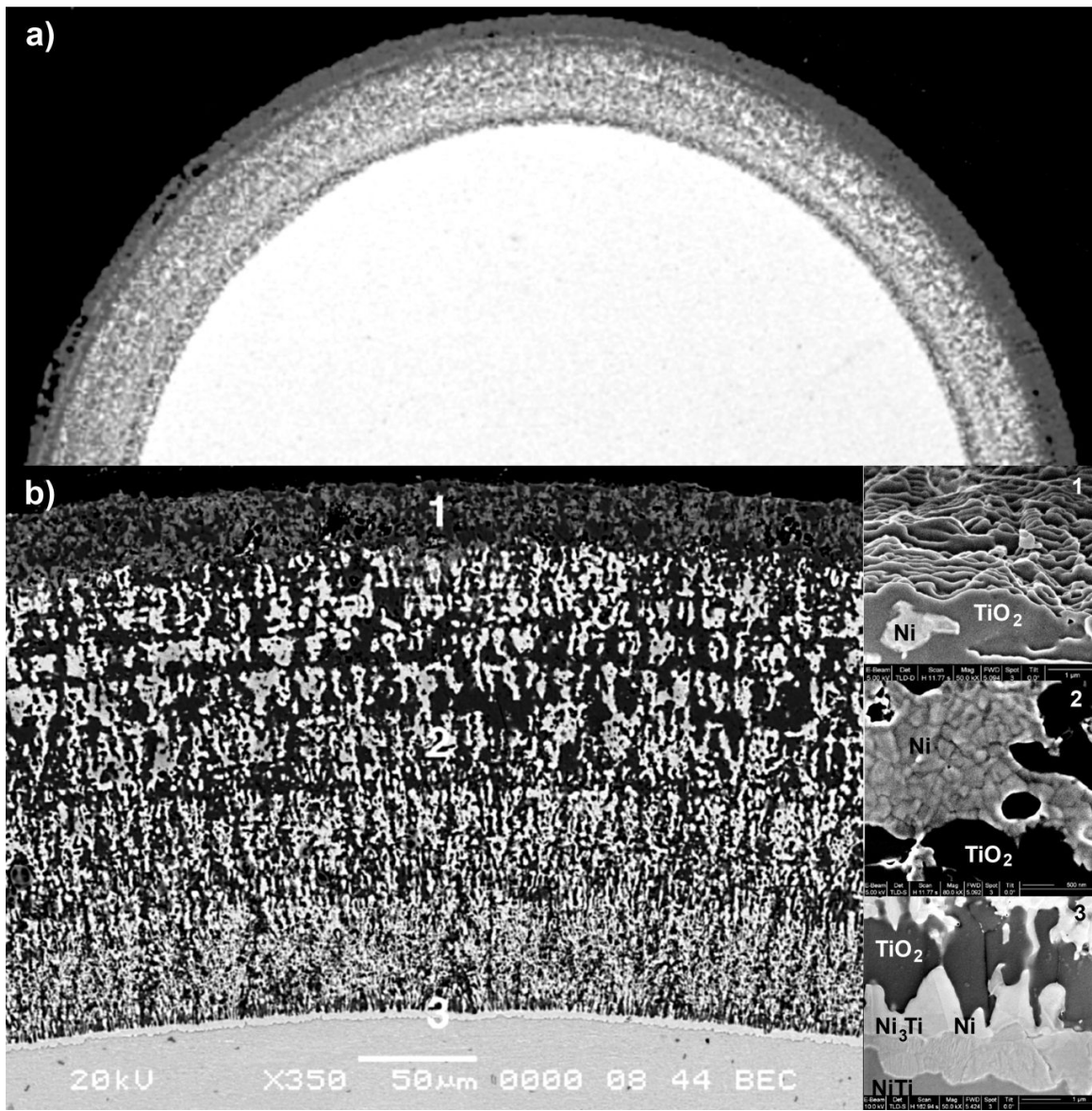


**Figure 2.11: a) Cross-section of 3-mm NiTi wire, b) close-up view of oxide layer: 1) surface, 2) oxide, 3) bulk interface. Figure adapted from [67].**

Oxide thickness is also important for various reasons. Typically, the thicker the passive oxide layer is, the better the corrosion performance, although this is not necessarily true for NiTi SMAs. While it is true that an oxide layer that is too thin will result in poor corrosion resistance, it is also true that too thick an oxide layer leads to poor corrosion performance of NiTi SMAs. When the Ti oxide layer is too thick, it becomes crystalline and brittle. Since it is well known that  $\text{TiO}_2$  is unstable under loading [68], this is very detrimental for NiTi SMAs because they are always employed in dynamic systems to take advantage of the SME and/or

PE capabilities. The schematic diagram in Figure 2.12 shows how the oxide layer of NiTi SMAs can be damaged by straining the material. This problem is further compounded if there is a Ni rich region between the oxide and the bulk material (see Figure 2.11). When the oxide is damaged, repassivation can be slowed because the Ti ions must diffuse through the Ni rich region before reaching the surface [63]. Thus, it is important to have a thin, homogenous, and amorphous oxide, approximately 5 to 20 nm thick, which has been shown to be capable of deforming up to 6% without damage [69, 70]. Different surface treatments drastically affect the biocompatibility and corrosion properties of the surface oxide [29, 65, 71, 72].

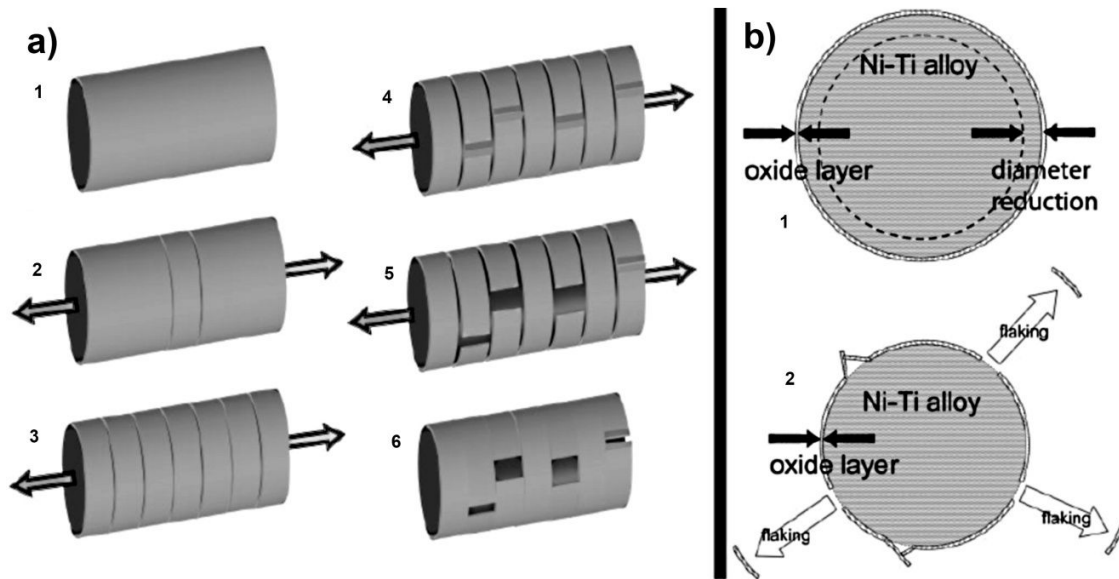


**Figure 2.12: a) The longitudinal view of 1) NiTi SMA wire this is 2-5) progressively strained and 6) unloaded with resulting permanent damage to the oxide. b) A cross-sectional view of 1) NiTi SMA wire before straining and 2) during straining with resulting damage to the oxide layer. Figure adapted from [73].**

### 2.2.1 Heat Treatment

The most basic method of forming a surface oxide is through heat treatment (HT). Heat treatment is typically done in air or oxygen environments at temperatures ranging from 300 °C to 600 °C [65, 69, 74-77]. This process typically builds a thick heterogeneous oxide that has a significant amount of elemental Ni and nickel oxides [65], and contains a mixture of various crystal structures [29]. Depending on the thickness of the oxide, reasonable corrosion resistance is achievable; however, it can be very unstable under loading conditions [69]. Heat treatment is sometimes considered a poor method of forming a passive oxide layer on NiTi

SMA as they contain many defects and are more susceptible to Ni ion release [75, 76]. However, they are necessary since heat treatment is required for shape setting (see Section 2.1.3 The Shape Memory Effect) and forming Ni-rich precipitates (see Section 2.1.5 Effects of Composition and Aging).

The corrosion performance of a HT surface is ultimately determined by the surface that is present before HT; thus, preceding HT with another surface treatment can improve or exacerbate the corrosion resistance of the final surface formed afterwards [29, 69, 74]. The exact temperature used can also have some effect on the oxide that is formed. Armitage et al. [77] found that the oxide grows inward during heat treatments up to 400 °C, which results in a composition of Ni and Ti in the oxide layer similar to that of the bulk material. However, they also found that temperatures from 500 °C to 600 °C encourage outward oxide growth, resulting in less Ni in the oxide layer. Another factor in oxide formation during heat treatment is the amount of oxygen available for reaction. The Ti-Ni-O phase diagram at 530 °C is shown in Figure 2.13. At high oxygen partial pressures, TiO<sub>2</sub> and NiO mixtures can exist over a wide range of oxygen levels. Lower partial pressures result in only Ti oxides forming, ranging from TiO<sub>2</sub> to Ti<sub>2</sub>O<sub>3</sub> to TiO, as the partial pressure of oxygen is reduced. Lowering the partial pressure also results in Ni-rich and Ti-rich precipitates forming, such as in the bulk where little or no oxygen is available for reaction (see 2.1.1 Physical Metallurgy).

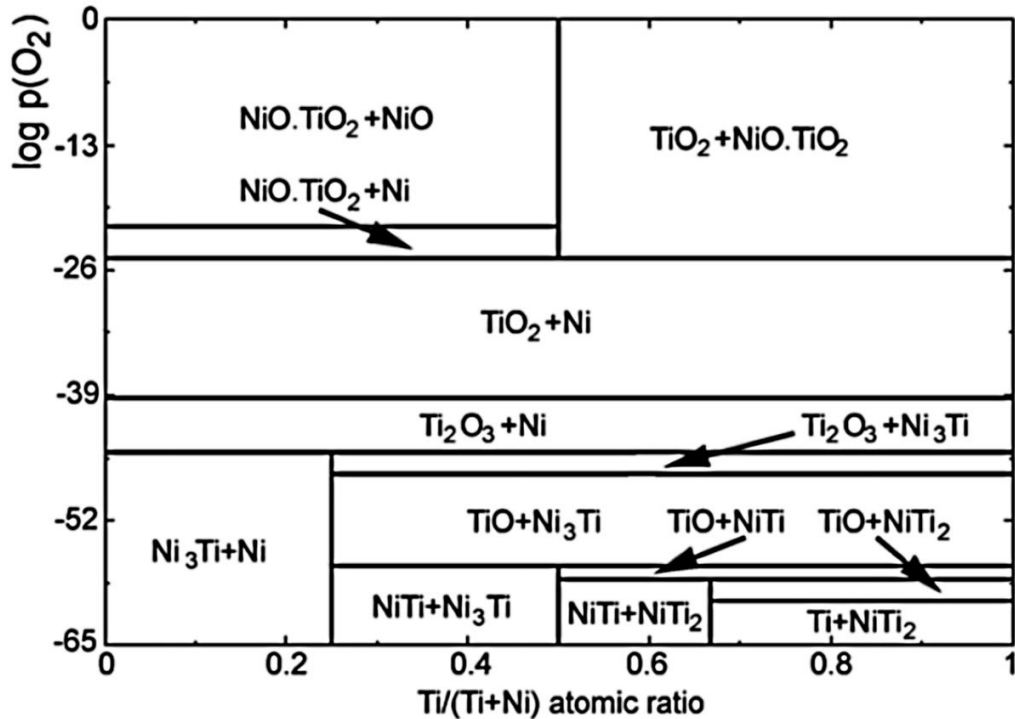


Figure 2.13: Ti-Ni-O phase diagram computed at 530 °C. Figure adapted from [78].

### 2.2.2 Chemical Etching

While it is possible to perform specialized heat treatments, typical manufacturing procedures do not go to such trouble. Most commercially available NiTi SMAs are covered in a thick, brittle oxide that is undesirable. The most common practice is to remove the thick oxide by means of a chemical etching treatment (CET). The chemical etchant consists of hydrofluoric acid (HF), nitric acid ( $\text{HNO}_3$ ) and de-ionized water. The most commonly used mixture is  $1\text{HF} + 4\text{HNO}_3 + 5\text{H}_2\text{O}$  [69, 74, 79-81]; however, other concentrations include HF: $\text{HNO}_3$ : $\text{H}_2\text{O}$  at 1:2:3 vol.% [82], as well as 7.5 vol.% HF, 20 vol.%  $\text{HNO}_3$  and the balance being  $\text{H}_2\text{O}$  [22]. Etching times can vary from 1 – 2 minutes with ultrasonic mixing [22, 81] to 4 – 10 minutes with no mixing [74, 79], all the way up to 30 minutes [80, 82]. However, extreme etching times should be avoided, since this can lead to hydrogen embrittlement [83].

The chemical etchant leaches nickel from the surface, which is evident from the green color that diffuses into the etching solution [74]. Since the HT oxide contains significant amounts of Ni, this effectively removes the outer most oxide layer from the surface. The chemical etchant also preferentially oxidizes Ti to yield a new oxide that is homogeneous and amorphous or

nanocrystalline [29, 74]. The resulting oxide thickness ranges from 2 to 12 nm [22, 69, 79, 80, 82]. The corrosion performance for CET surfaces is very good, although it is not as good as pure Ti.

### **2.2.3 Mechanical Polishing**

An alternative method to CET for removing the HT oxide is a mechanical polish (MP). The process of mechanical polishing physically removes the surface oxide and creates a much smoother surface. Typically, the polishing is done to a 1  $\mu\text{m}$  finish [29, 69, 77, 84], However, a rougher 1200-grit grinding paper has been used for the final polish [15, 63], as well as finer finishes of 0.3  $\mu\text{m}$  [80] and 0.03  $\mu\text{m}$  [22]. The new oxide formed during polishing is amorphous or nanocrystalline [22], but it is more heterogeneous than CET surfaces because it retains all of the phases present in the bulk material [29]. Also, oxidation at room temperature is not complete [65] and equilibrium is expected to be reached at a depth of approximately 3 nm [85]. This has been supported by many studies that have found oxide thickness ranging from 2.4 to 6 nm [22, 63, 77, 80, 84]. Since polishing finishes vary, so do the resulting corrosion resistance and biocompatibility, although good MP surfaces have a breakdown potential comparable to that of CET surfaces.

### **2.2.4 Laser Surface Melting**

Laser surface melting (LSM) (see Section 1.2 Laser Processing of NiTi) focuses on altering only the surface conditions of NiTi SMA. LSM smooths the surface by remelting and preferentially vaporizes Ni. LSM can be conducted in air or a shielding gas (see Section 2.4.3 Shielding Gas). When LSM is performed in air, this leads to a significant increase in  $\text{TiO}_2$ , which improves corrosion performance [15]. When performed with a shielding gas, the enhancement of the corrosion performance is due to the increase in the Ti/Ni ratio [15]. The resulting oxide layer is usually amorphous and likely non-uniform with areas of Ni enrichment [65]. However, the amount of Ni ions released decreases after LSM [16, 70]. The thickness of the oxide layer varies depending on the processing parameters and the initial surface conditions. Before LSM can be performed, the thick oxide created during manufacturing must be removed by means of either CET or MP; this is also true of all of the subsequent surface treatments, but this statement will not be made again.

### **2.2.5 Boiling Water**

One of the most promising methods for improving the corrosion performance of the NiTi SMA surface is the boiling water (BW) technique. The NiTi SMA is placed in boiling distilled water at 132 °C for 30 minutes [81, 86]. This promotes the diffusion of Ni to the surface. It has been shown that the innermost surface layers at a depth of 5-10 nm are depleted of Ni (< 5 at. %) after boiling in water [65]. The water provides a medium for removal of Ni from the surface, as shown by Shabalovskaya and Anderegg [79] through ICP AES analysis of the water after boiling. The boiling water also enables diffusion of oxygen into the surface, filling the vacancies left by the removal of Ni and promoting better stoichiometry [74]. The resulting oxide is either amorphous or nanocrystalline [74]. The depletion of Ni and insertion of oxygen in its place creates a significantly more homogeneous and stable oxide layer with significantly reduced Ni ion release [29, 70, 87] and corrosion performance can be similar to that of pure Ti [88]. Boiling the NiTi SMA for too long a period of time (typically 60 minutes or more) will cause the Ni in the bulk material to diffuse towards the surface [65], which is detrimental towards Ni ion release [87], since the Ni ions are more easily released from the surface than from the bulk. The thickness of the BW surface oxide is approximately 10-26 nm [65, 70].

### **2.2.6 Hydrogen Peroxide**

The use of 30% hydrogen peroxide ( $H_2O_2$ ) is done either by soaking for 22 hours (HPS) or by boiling for 2 hours (BHP). When the NiTi SMA goes through HPS, a Ni-rich oxide is formed, which contains some form of nickel oxide and/or nickel hydroxides [79, 88]. This Ni-rich surface allows an increased release of Ni ions, similar to pure Ni [88]. When the NiTi SMA goes through BHP, the surface is depleted of Ni and a thick titania scale rich in Ti-OH forms [89]. The surface oxide is homogeneous and shorter boiling times can be employed to reduce the oxide thickness from 100 nm to 10 nm to minimize cracking [90].

### **2.2.7 Autoclave**

Autoclaving (AC) can be done with either water or steam. Autoclaving is based on the same principal as BW. However, the use of a steam autoclave is significantly less efficient, since very little surface contact exists for the removal of Ni and humidity favors hydroxide formation

[65]. The use of water AC is capable of producing an extremely robust surface that is corrosion resistant, biocompatible and sterilized at the same time.

### **2.2.8 Electropolishing**

The method of electropolishing (EP) applies a differential potential between the sample being polished (anode) and another electrode, typically platinum (cathode). The surface is smoothed as metal is dissolved. Exact techniques for NiTi SMAs differ greatly and are often proprietary. For this reason, the corrosion performance of EP NiTi SMAs varies depending on who is the experimenter, NiTi SMA composition and electropolishing method. Michiardi et al. [84] reported higher Ti/Ni ratios and thicker oxides. However, Shabalovskaya et al. [29] found more heterogeneity and a thinner oxide (only a few nm). Typically the oxide is amorphous or nanocrystalline [69]. EP has the potential to produce a very good surface finish, but great care must be taken to make sure the procedure is done properly. Figure 2.14 presents the variation in Ti/Ni ratio and total % Ni on the surface for the various surface treatment methods discussed.

### **2.2.9 Ion Implantation**

A much less commonly used surface treatment is ion implantation. This is a line-of-sight process where ions are extracted from plasma, accelerated and blasted at a surface [29]. The oxide formed by this method has been shown to be amorphous [92], but is not of an ideal composition. While electron-beam radiation and ion implantation deplete Ni at the surface [29], it has been shown that Ni oxides can form in the oxide layer and  $Ti_4Ni_2O_x$  precipitates can form in the bulk [92]. These precipitates in the bulk can alter the functional properties of the NiTi SMA (see Section 2.1.5 Effects of Composition and Aging). Additionally, the oxide thickness can grow ten-fold that of the original surface oxide [92]. This provides improved corrosion resistance in static conditions, but leads to surface cracking with loads in the elastic region (<1%) [29].

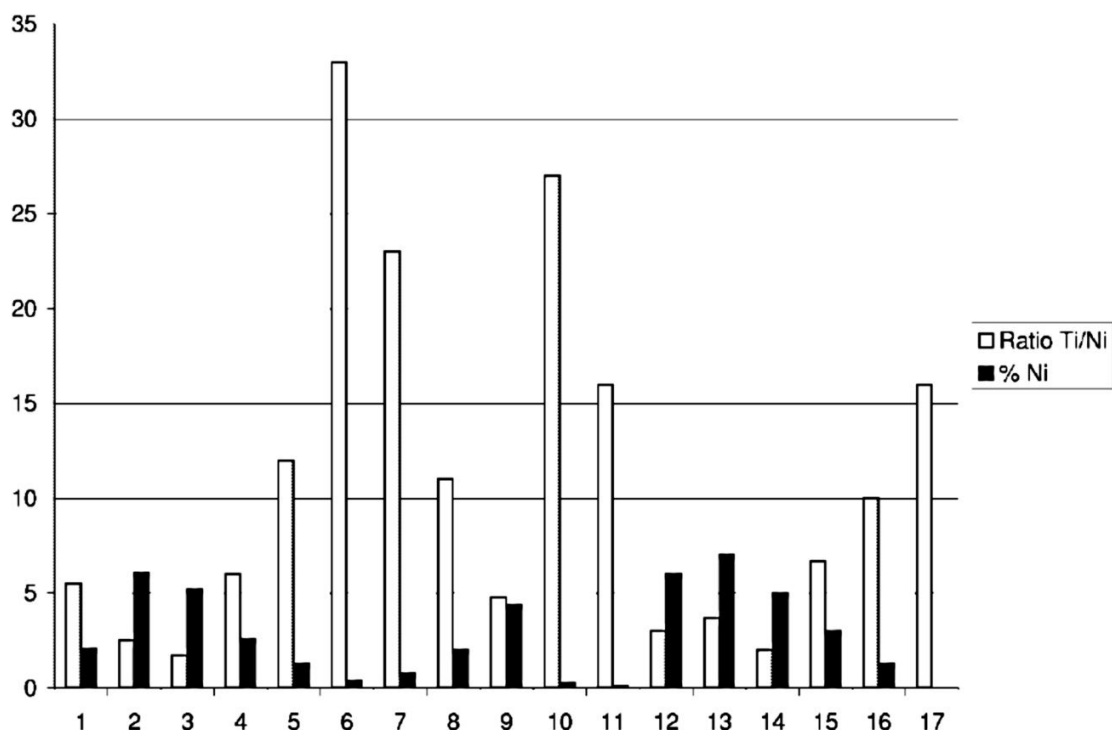


**Figure 2.14: The Ti/Ni ratio and Ni surface concentration for the following surface treatments: 1) MP, 2) MP and CE, 3-5) steam AC for 30, 60 and 120 minutes, 6) BW for 30 minutes, 7-9) water AC for 30, 99 and 180 minutes, 10) HPS for 22 hours, 11) EP, 12) EP and steam AC, 13) EP and dry heat, 14) EP and ethylene oxide, 15) EP and peracetic acid decontamination, 16) EP and hydrogen peroxide plasma and 17) EP and peracetic acid plasma. Figure adapted from [65, 91]**

## 2.3 Corrosion Analysis

Many techniques are available to characterize surface oxides and determine corrosion resistance of materials. The methods that are commonly used to analyze NiTi SMAs include, but are not limited to: (1) SEM and/or AFM to characterize surface morphology [74, 76, 87, 90, 93], (2) XPS and Auger analysis to determine the species present and/or depth of their penetration [74, 76, 87, 90, 92, 93], (3) XRD, Raman, and TEM analysis to determine crystallographic properties of oxides [15, 19, 74, 92], and (4) potentiodynamic cyclic polarization and/or Ni ion release to determine the stability of the oxide layer [15, 19, 76, 87, 90, 92, 93]. This study specifically looks at 3D topographical analysis, scanning electrochemical microscopy (SECM), Raman spectroscopy, and potentiodynamic cyclic polarization.

### 2.3.1 Fundamentals of SECM Analysis

A scanning electrochemical microscope consists of: (1) a conductive microelectrode (ME) encased in a insulating material so that only the tip of a known area is exposed, (2) an electrically conductive material to be analyzed (substrate), (3) a reference electrode, and (4) a redox-active material usually dissolved in a salt solution to enhance the conductivity between the electrode and the substrate. The ratio between the radius  $r_{\text{glass}}$  of the insulating sheath and the radius  $r_{\text{T}}$  of the active ME is known as the  $RG$  value. This value plays a significant role in the reaction kinetics, as will be shown later.

In the SECM feedback mode, a fixed potential is applied and a steady state current is measured while the ME is in the bulk solution. The mediator compound becomes electrolyzed at the ME tip. When the ME is near the substrate surface two possible outcomes can occur. First, the substrate could be insulating and inactive to the electrolyzed mediator. In this case, the substrate acts as a hindrance and reduces the current that can reach the ME (Figure 2.15). The second possibility is that the substrate is conductive and reacts with the electrolyzed mediator. The product of this reaction diffuses to the substrate where it can be reduced back to its original form. From the substrate, the mediator diffuses back to the ME where it increases the ME current depending on the distance  $d$  between ME and sample, diffusion coefficient  $D$  of the mediator and the effective heterogeneous rate constant  $k_{\text{eff}}$  (cm/s) at the sample.

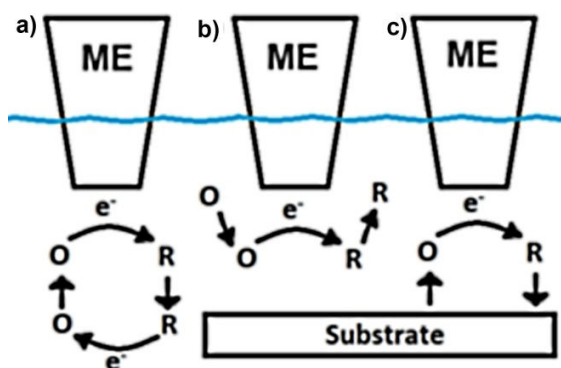


**Figure 2.15: Schematic showing the reactions that takes place at the ME tip a) in the bulk solution, b) at an insulating surface and b) at a conductive surface.**

The approach curves are measured by starting in the bulk solution and slowly moving the ME down to the sample surface. The approach is stopped when a sharp change of the current

occurs at the ME tip. The ME-NiTi electrode distance and ME current approach curve measurements are normalized to the steady state current ( $i_{T,\infty}$ ) measured in the bulk solution and ME radius ( $r_T$ ), respectively, using equations (2) and (3), respectively:

$$I_T = \frac{i_T}{i_{T,\infty}} \quad \text{(Equation 2)}$$

$$L = \frac{d}{r_T} \quad \text{(Equation 3)}$$

where  $I_T$  is the normalized ME current,  $i_T$  is the measured ME current,  $i_{T,\infty}$  is the steady state current,  $L$  is the normalized distance,  $d$  is the ME-NiTi electrode distance and  $r_T$  is the radius of the active ME.

To obtain the effective heterogeneous charge transfer rate constant ( $k_{\text{eff}}$ ), the normalized approach curves  $I_T$  vs.  $L$  are then fitted to the analytical approximation derived by Cornut and Lefrou [94] shown in equation (4) below:

$$I_T^k = I_{T,\text{con}} + \frac{I_{T,\text{ins}} - 1}{(1 + 2.47RG^{0.31}LA)(1 + L^{0.006RG+0.113}A^{-0.0236RG+0.91})} \quad \text{(Equation 4)}$$

where  $I_T^k$  is the analytical normalized current,  $I_{T,\text{con}}$  is the normalized positive feedback current,  $I_{T,\text{ins}}$  is the normalized negative feedback current,  $L$  is the normalized distance defined previously,  $RG$  is the ratio of radii defined previously, and  $A$  is the dimensionless substrate kinetics parameter.  $I_{T,\text{ins}}$  and  $I_{T,\text{con}}$  were calculated by using the analytical approximation for positive feedback current shown in equations (5) and (6) below [94]:

$$I_{T,\text{ins}} = \frac{\frac{2.08}{RG^{0.358}} \left( L - \frac{0.145}{RG} \right) + 1.585}{\frac{2.08}{RG^{0.358}} (L + 0.0023RG) + 1.57 + \frac{\ln(RG)}{L} + \frac{2}{\pi RG} \ln \left( 1 + \frac{\pi RG}{2L} \right)} \quad \text{(Equation 5)}$$

$$I_{T,\text{con}} = \alpha + \frac{\pi}{4\beta RG \tan^{-1}(L)} + \left( 1 - \alpha - \frac{1}{2\beta RG} \right) \frac{2}{\pi} \tan^{-1}(L) \quad \text{(Equation 6)}$$

where  $\alpha$  and  $\beta$  are defined by equations (7a) and (7b) below [94]:

$$\alpha = \ln 2 + \ln 2 \left( 1 - \frac{2}{\pi} \cos^{-1} \left( \frac{1}{RG} \right) \right) - \ln 2 \left( 1 - \left( \frac{2}{\pi} \cos^{-1} \left( \frac{1}{RG} \right) \right)^2 \right) \quad \text{(Equation 7a)}$$

$$\beta = 1 + 0.639 \left( 1 - \frac{2}{\pi} \cos^{-1} \left( \frac{1}{RG} \right) \right) - 0.186 \left( 1 - \left( \frac{2}{\pi} \cos^{-1} \left( \frac{1}{RG} \right) \right)^2 \right) \quad \text{(Equation 7b)}$$

The dimensionless substrate kinetics parameter  $\Lambda$  in equation 4 was calculated using equation (8) below [94]:

$$\Lambda = \frac{kr_T}{D} \quad (\text{Equation 8})$$

Where  $k$  is the rate constant of the redox reaction involving the mediator and  $D$  is the diffusion of the redox-active mediator.

### 2.3.2 Fundamentals of Potentiodynamic Cyclic Polarization Analysis

A basic potentiodynamic cyclic polarization test set-up consists of: (1) a reference electrode that exhibits a constant potential, (2) a working electrode which is the material to be tested and (3) a counter electrode. Any potential difference between the reference electrode and the working electrode creates a flow of current from the working electrode to the counter electrode [95].

As is the case with SECM, higher measured currents mean higher reactivity and lower measured currents mean lower reactivity. SECM uses a fixed potential and measures the local reactivity in a non-destructive manner, while cyclic polarization using a varying potential and characterizes the stability of the surface as a whole. The magnitude of the current depends on the surface area of the working electrode. Thus, it is useful to normalize the current with respect to the area across which it flows to yield the current density expressed in  $A/cm^2$ . The potential is cycled from low to high potential and then reversed back to the low value. When starting from a low potential, the first observable feature is a transition from a cathodic reaction to an anodic reaction. Typical cathodic reactions for a deaerated solution are hydrogen evolution, shown in equations (9a) and (9b) below:



The anodic reaction involves the anodic oxidation of the metal being studied, shown in equation (10) below:



where  $M$  represents the species that is being oxidized and  $n$  is the charge of the metal ion produced. The potential at which this reaction begins is known as the corrosion potential  $E_{\text{corr}}$ . The reaction occurs over a range of potentials. Figure 2.16 shows a graphical representation of the relationship between the cathodic and anodic reactions as well as a simulated polarization curve derived from the analytic relationship.

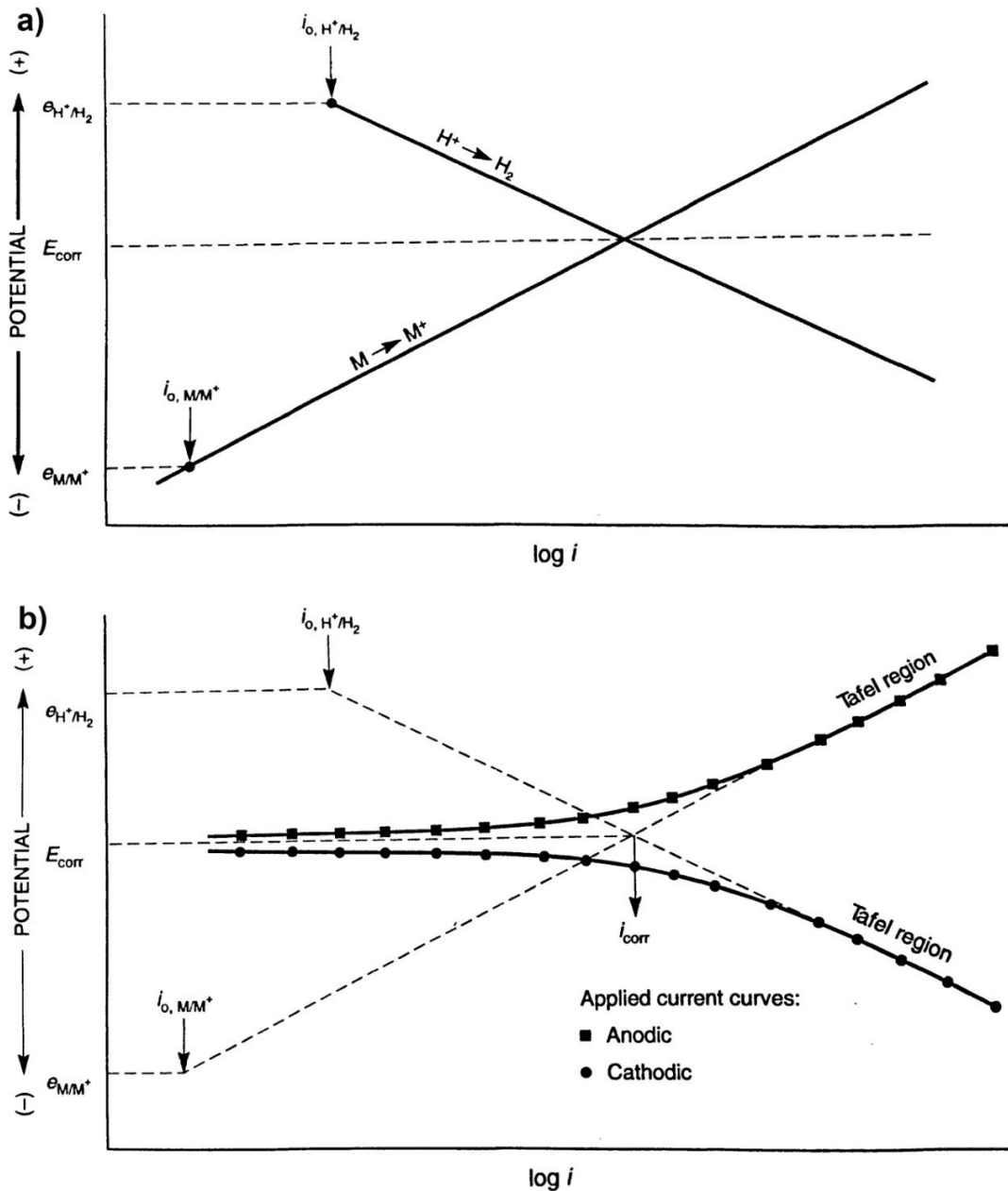
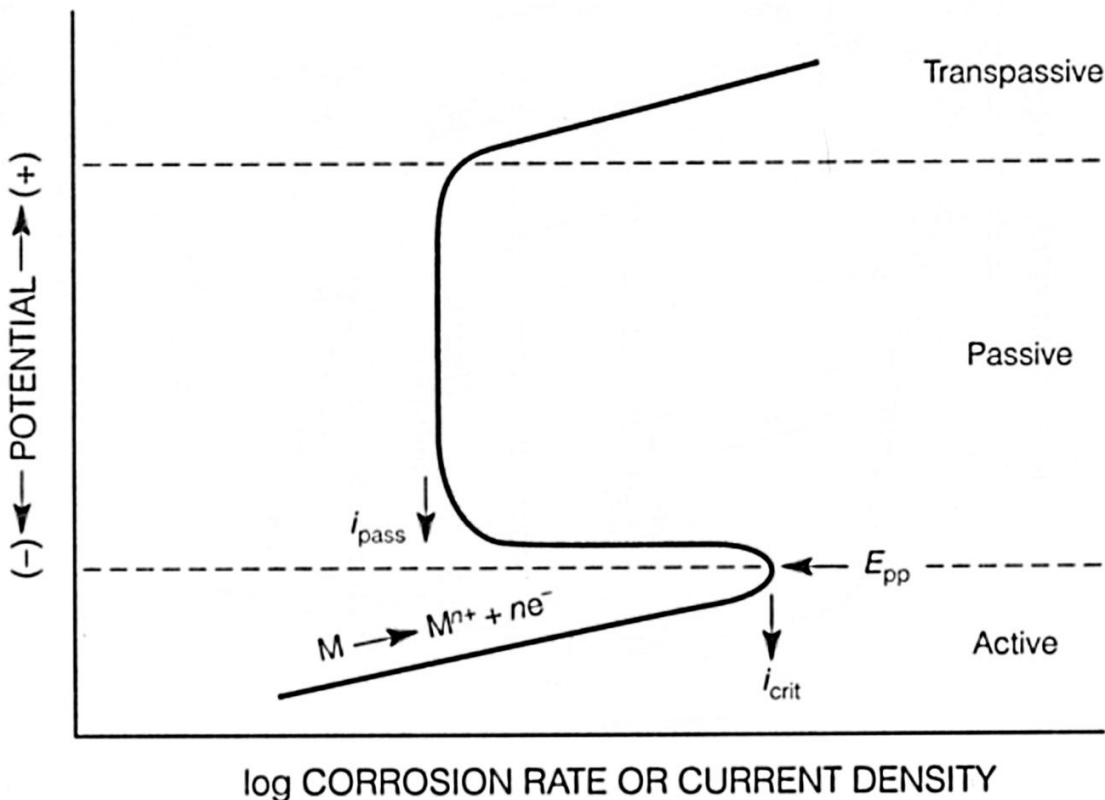


Figure 2.16: a) Analytic cathodic and anodic rates and b) simulated experimental polarization curves derived from a). Figure adapted from [96].

Increasing the potential above the Tafel region brings the sample into the passive region, as shown in Figure 2.17. In this range of potentials, the current density remains relatively constant and very low. Increasing the potential further can bring the sample to a transpassive region, where the passive layer becomes unstable and the anodic reaction increases again. Alternatively, H<sub>2</sub>O oxidation to O<sub>2</sub> can occur. The potential at which this transition occurs is defined as  $E_{\text{break}}$ , or the pitting potential. This typically takes place near the potential for oxygen evolution.



**Figure 2.17: Schematic of active-passive polarization behavior. Figure adapted from [96].**

For cyclic polarization, once the current density has increased to a predetermined value, the scan direction is reversed so that the potential is now decreased. This is done to determine the ability of the material to repassivate. When the crossover at the passive current density occurs, as shown in Figure 2.18, it is presumed that pits can no longer form. This crossover is defined as  $E_{\text{prot}}$ , or the repassivation potential. The size of the hysteresis between  $E_{\text{break}}$  and  $E_{\text{prot}}$  is important because the larger the hysteresis, the longer the material is corroding. Thus, a smaller hysteresis is desirable.

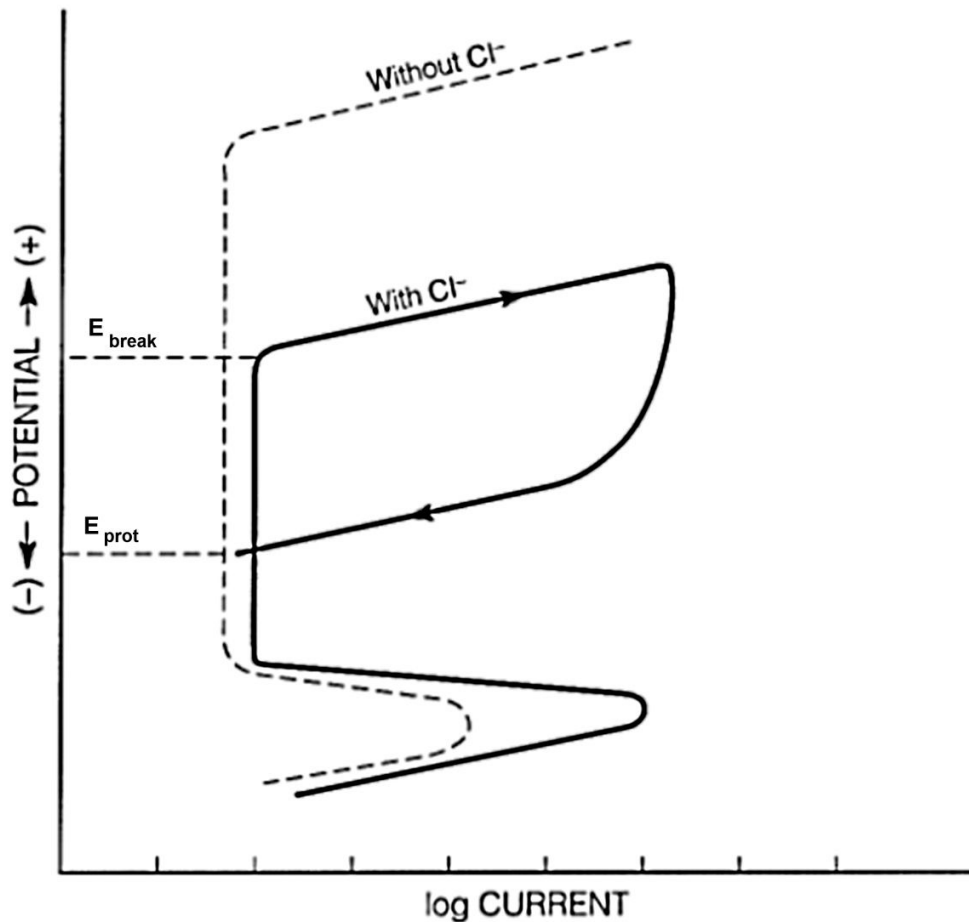


**Figure 2.18: Cyclic polarization curve showing  $E_{break}$  and  $E_{prot}$  (schematic). Figure adapted from [96].**

## 2.4 Laser Fundamentals

The word LASER is an acronym for Light Amplification by Stimulated Emission of Radiation. The light that is emitted is spatially and temporally coherent with very low diffraction, which can be coupled with transmittance optics to focus the high intensity beam into a single spot with a high energy density [97, 98]. A laser system is comprised of three main components: an amplifying medium, a means of exciting the medium to its amplifying state (pump source) and an optical resonator [98]. The amplifying medium consists of special materials that produce energy-carrying photons of specific wavelengths when excited. The pump source is determined by the type of active medium being used; the pump source for Nd:YAG is a flash lamp [98]. The optical resonator is composed of two parallel mirrors, one that is fully reflective and the

other that is partially reflective. They are placed around the active medium to filter and transmit photons that fully satisfy the specific requirements for oscillation [98].

When the laser is activated, atoms are energized from the ground state to the excited state by pumping. Incoherent photons are then emitted when the atoms relax back to the ground state. Photons that do not travel parallel to the optical axis of the laser are rapidly lost in the resonator; however, photons that do travel parallel to the optical axis are oscillated in the resonator with the possibility of inducing stimulated emission, which generates additional coherent photons [98]. By further populating the monochromatic with unidirectional photons, a highly energetic laser beam is created that is suitable for welding.

A population inversion, when the number of photons being amplified per unit time exceeds the number being absorbed, is required to amplify the quantity of light [99]. When a population inversion occurs in the cavity, the laser interacts with the excited atoms and lowers the energy level, concurrently releasing additional quanta of light [100]. If no population inversion occurs, the energy is absorbed from the laser to energize electrons, thus reducing the laser beam energy. After amplification, the beam is released through a partially reflective mirror in the cavity. A schematic of the laser cavity is shown in Figure 2.19.

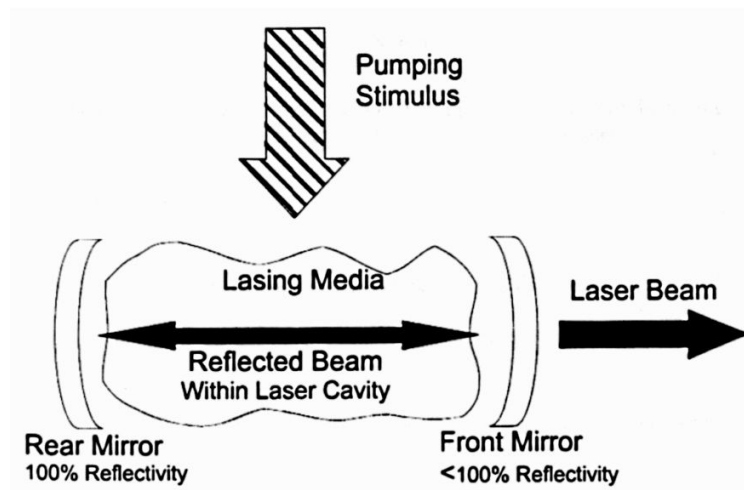


**Figure 2.19: Schematic showing how a laser cavity produces a laser beam [101].**

### **2.4.1 Pulsed Nd:YAG Laser Processing**

Each type of laser available generates light with a unique wavelength, which depends on the material used to make the semiconductor. They range from 0.1  $\mu\text{m}$  to 10  $\mu\text{m}$ , with Nd:YAG producing one of the shorter wavelengths available. The energy emitted by an Nd:YAG laser can be more efficiently absorbed by most materials and thus more efficiently melt a specific volume of material compared to other lasers. Nd:YAG lasers also produce photons that can be transmitted through glass, enabling flexibility with beam transfer by way of fiber optics.

A stable power output paired with a high power density makes pulsed Nd:YAG laser ideal for many industrial applications. Pulsed Nd:YAG laser welding is commonly used for fusion welding to generate deep welds with low average heat input. Commercially available Nd:YAG lasers are generally rated with average output powers from 0.3 kW to 3 kW, which is ideal for small scale use [98].

A schematic of a Nd:YAG laser system is shown in Figure 2.20. The cavity assembly is composed of an active medium, pumping source, and resonator. When excited, an yttrium aluminum garnet (YAG) crystal doped with neodymium (Nd) atoms produces photons with a wavelength of 1064 nm [98]. The excitation radiation is pumped using flash lamps. The laser output is transmitted through the input coupling optic and into an optical fiber connected to the working head before being delivered to the workpiece. The capability of delivering photons via fiber optics is advantageous for fabrication of complex components. Other advantages include higher processing efficiency, ability to create narrow welds with small heat-affected zones (HAZ) and the capacity to weld special materials such as titanium and quartz [97, 98].

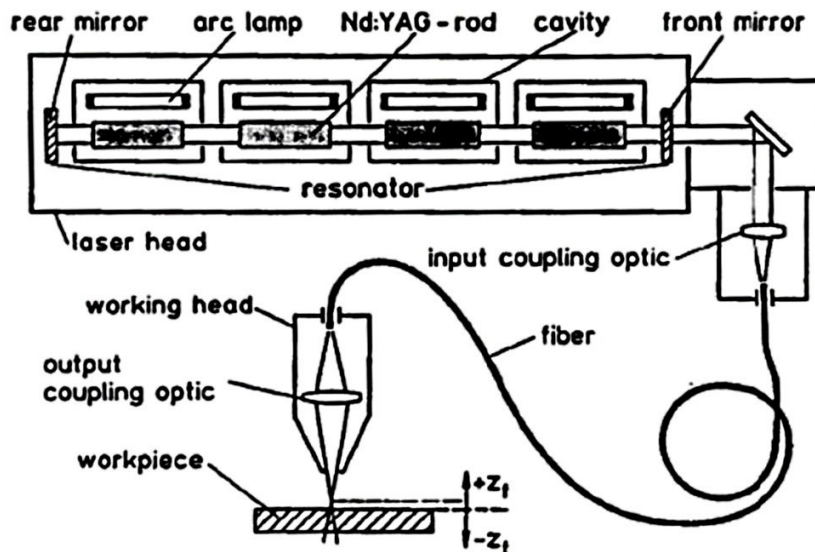
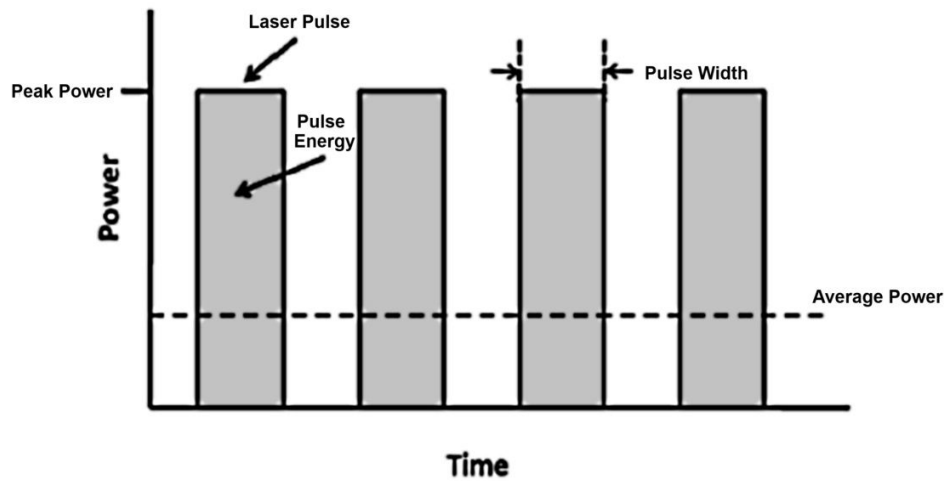


Figure 2.20: Schematic of Nd:YAG laser setup [32].

## 2.4.2 Processing Parameters

Several key parameters characterize the laser pulses produced by a Nd:YAG laser, including pulse width, peak power, frequency, travel speed and defocus distance. For spot welding, individual pulses are defined by the peak power and pulse width. For seam welding, the amount of overlap between individual pulses is controlled by the frequency and weld speed. Figure 2.21 shows a schematic of a temporal profile of laser pulses produced with the Nd:YAG laser process. Peak power is the maximum power of the laser pulse and weld width is the duration of the laser pulse, which typically varies from 0.2 to 20 ms. Pulse energy is determined by the area under each laser pulse in Figure 2.21. The average power transferred to the workpiece is a function of pulse energy and frequency. However, substantial energy losses due to factors such as reflection can occur, making it difficult to exactly quantify the energy absorbed by the workpiece [32]. Optimization of these parameters defines the process window for producing acceptable welds.



**Figure 2.21: Schematic of pulsed Nd:YAG output [32].**

The advantage of laser processing is the ability to achieve a high energy density, and maximize penetration of the workpiece. This is achieved by focusing the light to a minimum beam waist diameter, or focusing the spot size at the zero defocus distance [98], as shown in Figure 2.22. An offset from this distance defocuses the light, resulting in a decrease in the power density. Focus spot size depends on the combined effects of optics, laser characteristics and welding parameters. The focus position relative to the workpiece depends on the welding mode (see Section 2.4.4 Laser Beam Modes), geometry and the use of filler metal [98]. The general rule is to focus at a distance where the maximum penetration depth is attained through experimental verification. A laser operating in its convergence range has the highest energy efficiency.

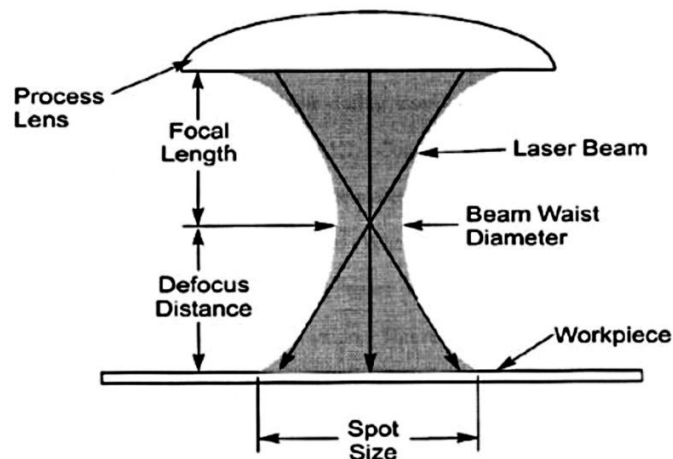


**Figure 2.22: Schematic of the propagation and convergence of a laser beam [101].**

### **2.4.3 Shielding Gas**

Since most welded materials typically oxidize, a shielding gas of argon or helium is generally used to prevent a reaction of oxygen or nitrogen with the molten weld pool. Oxide inclusions are most often detrimental to the material properties [97, 98]. This is extremely important for NiTi SMAs, which have a high affinity for oxygen and, to a lesser extent, nitrogen. Selection of the proper shielding gas has also been shown to enhance the transmission of the incident laser beam for absorption by the workpiece [99].

### **2.4.4 Laser Beam Modes**

The incident laser beam is absorbed in one of two modes during laser welding – conduction and keyhole, as shown in Figure 2.23. During conduction mode, the laser intensity is only sufficient to melt the workpiece. The pool first forms at the surface and grows due to conduction in all directions, which results in a semi-elliptical shape [32]. Since the laser energy is only absorbed by the top surface of the material, reflection can greatly reduce the amount of energy absorbed by the material. Keyhole mode occurs when the peak temperature at the surface is high enough to vaporize the workpiece material. Keyhole depression in the molten pool is produced by the pressure of vaporization [32]. This is a more efficient method of transferring energy into the workpiece since the keyhole traps the laser energy and the internal reflectivity within the keyhole acts as a blackbody.

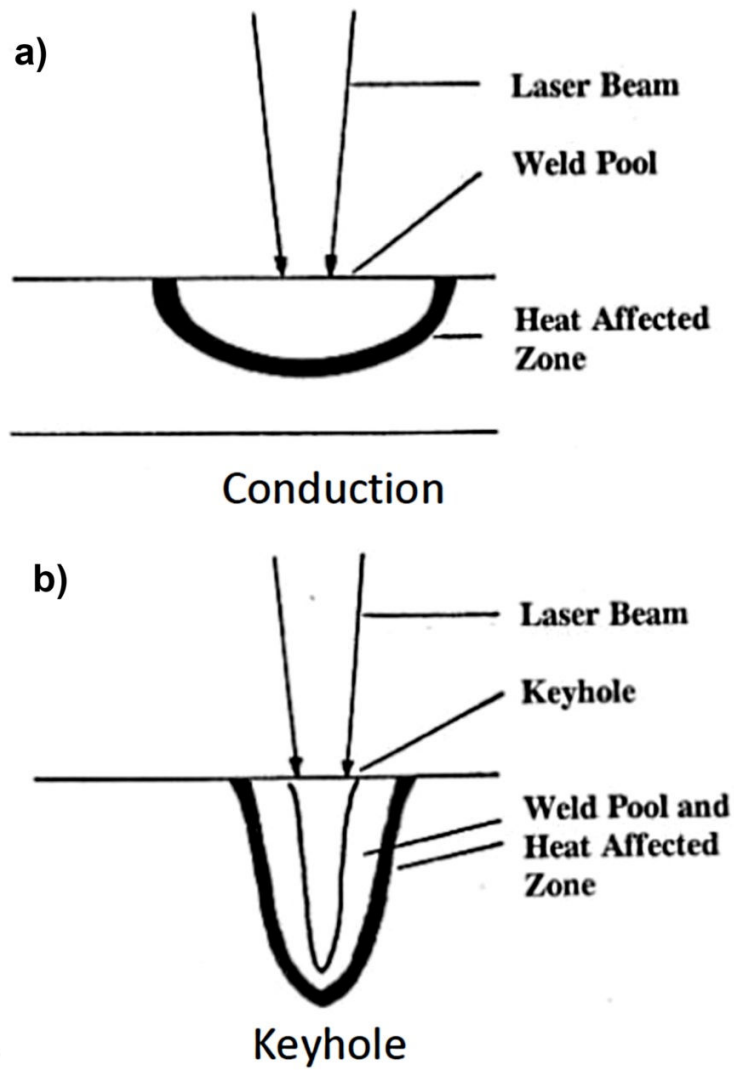


Figure 2.23: Comparison of a) conduction and b) keyhole welding modes [97].

## **Chapter 3: Experimental Methods**

### **3.1 Material Selection**

This study used 0.37 mm thick by 12 mm wide SE508 NiTi strips that are commercially available from Nitinol Devices and Components (NDC), Inc. Their chemical composition was 55.8 wt.% (50.7 at.%) Ni and 44.2 wt.% (49.3 at.%) Ti with a maximum O and C content of 0.05 wt.% and 0.02 wt.%, respectively, as reported by the manufacturer. Prior to testing, the NiTi strip was ultrasonicated in a 7.5 vol. % HF, 20 vol. % HNO<sub>3</sub>, bal. H<sub>2</sub>O solution for 2 minutes, turning upside-down after 1 minute, to remove the thick black oxide layer that forms during manufacturing. After chemically etching, the cross-sectional thickness was measured to be 0.35 mm. For the remainder of this study, the chemically etched state is referred to as ‘CE.’

### **3.2 Laser Processing Equipment and Parameters**

A LW50 A Miyachi pulsed Nd:YAG laser system with a 1.06 μm wavelength and a 600 μm nominal spot size was used in this study. This system was equipped with a power monitor, which allowed for accurate in situ measurement of incident power output. Laser processing was done on monolithic NiTi sheets with the top and bottom shielded with argon to avoid oxidation. A flow rate of 14.2 L/min (30 CFH) was used for this study. The laser processing setup, including fixtures, is shown in Figure 3.1. The CE strip was cleaned with acetone, ethanol and then de-ionized water prior to laser processing to remove any surface contaminants.

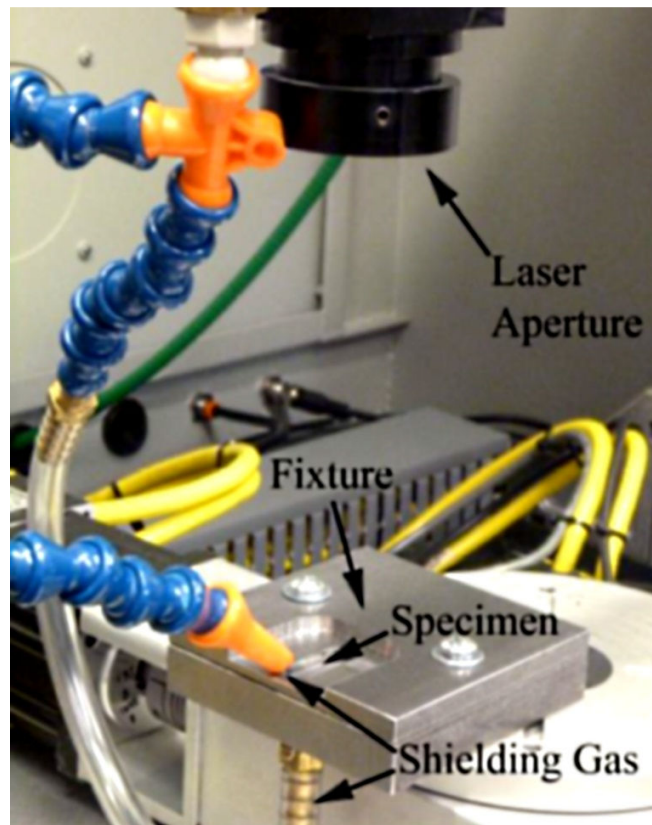


**Figure 3.1: Laser processing setup. NiTi strip was clamped in the fixture with Ar gas shielding the top and bottom to prevent oxidation. [50]**

The following pulsed laser protocol was used: a peak power of 0.8 kW for 6 ms, followed by a linear ramp down to 0.0 kW over 4 ms, as shown in Figure 3.2a. This protocol was developed in a previous study [50]. For the first part of the study, the laser spots were pulsed one through five times in a single spot to investigate the change in surface reactivity with increased laser pulsing. This material state will be referred to as the “laser processed” (LP) state for the remainder of this study, with a number preceding ‘LP’ to indicate the number of pulses used. For the second part of the study, the laser pulses were overlapped by approximately 50 %, as shown in Figure 3.2b. This material state will be referred to as the “laser processed with overlap” (LPO) state for the remainder of this study, with a number preceding ‘LPO’ to indicate the number of pulses used in each spot. After laser processing, samples were cleaned again with acetone, ethanol and de-ionized water prior to testing in order to remove any surface deposits from laser processing.

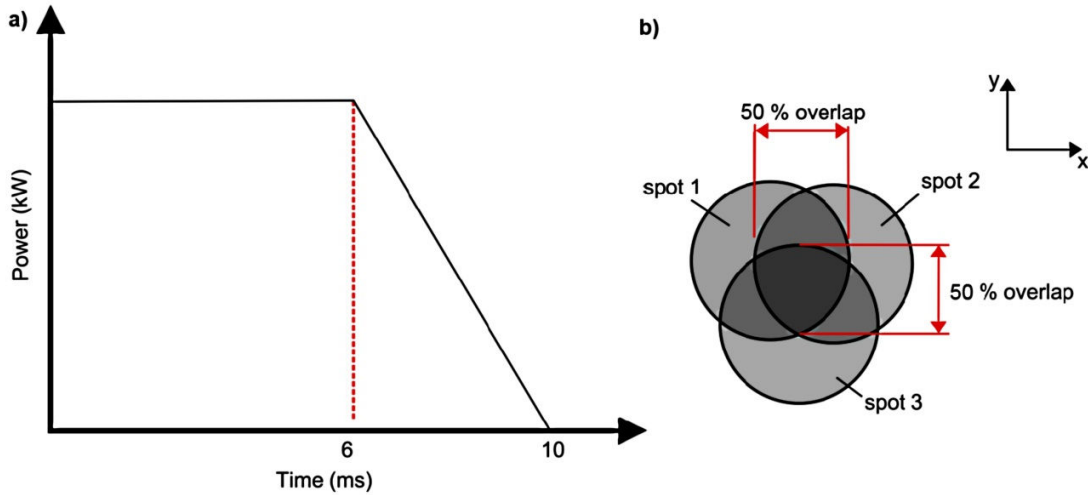


**Figure 3.2: a) Laser processing schedule and b) schematic of 50 % overlap of laser processed spots. Figure adapted from [50].**

### 3.3 Post-Process Surface Treatment

Each post-process surface treatment was performed on 5LPO samples, as this was deemed to be the worst case scenario. The first method used was MP. After laser processing, strips were cut in  $8 \times 8 \text{ mm}^2$  pieces and progressively ground with 600, 800, 1200 coarse, and 1200 fine grit silicon carbide paper. Polishing was then performed with a  $0.03 \text{ }\mu\text{m}$  colloidal silica suspension and 30% hydrogen peroxide mixture (9:1 ratio). This state will be referred to as the “laser processed and mechanically polished” state (LPMP) for the remainder of this study. Extreme care was taken to use consistent grinding/polishing protocol for each individual specimen. The other method tested was CET. The samples were immersed in a mixture of 15% HF, 40% HNO<sub>3</sub>, and 45% DI water for 30 seconds, and then immediately sonicated in DI water for 10 minutes. This state will be referred to as the “laser processed and chemically etched” state (LPCE) for the remainder of this study. Both of these treatments were followed by a boiling water treatment to determine how significant an effect this treatment would have on the surface oxide. These states will be referred to as the “laser processed, mechanically polished, and boiled in water” state (LPMPBW) and the “laser processed, chemically etched, and boiled in water” state (LPCEBW), respectively. The LPMPBW samples were boiled in water for 1 hour due to the higher Ni content of the surface oxide formed by mechanically polishing (see Section 2.2.3 Mechanical Polishing). The LPCEBW samples were boiled in water for 30 minutes, which is a typical treatment time (see Section 2.2.5 Boiling Water).

## 3.4 Analytical Methods

### 3.4.1 Surface Analysis

The surface topography was characterized using the Nanovea ST400 Optical Profilometer, which is a 3D non-contact profiler that was not affected by sample reflectivity. This is important due to the variation in reflectivity across the sample surface. Three dimensional topographical surface maps of the samples were obtained by rastering the optical pen over a  $1.2 \times 1.2 \text{ mm}^2$  area using a step size of  $5 \text{ }\mu\text{m}$ . The surface roughness was calculated by equation (11) below:

$$R_a = \sum \frac{|Z_i|}{N} \quad (\text{Equation 11})$$

where  $R_a$  is the average roughness,  $Z_i$  is the height difference from the mean at the  $i^{\text{th}}$  location and  $N$  is the number of data points measured. High-magnification optical microscopy was done with an Olympus BX51M upright inspection and research microscope. Low-magnification optical microscopy was performed using a Leica A60 S Stereomicroscope and a PAX cam LM2 digital camera using Seagull image capture software.

### 3.4.2 Scanning Electrochemical Microscopy

The Scanning Electrochemical Microscopy (SECM) analysis was carried out using a HEKA scanning electrochemical microscope (HEKA Elektronik, Germany). The sample was fixed to the bottom of a Teflon cell. A  $25 \text{ }\mu\text{m}$  diameter platinum microelectrode (ME) was utilized as the working electrode, a chloridized silver wire as a quasi-reference electrode (Ag|AgCl-QRE) and a  $0.5 \text{ mm}$  diameter platinum wire as a counter electrode (Goodfellow Cambridge Limited, Huntingdon, England). A ME was fabricated in-house (McGill University, Montreal, Quebec) by sealing a Pt wire ( $25 \text{ }\mu\text{m}$  diameter, Delta Scientific Laboratory Products Ltd., Canada) into a borosilicate glass capillary having an outer diameter of  $1.5 \text{ mm}$  and inner diameter of  $0.7 \text{ mm}$  (Sutter Instrument, USA). The probe tip was subsequently sharpened to a ratio  $RG \approx 10$ . The resulting Pt MEs were polished on a microcloth pad (Struers MD Chem cloth) using a series of water-based alumina slurries (i.e.  $1 \text{ }\mu\text{m}$ ,  $0.3 \text{ }\mu\text{m}$  and  $0.05 \text{ }\mu\text{m}$ ). The working solution was

composed of 1 mM FcMeOH as redox-active mediator and 0.1 M K<sub>2</sub>SO<sub>4</sub> as the supporting electrolyte in ultra-pure water (Millipore MiliQ water 18.2 MΩ).

SECM feedback images (1.2 × 1.2 mm<sup>2</sup> area) were acquired with the ME probe positioned at a tip-to-substrate distance of 10 μm relative to the highest topographic feature on the surface and using a x,y-scan rate of 5 μm/s. Line scans of the ME-NiTi electrode distance were normalized using equation (3), where  $d$  (the ME-NiTi electrode distance) was calculated to be 30 – h, where h is the measured height (μm) (since the highest topographic feature was 20 μm and the probe was 10 μm above). To decouple topography effects from the electrochemical reactivity, the theoretical dimensionless ME current ( $I_T^k$ ) was calculated across the line scan from equation (4). The rate constant  $k$  was calculated by first principles using equation (12) below:

$$k = \frac{i_T L}{FAC} \quad \text{(Equation 12)}$$

where  $i_T$  is the measured ME current at each location in the line scan,  $L$  is the dimensionless ME-NiTi distance,  $F$  is the Faraday constant,  $A$  is the exposed surface area of the ME and  $C$  is the concentration of the redox-active mediator. The concentration of the redox-active mediator was assumed to be constant and  $L$  was used to account for the distance between the ME and substrate.

The approach curves in a 1 mM FcMeOH/0.1 M K<sub>2</sub>SO<sub>4</sub> solution were acquired according to the following scheme. The ME tip was polarized at  $E_T = 0.4$  V vs Ag|AgCl-QRE to allow for mass transport-controlled oxidation of FcMeOH into FcMeOH<sup>+</sup> as the sample was maintained at its rest potential. The ME was moved down to the sample surface at an approach speed of 2 μm/s. The approach was stopped when a sharp change of the current at the ME tip was measured. The ME-NiTi electrode distance and ME current approach curve measurements were normalized to the steady state current ( $i_{T,\infty}$ ) and ME radius ( $r_T$ ), respectively, using equation (2) and equation (3), respectively.

The normalized approach curves  $I_T$  vs.  $L$  were then fitted to the analytical approximation of Cornut and Lefrou [94] shown in equation (4) to obtain the effective heterogeneous charge transfer rate constant ( $k_{\text{eff}}$ ). The experimental steady state current  $i_{T,\infty}$  was 3.147 nA and the

diffusion coefficient  $D$  of the redox-active mediator was determined experimentally to be  $7.6 \times 10^{-6} \text{ cm}^2/\text{s}$ .

### 3.4.3 Raman Spectroscopy

In Raman spectroscopy, the sample is radiated by a laser beam in the UV-visible wavelength region. The scattered light is usually observed in the direction perpendicular to the incident beam. Raman spectra are measurements of the vibrational frequency  $\nu_m$  of the sample as a shift from the incident beam frequency  $\nu_o$  [102]. The vibrational frequency measured corresponds to the vibrational frequency of bonds present in the material being analyzed. For this study, the vibrations measured would be indicative of the presence of crystals, which would contain several bonds with the same frequency. An amorphous structure would have a random orientation and no significant peak would be observed. The Raman spectrometer used for this experiment was a Renishaw ramanscope with a resolution of  $\leq 1 \text{ cm}^{-1}$ . The spectra were obtained with a He-Ne laser operating at 633 nm with an incident power of 7.5 mW and a 5  $\mu\text{m}$  spot size. The wavelength calibration was made using the silicon emission line at  $520 \text{ cm}^{-1}$ .

### 3.4.4 Cyclic Potentiodynamic Polarization

Corrosion performance was determined through cyclic potentiodynamic polarization testing. The ASTM F2129-08 [103] standard for cyclic polarization testing of NiTi materials was used as a reference for the test setup. The reference electrode was a saturated calomel electrode (SCE) in a KCl salt bridge ( $233 \pm 10 \text{ mV}$  versus SHE in  $37 \text{ }^\circ\text{C}$ ) and the counter electrode was a platinum wire mesh. The working electrode consisted of a custom made sample holder that exposed a  $0.25 \text{ cm}^2$  surface area of the specimen by way of a rubber gasket and a Teflon® cap. The back side of the specimen was in contact with a brass rod, as shown in Figure 3.3. The sample holder was made following the ASTM standard [103, 104].

In order to mimic body conditions, a phosphate buffered saline (PBS) electrolyte with pH 7.4 (MP Biomedicals) was used within a 250 mL double-walled corrosion cell (Figure 3.4) maintained at  $37 \text{ }^\circ\text{C}$  throughout the test. The chemical composition of the PBS was 8.0 g/L NaCl, 0.2 g/L KCL, 1.15 g/L  $\text{Na}_2\text{HPO}_4$ , and 0.2 g/L  $\text{KH}_2\text{PO}_4$ . The PBS electrolyte was de-aerated with nitrogen at a flow rate of 50 mL/min for 30 minutes prior to testing and then

continuously throughout the test. The open-circuit potential (OCP) was measured for up to one hour, or until it was stable within 0.05 mV/s. The test was performed at a scan rate of 0.167 mV/s, according to the ASTM standard [103, 105]. The scan started at -0.6 V and increased to 1.4 V, automatically reversing if the current density exceeded 0.1 mA/cm<sup>2</sup>. A GAMRY Instruments Series G-300 potentiostat with Framework v4.5 software was used for voltage control and data acquisition. Four samples of each surface condition were tested and representative curves are shown; all data are provided in Appendix III: Experimental Data for Cyclic Polarization Tests.

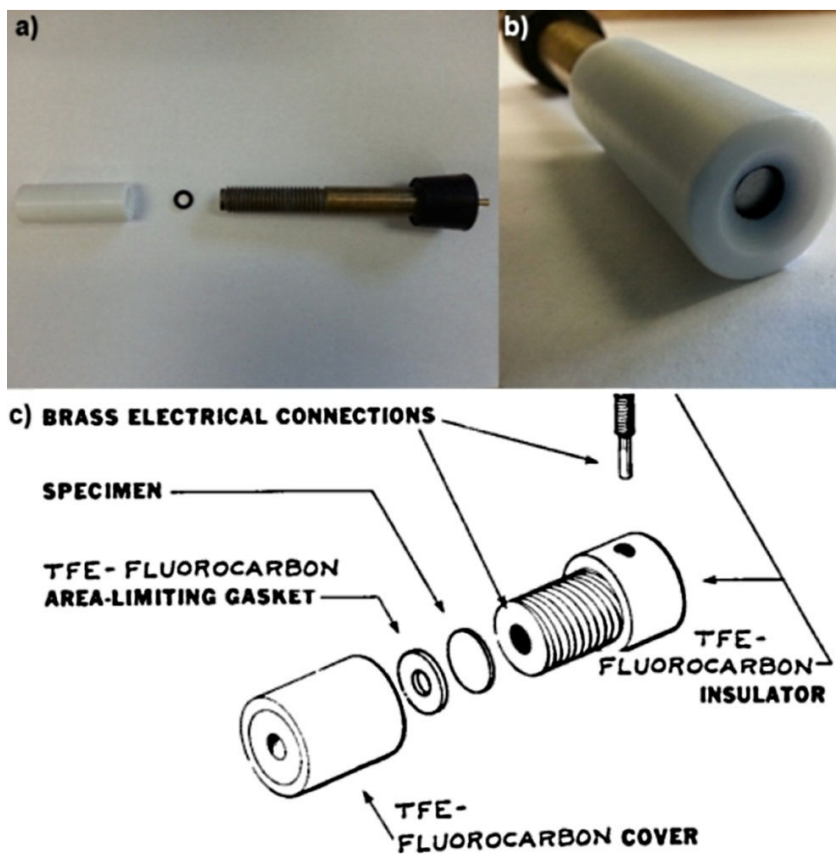


**Figure 3.3: a) The components of custom-made working electrode (Teflon cap, rubber gasket and brass rod), b) assembled working electrode and c) ASTM standard configuration of similar set-up [104].**

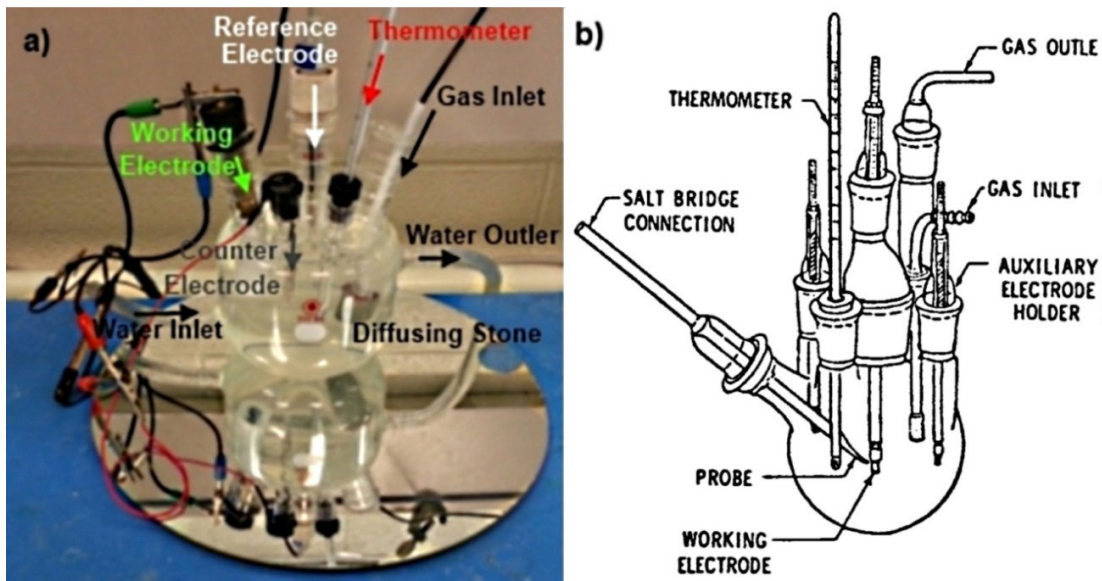


**Figure 3.4: a) Corrosion cell used for cyclic potentiodynamic polarization test compared with b) standard set-up for cyclic polarization testing of implants [105].**

Analysis of the cyclic polarization curves was done with GAMRY Echem Analyst Version 5.61 software. In order to perform the Tafel extrapolations, the sample density and equivalent weight had to be determined. The average density of the samples was found to be  $6.45 \text{ g/cm}^3$ . The equivalent weight for the NiTi alloy was calculated using equation (13) below from ASTM Standard G102-89 [106]:

$$EW = \frac{1}{\sum \frac{n_i f_i}{W_i}} \quad (\text{Equation 13})$$

where  $EW$  is the equivalent weight,  $n_i$  is the valence of the  $i^{\text{th}}$  element in the alloy,  $f_i$  is the mass fraction of the  $i^{\text{th}}$  element in the alloy and  $W_i$  is the atomic weight of the  $i^{\text{th}}$  element in the alloy. The equivalent weight for NiTi SMA was calculated to be 17.15 and was used to perform Tafel analysis using Echem Analyst software. The corrosion current density was calculated using the equation (14) below [106]:

$$i_{corr} = \frac{I_{corr}}{A} \quad (\text{Equation 14})$$

where  $i_{corr}$  is the corrosion current density in  $\mu\text{A/cm}^2$ ,  $I_{corr}$  is the total current density in  $\mu\text{A}$ , and  $A$  is the exposed surface area in  $\text{cm}^2$ .

# **Chapter 4: Evolution of Surface Structure after Laser Modification**

## **4.1 Effects of Single Spot Laser Pulsing**

In this part of the study, specific focus was given to the localized surface reactivity characterized using the SECM techniques. The SECM technique, developed during the late 80's by Bard's group [107], has rapidly emerged as a highly promising and useful method to investigate electrochemical and morphological characteristics of surfaces at a more local scale (typically micrometric). Many topics have been investigated ranging from classical surface science to biological and medical [108-112]. SECM is also considered a valuable tool for local electrochemical characterization of thin passive oxide layers covering numerous metals and alloys, as reported by several research groups on the behavior of the oxide films of Ti and its alloys [113-116]. Already a few studies have examined NiTi materials by SECM. Belger et al. [117] used AC-SECM to examine electropolished NiTi and found the surface to be highly uniform and passivating. Schulte et al. [115] examined mechanically polished NiTi surfaces by AC-SECM and found lateral variations in electrochemical activity that was the precursor to pitting. Ruhlig et al. [118] performed AC-SECM analysis of similar and dissimilar welds of NiTi and stainless steel; however, their analysis was performed on polished cross-sections, not native surfaces. They found no significant difference between the weld zone and the base material of the polished cross-sections of NiTi-NiTi welds.

The goal of this study is to determine the evolution of the surface oxide with an increased number of pulses on a single spot from a Nd:YAG laser. The surface properties were analysed by optical profilometry and SECM. Raman spectroscopy was used to determine the crystallinity of the surface oxide after laser pulsing. Potentiodynamic cyclic polarization was used to determine the stability of the oxide after laser pulsing.

### **4.1.1 Surface Morphology**

Analyse of the surface morphology prior to SECM analysis is crucial to ascertain how much the surface topography affects SECM feedback measurements. Surface topography was

measured by a contactless profilometer. The 3D topographical profiles of the individual spots are shown in Figure 4.1a. The  $R_a$  values were calculated to be 1.45  $\mu\text{m}$  (1LP), 1.62  $\mu\text{m}$  (2LP), 1.71  $\mu\text{m}$  (3LP), 1.25  $\mu\text{m}$  (4LP), 2.54  $\mu\text{m}$  (5LP) and 2.18  $\mu\text{m}$  (CE). The surface roughnesses of all of the LP samples are comparable to that of the CE surface. The laser spots themselves are observed to be smoother than the chemically etched material surrounding it, similar to the findings of other laser processing studies [15]. A slightly elevated region is observed in the center of all the spots due to the pressure drop associated with keyhole laser welding. Ripples are also observed in the re-melted region, and increase in intensity with the number of pulses.

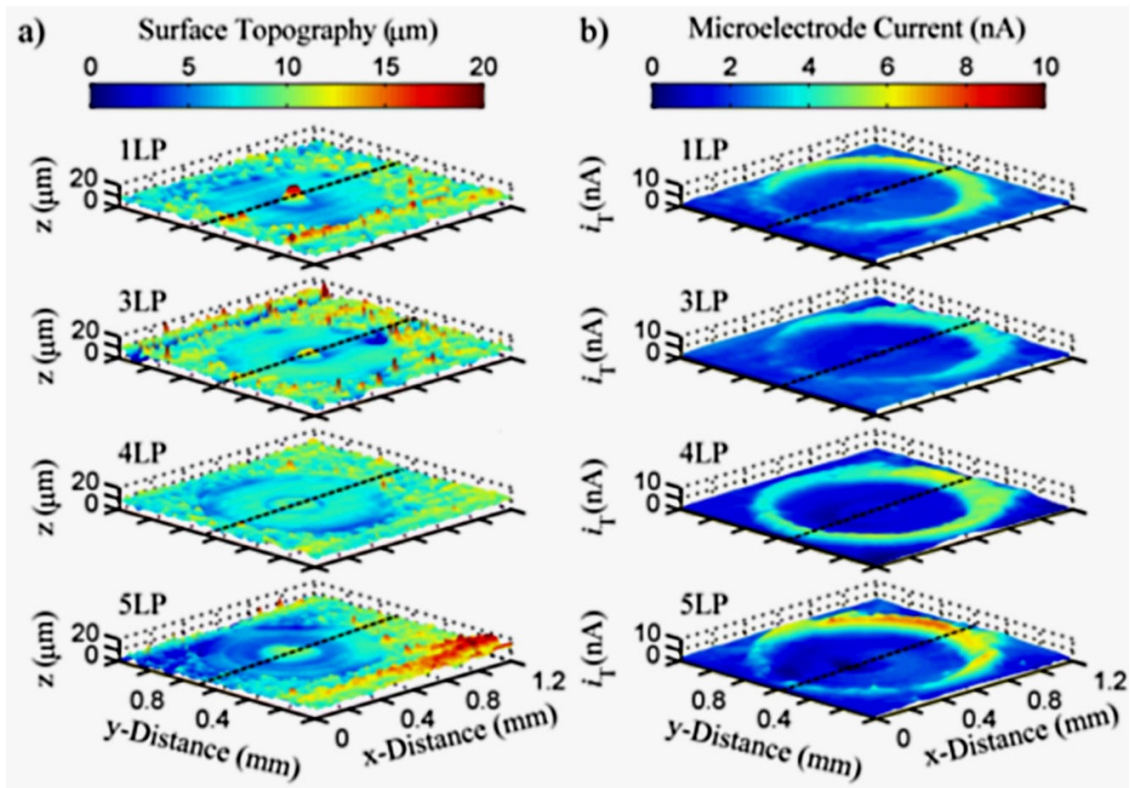


**Figure 4.1: a) Surface topography maps and b) SECM feedback images of 1LP, 3LP, 4LP and 5LP samples. Dashed lines correspond to line scans in Figure 4.3. (SECM analysis courtesy of Dr. Ushula Tefashe, McGill University)**

#### 4.1.2 SECM images in the feedback mode

The SECM images of the NiTi sample surfaces obtained in the feedback mode are shown in Figure 4.1b. After only one laser pulse, a ring of increased reactivity exists adjacent to the re-melted region (*vide infra*). This corresponds to the HAZ found around the weld pool region

and is consistent with the studies by Chan et al. [21] and Pequegnat et al. [22] who observed preferential corrosion adjacent to pulsed laser spots. Increasing the number of pulses tends to increase the intensity of ME current as well as the area in which higher current was observed. The high current areas were estimated to be  $0.27 \text{ mm}^2$  for 1LP,  $0.30 \text{ mm}^2$  for 3LP,  $0.34 \text{ mm}^2$  for 4LP and  $0.40 \text{ mm}^2$  for 5LP. The growth of the annular region of higher ME current was not uniform (Figure 4.1) suggesting it may not result entirely from the formation of a HAZ. The trailing edge to the right of the re-melted region corresponds to the plume deposits that form on the surface during laser processing, as is clearly observed in the optical image of the laser spot pre-cleaning as shown in Figure 4.2a. Note the removal of the black plume deposit to the right of the laser spot after cleaning (Figure 4.2b). This agrees with previous studies that observed Ni-enriched plume deposits after laser pulsing of NiTi SMAs [13].

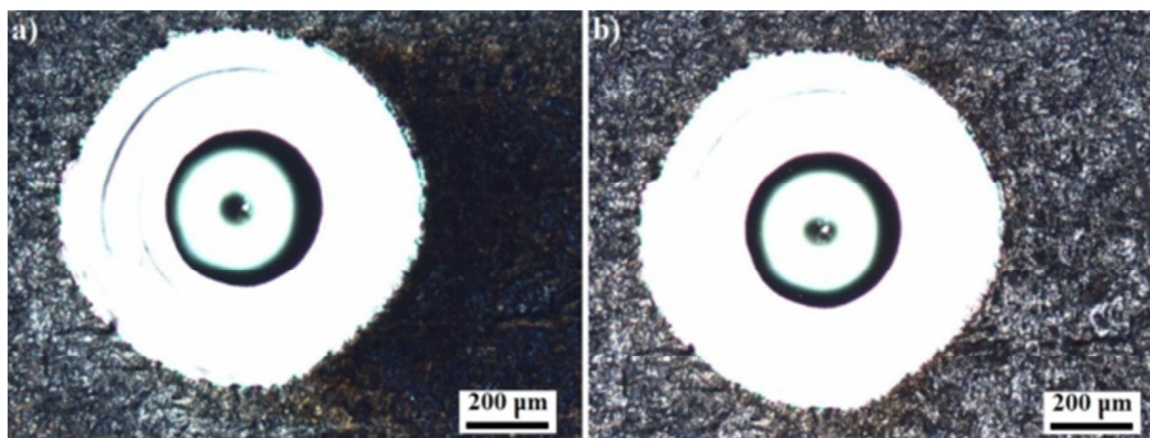


**Figure 4.2: Optical images of a laser processed sample a) with post-process Ni deposits on surface and b) after cleaning thoroughly with acetone, ethanol, and de-ionized water**

It can be seen that CE/re-melted regions of the NiTi surface provide small ME current and that of the HAZ region provide a large current response, with a measured current in excess of the bulk solution. In the centre of the laser spots as well as in the HAZ/CE regions, topographic variations on the order of  $7 \mu\text{m}$  are observed. The general patterns observed in the SECM images are consistent with those of the topography images, although the measured current reflects the combined effects of reactivity and topography. Thus, we expect to observe a significant surface topography effects coupled to the regeneration reaction at the center of re-melted region in 1LP and 3LP samples (Figure 4.1b), where increased topographic heights result in a more pronounced decrease in  $i_T$  as the ME scanned above the surface. To decouple

topography effects from the electrochemical reactivity, the theoretical dimensionless current ( $I_T^k$ ) is compared with the dimensionless ME-NiTi substrate distance ( $L$ ). Figure 4.3 compares  $I_T^k$  and  $L$  line scans through the center of the samples corresponding to the dashed lines in Figure 4.1. The resulting  $I_T$  is significantly reduced in the re-melted/CE regions, which demonstrates that the decoupling procedure successfully removed the topographical component from the total current and allowed for the extraction of the mediator regeneration contribution. At the center of the re-melted region, the  $I_T^k$  values are 0.61, 0.69, 0.83 and 0.66 for 1LP, 3LP, 4LP and 5LP respectively. These values were consistent with those obtained the non-reactive CE region.

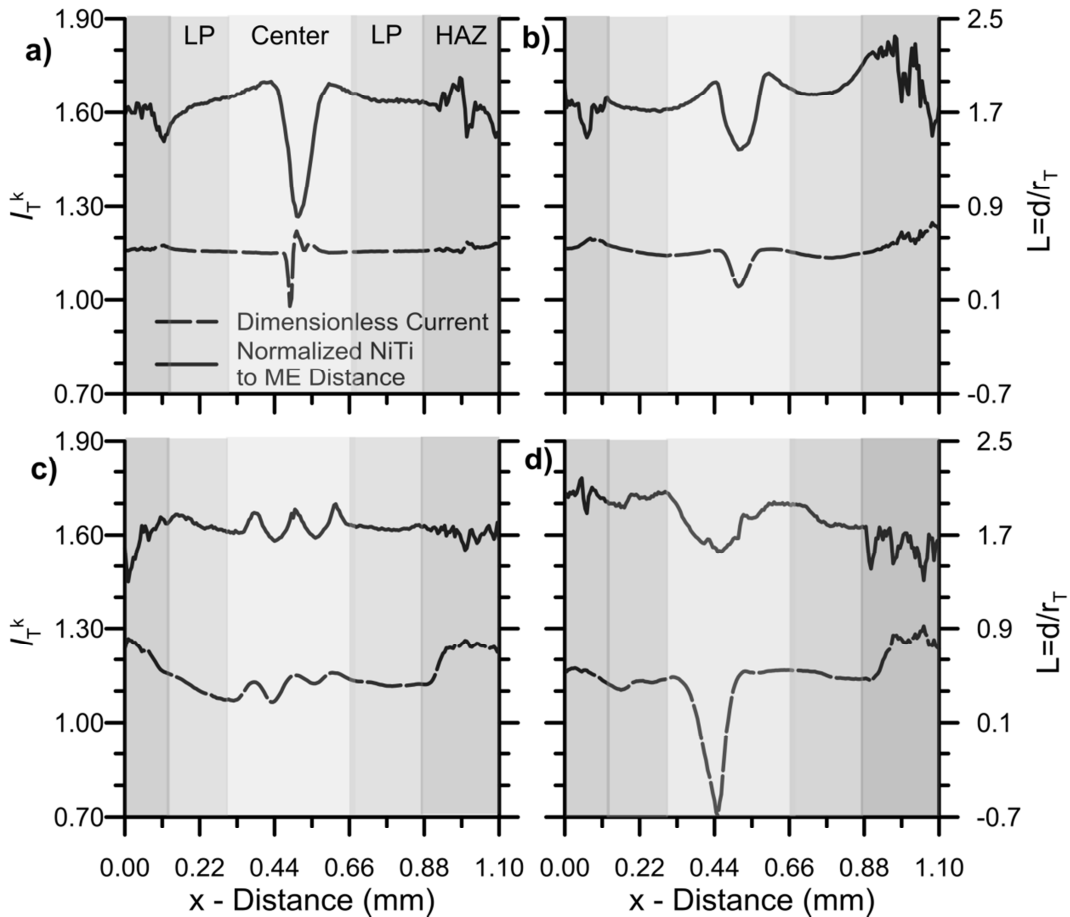


**Figure 4.3:** Line scans of dimensionless ME current and ME-NiTi distance across the center of a) 1LP, b) 3LP, c) 4LP and d) 5LP corresponding to dashed lines in Figure 4.1.

### 4.1.3 Feedback mode approach curves

Figure 4.4 shows a series of SECM feedback mode approach curves obtained for a 5LP NiTi sample. These measurements avoid the ambiguities introduced by topography and confirm that the variations in current observed in the images in Figure 4.1b are primarily due to variations in reactivity. The locations chosen span from the retained CE region, through the HAZ region and into the re-melted LP surface regions. Superimposed on these experimental curves are simulated approach curves for various values of the effective heterogeneous first-order rate constant  $k_{\text{eff}}$  [94]. The top and bottom dashed lines in Figure 4.4 represent theoretical curves for diffusion-controlled reaction at the sample (“positive feedback”) and hindered diffusion (no reaction at the sample, “negative feedback”), respectively. Open symbols are experimental data and solid lines are theoretical fits to the analytical approximation by Cornut and Lefrou [94].

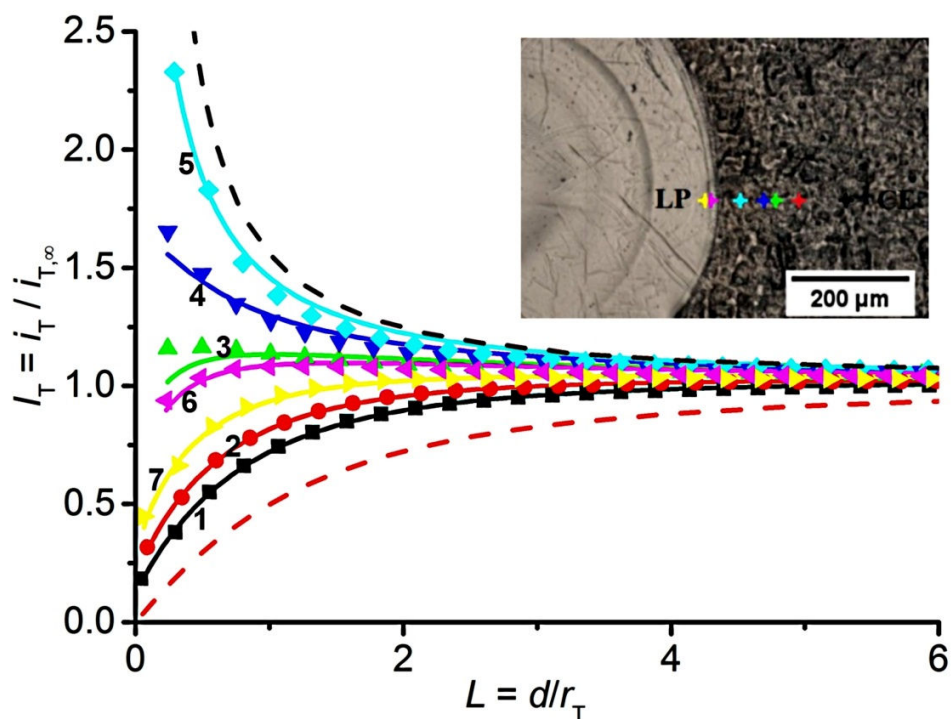


**Figure 4.4: Normalized SECM feedback approach curves measured for 5LP. Symbol lines are experimental approach curves, solid lines are the theoretical curves for finite electron transfer kinetics, while dashed lines are the theoretical curves for a totally conducting sample (upper curve) and for a totally insulating sample (bottom curve), respectively. Inset shows the area from which the SECM feedback approach curves were recorded, starting in the CE region, transitioning through the HAZ into the LP surface region. (SECM analysis courtesy of Dr. Ushula Tefashe, McGill University)**

The approach curves in Figure 4.4 show a transition from slightly negative feedback (curves 1, 2 and 7) on the retained CE/re-melted region to finite kinetic regime (curves 3, 4, and 6) and strong positive feedback (curve 5) in the HAZ regions. Generally, the experimental and simulated curves match well allowing values of  $k_{\text{eff}}$  to be determined for these regions. The  $k_{\text{eff}}$  values determined from the approach curves are listed in Table 1. These values confirm that the reactivity of different regions varies considerably. The  $k_{\text{eff}}$  values range from  $0.5 \times 10^{-3} \text{ cm s}^{-1}$  to  $34.2 \times 10^{-3} \text{ cm s}^{-1}$ , a difference of almost a factor of  $\sim 70$ . However, several points are worth discussing. (i) Smooth experimental curves and good fits to analytical approximation are generally obtained in the case of slightly negative feedback (approach curves 1, 2 and 7). This is consistent with the less reactive regions being associated with grains close in composition. (ii) For approach curves associated with intermediate values of  $k_{\text{eff}}$  (approach curves 3, 4, and 6), the flattening of the experimental approach curves as the ME tip comes close to the substrate surface may be due to contact between the substrate and the glass sheath of the tip [119-121]. (iii) The approach curve yielding the highest value of  $k_{\text{eff}}$  appears to develop in stages as the surface is approached. Since the reactive locations are associated with the highly faceted surface sites, this suggests that variations in reactivity associated with these surface ridges or variations in local chemistry may exist due to the close approach of the tip (*vide infra*). This result correlates with the observations of Chan et al. [21] and Pequegnat et al. [22] of a region with decreased corrosion resistance adjacent to each laser spot following the pulsed laser processing of NiTi alloys.

**Table 1: Effective heterogeneous first-order rate constant  $k_{\text{eff}}$  values determined from approach curves. (Analysis by of Dr. Ushula Tefashe, McGill University)**

Region	Approach Curve #	$k_{\text{eff}}$ ( $10^{-3} \text{ cm s}^{-1}$ )
Retained CE	1	0.5
	2	0.83
HAZ	3	4.2
	4	10.1
	5	34.2
	6	3.3
Re-melted	7	1.6

#### 4.1.4 Crystallinity of Surface Oxide

The SECM mapping of this conducting annular region around the spot (Figure 4.1a) was used to direct the Raman analysis and determine structural differences that exist in the oxides present in the HAZ, CE and LP regions. The Raman spectra for 1LP and 5LP are shown in Figure 4.5. For both samples peaks were observed at  $150 - 250 \text{ cm}^{-1}$  in the CE region, which correlates to Ti oxides. The 1LP sample had only one distinct HAZ region where partial crystallinity was observed. The broadness of the peaks suggests a thin oxide with very low amounts of crystallinity [89]. Due to the broadness of the peaks, the exact species present could not be verified, but the peak present on the HAZ of the 1P sample correspond closely with the anatase and rutile forms of  $\text{TiO}_2$ , which agrees with previous findings [89,122].

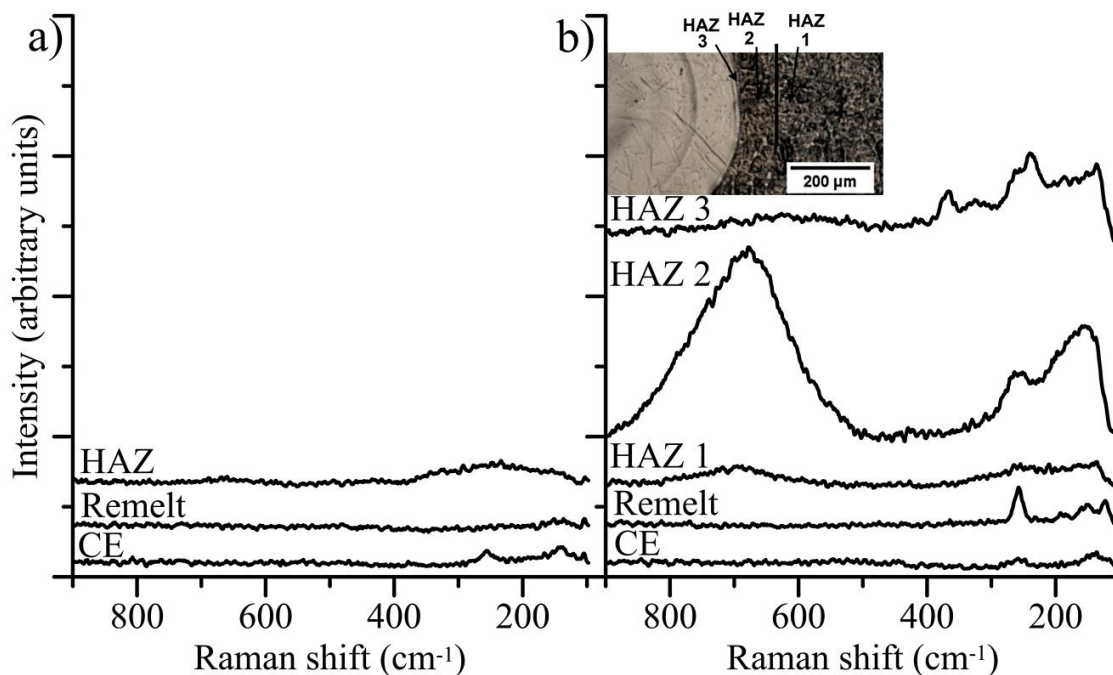


**Figure 4.5: Raman spectra for a) 1LP and b) 5LP with a resolution of  $\leq 1 \text{ cm}^{-1}$ . Inset shows the area from which the Raman spectra were taken, indicating the different HAZ regions observed in the 5LP sample.**

The Raman spectrum of the outer HAZ region of the 5LP sample, labelled HAZ 1 in Figure 4.5b, is similar to the HAZ region observed in the 1LP sample. The inner HAZ region, labelled HAZ 3 in Figure 4.5b, displays significantly sharper peaks, suggesting an increase in crystallinity and/or oxide thickness. The peaks observed in the HAZ 3 tend to correspond more closely to  $\text{NiTiO}_3$  [122], but without the presence of a peak above  $700 \text{ cm}^{-1}$ . This may be an

indicator that some Ni or Ni oxides may have been entrapped in the HAZ region after repeated pulsing. This result correlates well with the SECM maps of Figure 4.1b, which show increased reactivity on the right side of the laser spot corresponding to Ni plume deposits. The region labelled HAZ 2 appears to be a transition from the outer HAZ region to the inner HAZ region, with a significant peak around  $700\text{ cm}^{-1}$  that suggests the presence of Ni oxides. The spread of the crystalline structure and the extent to which it crystallizes seems to increase with the number of pulses. This is reasonable since more energy transferred into the sample should enable the oxide crystals to grow bigger and further.

The presence of these semi-crystalline regions surrounding the pulsed region is significant in two ways. Firstly, these crystal structures are known to provide a pathway for oxygen to reach the bulk NiTi material below the protective oxide and for Ni to reach the outer surface [89]. This agrees with the SECM findings that showed increased conductivity in the HAZ region. It is well known that an amorphous oxide layer is more robust than a crystalline oxide layer [29, 65] since it lacks these regular and ordered diffusion pathways. Additionally, these semi-crystalline regions create non-homogeneity across the surface. It is also well known that a uniform, homogeneous surface oxide is more stable than a heterogeneous surface oxide layer [65]. Potentiodynamic cyclic polarization tests were performed to determine the effect of this heterogeneity on the stability of the surface oxide.

#### **4.1.5 Corrosion Resistance**

Representative cyclic polarization curves for CE, 1LP, and 5LP are shown in Figure 4.6. After 1LP, the breakdown potential decreases slightly from  $1.170 \pm 0.025\text{ V}$  to  $1.121 \pm 0.021\text{ V}$ ; as well, the repassivation potential drops marginally from  $1.027 \pm 0.018$  to  $0.974 \pm 0.023\text{ V}$ . These slight decreases in the potential may be due to the onset of inhomogeneities in the surface oxide caused by partial crystallinity of the HAZ region.

After 5LP, the breakdown potential is significantly reduced to  $0.477 \pm 0.194\text{ V}$ . Also, the samples are unable to repassivate above the corrosion potential. Breakdown of the 5LP oxide is found to occur along the outer edge of the sample adjacent to the area limiting gasket, in the form of crevice corrosion observed optically (Figure 4.6c). NiTi SMAs are known to be susceptible to crevice corrosion [123]. The decrease in roughness of the laser spot in the centre

of the sample most likely contributes to a build-up of corrosion products around the outer edge, where the area limiting gasket forms an artificial crevice. This likely leads to the crevice corrosion breakdown since this form of corrosion is not observed in the CE samples.

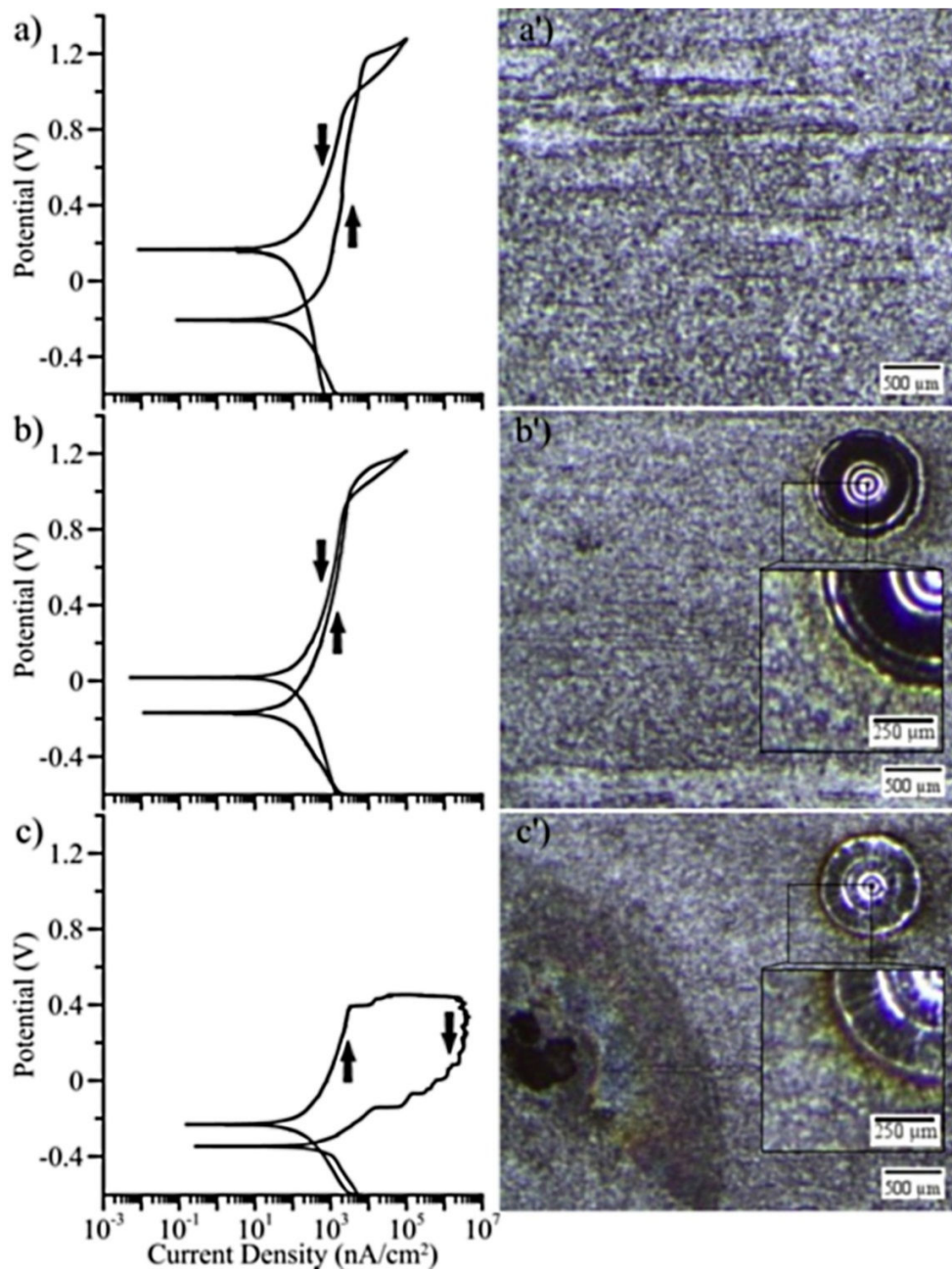


**Figure 4.6: Representative potentiodynamic cyclic polarization curves for a) CE, b) 1LP and c) 5LP with corresponding optical images of resulting corrosion.**

Although the breaking point is the artificial crevice formed around the outer edge of the sample, an increase in the amount of corrosion in the HAZ of the 5LP sample is observed

optically compared to the HAZ of the 1LP sample. A dark brown ring forms around the 5LP spots during cyclic polarization testing (Figure 4.6c') with the darkest regions being closest to the re-melt region (*i.e.* HAZ region) where the highest crystallinity is observed. Only a slight discoloration is observed around the 1LP after cyclic polarization testing (Figure 4.6b'). This suggests that the HAZ of the 1LP sample has a marginally higher corrosion rate than the re-melt region or retained base material (although not detrimentally so), but a much slower oxidation rate than the HAZ of the 5LP sample. Thus it appears that the rate of oxidation is locally higher in the HAZ region around the 5LP due to an increase in crystallinity, leading to poor corrosion performance in the HAZ compared to the re-melt region and the retained base material, as observed in past studies [21, 22].

## 4.2 Effects of an Array of Pulsed Laser Spots

In order to verify that crevice corrosion occurs primarily due to a combination of a too small HAZ region and the surface topography, new test samples were made. For the remainder of this study, the samples are processed with overlapping spots in an array pattern with a large enough area so that the CE surface was no longer significantly larger than the HAZ surface. A schematic representing the surface areas of the CE, HAZ, and LP regions is shown in Figure 4.7.

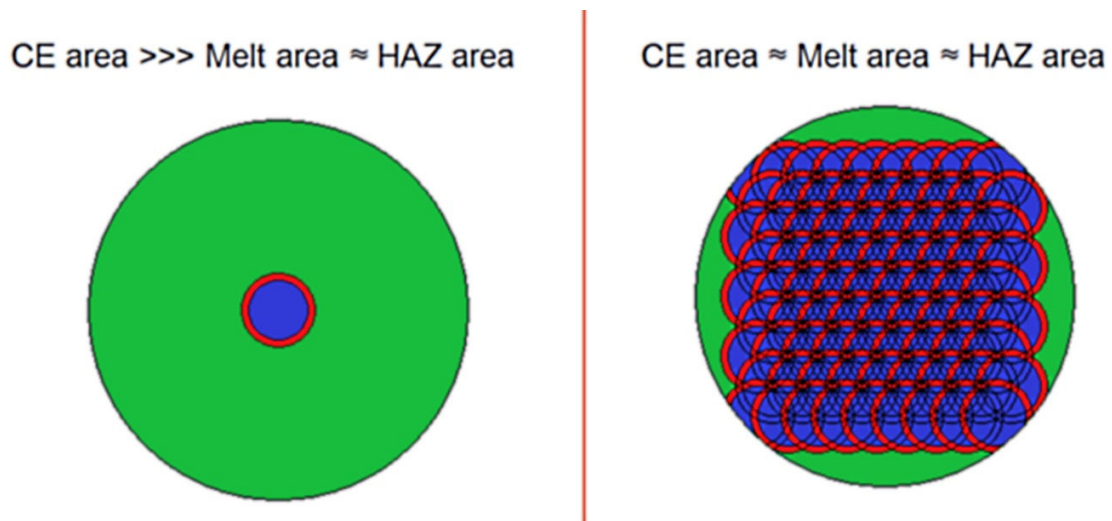


**Figure 4.7: Schematic showing relative surface areas exposed during cyclic polarization testing. Green is the CE surface area, blue is the LP re-melt surface area, and red is the HAZ surface area. Areas in schematic are approximations.**

## 4.2.1 Topography of Overlapping Spots

The 3D topographical profiles of the overlapping spots are shown in Figure 4.8 compared with a typical CE surface. The laser spots appear to be smoother than the CE surfaces, but the overall  $R_a$  values are slightly higher after LP. The  $R_a$  are calculated to be  $2.02 \mu\text{m}$  (CE),  $2.30 \mu\text{m}$  (1LPO) and  $2.39 \mu\text{m}$  (5LPO). The reason for the increase in the  $R_a$  value may be due to much lower regions that are located at the center of each spot (shown in dark blue), and the resulting scale pattern that forms due to the overlap of laser spots. Also, roughened rings are observed around each spot, which may contribute to the slight increase in the  $R_a$  value. Surface morphology was characterized prior to any corrosion analysis to determine if topographic features would play a role in early corrosion breakdown. With similar  $R_a$  values, topography would not be expected to be a major concern. The crucial factor should be the oxide crystallinity.

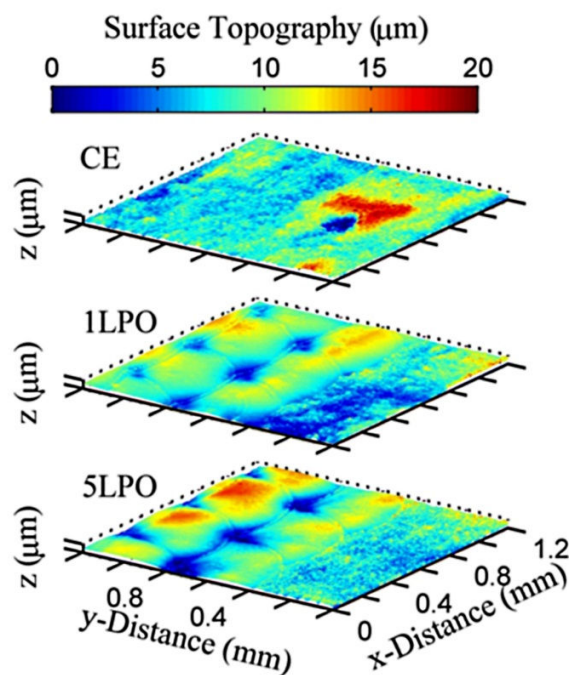


**Figure 4.8: Surface topography maps of CE, 1LPO and 5LPO samples.**

## 4.2.2 Crystallinity of Surface Oxides

The Raman spectra for 1LPO and 5LPO are shown in Figure 4.9. Both samples have two HAZ regions that are analyzed. The Raman spectra of outer HAZ regions of the both 1LPO and

5LPO samples, labelled HAZ 1 in Figure 4.9, are similar to the HAZ region observed in the 1LP sample and the HAZ1 region of the 5LP sample. The inner HAZ region, labelled HAZ 2 in Figure 4.9, displays no significant crystallinity for the 1LPO sample. However, in the 5LPO sample the HAZ2 region shows a sharpening of the peaks, suggesting an increase in crystallinity and/or oxide thickness. A peak also appears close to  $700\text{ cm}^{-1}$  corresponding more closely to  $\text{NiTiO}_3$  [122]. This may be an indicator that some Ni or Ni oxides may have been entrapped in the inner HAZ region after repeated pulsing. Potentiodynamic cyclic polarization tests are conducted to determine the effect of these differing amounts of crystallinity in the inner HAZ on the stability of the surface oxide.

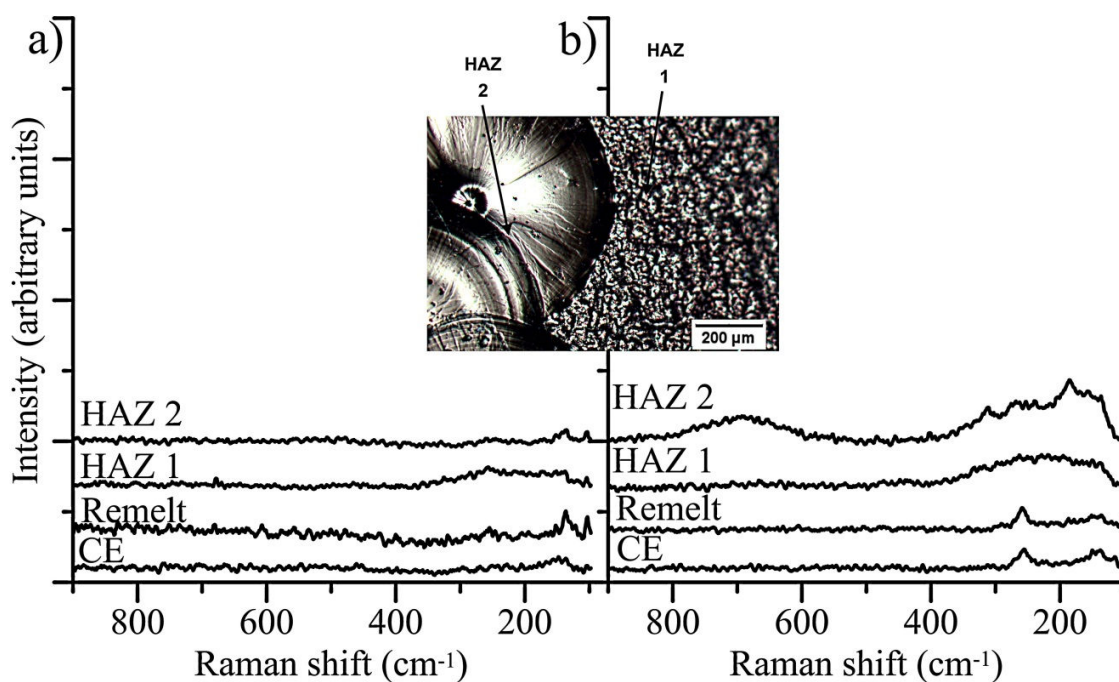


**Figure 4.9: Raman spectra for a) 1LPO and b) 5LPO with a resolution of  $\leq 1\text{ cm}^{-1}$ . Inset shows the area from which the Raman spectra were taken, indicating the different HAZ regions observed in both samples.**

### 4.2.3 Corrosion Resistance

Representative cyclic polarization curves for CE, 1LPO, and 5LPO are shown in Figure 4.10. After 1LPO and 5LPO, the breakdown potential is again reduced to  $0.581 \pm 153\text{ V}$  and  $0.535 \pm 0.71\text{ V}$ , respectively, similar to the 5LP samples. However, unlike the 5LP samples, the 1LPO samples are able to repassivate half of the time and the 5LPO samples are able to repassivate

every time; although the repassivation potential for 1LPO is  $-0.066 \pm 0.052$  V and  $-0.035 \pm 0.057$  V for 5LPO. This does suggest that when corrosion takes place in the HAZ it is somewhat easier to repassivate than when the corrosion takes place at the artificial crevice created by the limiting gasket.

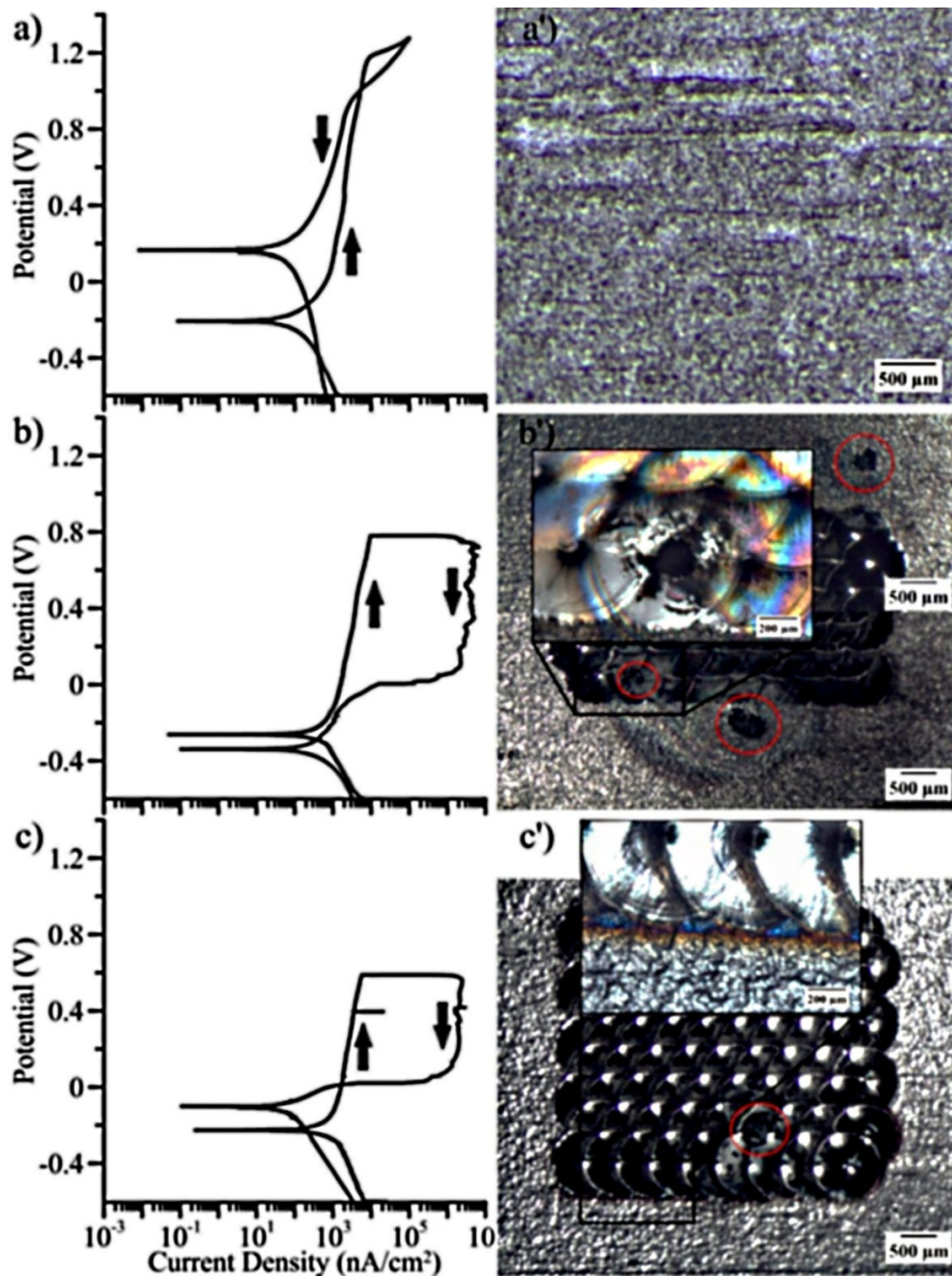


**Figure 4.10: Representative potentiodynamic cyclic polarization curves for a) CE, b) 1LPO and c) 5LPO with corresponding optical images.**

The corrosion initiation sites for the 1LPO samples are randomly distributed in the HAZ region or along the outer edge as crevice corrosion, as shown in Figure 4.10b'. The location of the corrosion sites corresponds with the samples ability to repassivate, as mentioned earlier. These findings also correlate well with the Raman spectroscopy which showed a low degree of crystallinity in the HAZ region, making it equally as unstable as the artificial crevice. The surface area of the HAZ is larger for 1LPO than 1LP, giving it an equal chance to corrode compared with the artificial crevice region. This also implies that the determining factor for corrosion initiation is surface roughness, not crystallinity, due to the low degree of crystallinity of these samples.

The 5LPO samples only corrode in the HAZ region and never corrode around the outer edge, as shown in Figure 4.10c'. This reaffirms the hypothesis that the HAZ region in the single spots samples is too small to be effective corrosion test samples. It also verifies that the instability of the oxide in the HAZ region increases with the number of pulses, since the instability of the HAZ becomes more dominant and supersedes corrosion in the artificial crevice region.

### **4.3 Chapter Summary**

This chapter demonstrated how the energy input during laser processing can affect the corrosion performance of NiTi SMAs. Furthermore, the oxide stability was investigated by SECM, Raman, and cyclic polarization testing. The amount of energy input determines the amount of crystallinity in the HAZ, which explains previous discrepancies in corrosion performance after laser processing. For fewer numbers of pulses (i.e. lower energy inputs) and thus low degrees of crystallinity, the determining factor for corrosion appears to be surface texture. For increased number of pulses (i.e. higher energy inputs), the determining factor for corrosion is the crystallinity in the HAZ region. Further testing will be done to improve the corrosion performance to that achievable prior to laser processing.

## Chapter 5: Post-Process Surface Modifications

Due to the nature of the oxide evolution, appropriate post-process surface treatments were chosen to restore the corrosion performance. Since the root causes of failure were topography and oxide crystallinity, heat treatments were ruled out as a possibility. While some improvement may be gained by thickening the oxide, this would only exacerbate the issue of crystallinity and very little overall improvement would be gained, as has already been shown in a previous study by Chan et al. [20]. The aim of this current study is to determine a better solution. Boiling water, hydrogen peroxide, and autoclave methods are all promising treatments, but they cannot remove crystallinity of the oxide and must be preceded by another surface treatment. The electropolishing method is not well understood and was not attempted in this study, but it may be a viable solution. The methods of mechanical polishing and chemical etching were tested for this study.

### 5.1 Mechanical Polishing

The MP procedure was chosen because it physically removes the outer surface, eliminating the topography effects and the detrimental crystalline oxide and builds a new oxide on a uniformly flat surface. This has already been shown to be effective at restoring the stability of a sample that has been completely laser processed [22]. However, since the oxide formed during this process retains the phases present in the bulk material (see Section 2.2.3 Mechanical Polishing) the question arises as to whether the surface oxide will be uniform enough when two different bulk compositions are present. Since laser processing is known to alter the composition of NiTi SMAs, a sample containing a LP region and a base material region would have two slightly different bulk compositions, which could affect the compositions of the oxides formed in each region.

#### 5.1.1 Topography of Mechanically Polished Surface

The 3D topographical profile of the LPMP surface is shown in Figure 5.1 compared with a typical CE surface. After polishing, the surface is much smoother with a  $R_a$  value of  $0.71 \mu\text{m}$ . Topographical features should not play any role in early corrosion failures; only crystallinity

and possible Ni compositions should be a factor in the corrosion behaviour of the LPMP samples.

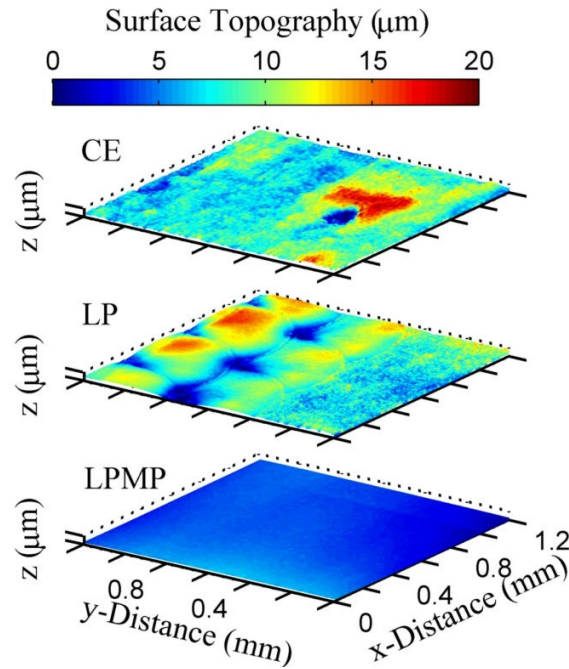


**Figure 5.1: Surface topography maps of CE, LP and LPMP samples.**

### **5.1.2 Crystallinity of Oxide formed by Mechanical Polishing**

The Raman spectrum for the LPMP surface is shown in Figure 5.2 compared to the untreated HAZ spectrum and the original CE spectrum. After MP, the crystallinity of the surface oxide is comparable to that of the original CE surface. Also, no evidence of any crystalline Ni appears in the Raman spectrum of the LPMP surface. Additional data from several scans taken across the LPMP surface are provided in Appendix II: Experimental Data for Raman Tests. The MP surface treatment is an effective means of removing the crystallinity in the HAZ region. The only uncertainty is possible oxide layer inhomogeneity across the surface due to the different bulk compositions.

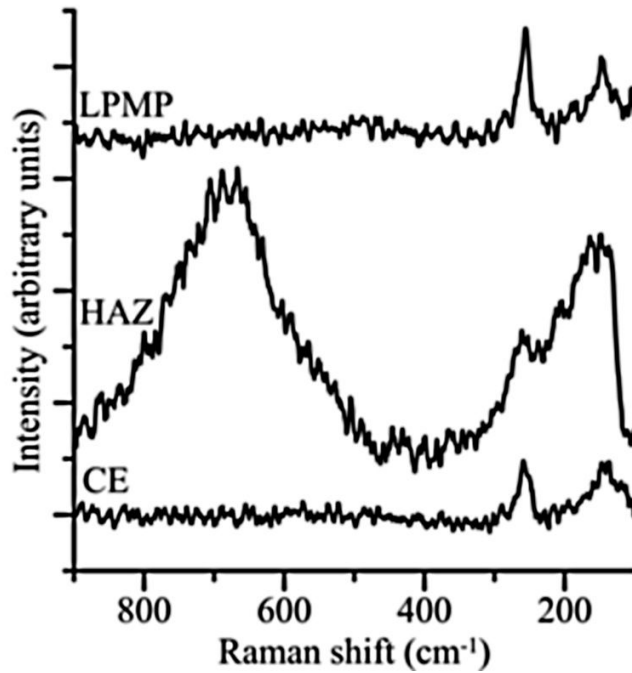


**Figure 5.2: Representative Raman spectra for the CE surface, untreated HAZ region, and the LPMP surface.**

### 5.1.3 Corrosion Resistance of Mechanically Polished Surface

Representative cyclic polarization curves for CE, 5LPO, and LPMP are shown in Figure 5.3. After MP, the breakdown potential and repassivation potential are restored to  $1.137 \pm 0.042$  V and  $1.026 \pm 0.007$  V, respectively, similar to the  $1.170 \pm 0.025$  V breakdown potential and  $1.027 \pm 0.018$  V repassivation potential of the CE surface. However, the corrosion potential of the LPMP surface decreases significantly to  $-0.461 \pm 0.046$  V compared to  $-0.194 \pm 0.032$  V of the CE surfaces. The drastic change in the corrosion potential is most likely due to the fact that the LPMP surface oxide layer contains significantly more elemental Ni than either the CE or 5LPO samples.

Something important to note is that the surface oxide thickness does not play a significant role in determining the breakdown potential. A previous study by Pequegnat et al. [22] showed that the oxide thickness of the mechanically polished surface is about half the thickness of the chemically etched surface. However, it has been shown that the oxide layer of a MP sample continues to develop *in situ* [81], preventing earlier failure due to a thinner oxide. It is also important to note that the LPMP polished surface does not undergo any preferential corrosion

due to the differences in the bulk compositions. This result is not completely unexpected, as Ruhlig et al. [118] found no significant difference in corrosion performance across the surface of a polished cross-section of a NiTi weld.

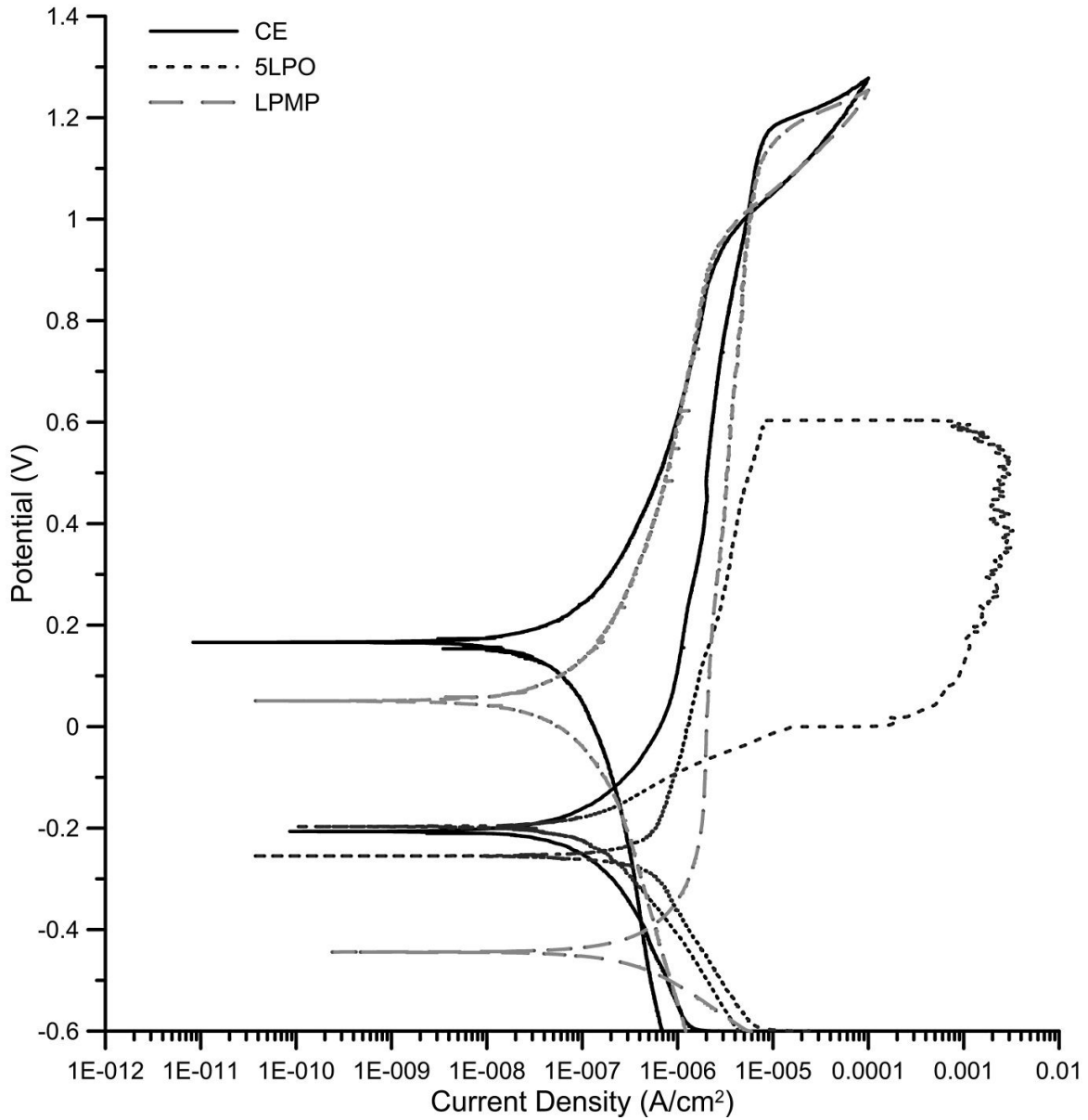


**Figure 5.3: Representative potentiodynamic cyclic polarization curves for CE, 5LPO and LPMP**

## 5.2 Chemical Etching

The CET method was chosen as a post-process treatment because it chemically breaks down the crystallinity in the oxide and removes excess Ni from the surface. Also, the interaction of the etchants with the surface should roughen up the smooth laser spots and decrease the topographic disparity between the retained original CE surface and the LP surface. Since the oxide thickness after laser processing is not excessive, a quick 30 second etching time can avoid over-etching the retained original CE regions.

### 5.2.1 Topography of Chemically Etched Surface

The 3D topographical profile of the LPCE surface is shown in Figure 5.4 compared with a typical CE surface. After etching, the surface is marginally rougher than the original 5LPO surface, with a  $R_a$  value of 2.69  $\mu\text{m}$  compared to 2.39  $\mu\text{m}$ . This change is not significant, but visual observations show a significant decrease in the reflectivity of the LP region after CET (Figure 5.5). Also, the laser spots are no longer well defined features in the topography, although there is still some disparity in surface texture between the LP region and the CE region is still observed. However, the roughness is closer to that of the CE surface and the topography is more uniform across the surface; this should not be as big a determining factor for the corrosion performance as previously seen with the 1LPO samples. The most critical aspect is whether or not the crystallinity has been removed from the HAZ region.

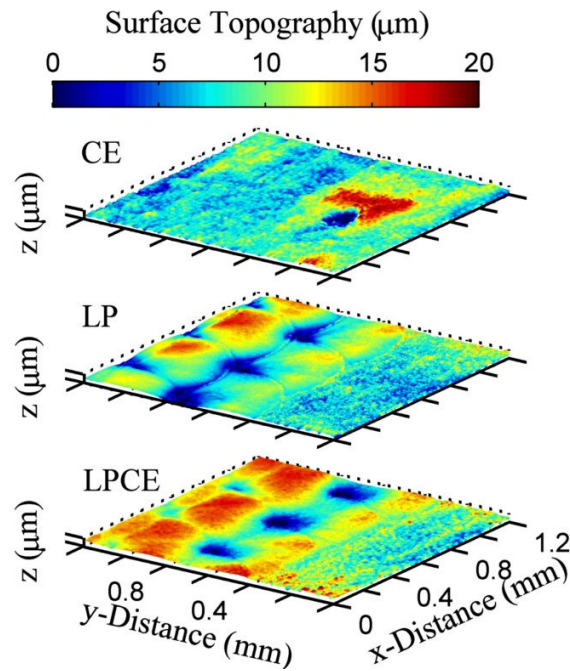


Figure 5.4: Surface topography maps of CE, LP and LPCE samples.

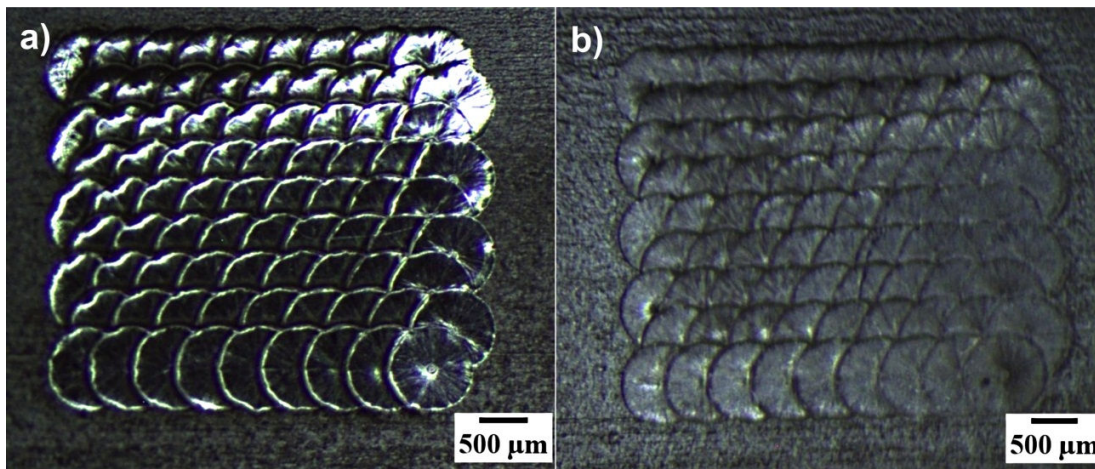
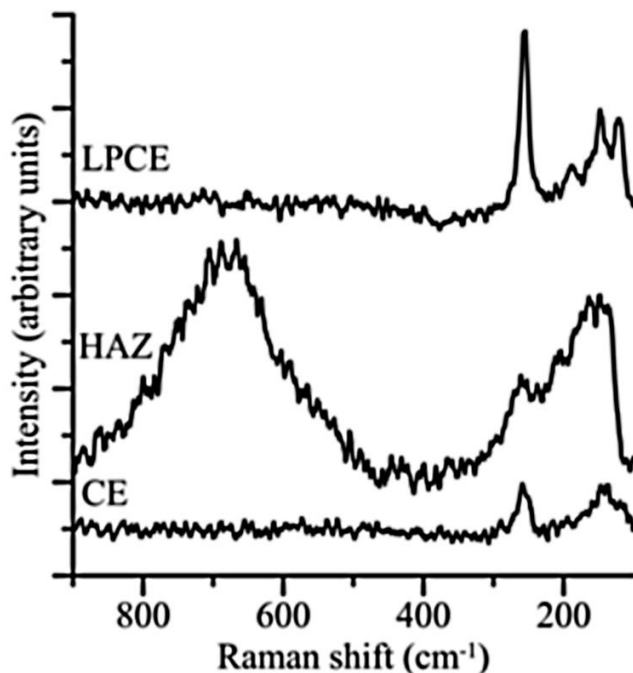


Figure 5.5: Optical image of a) 5LPO sample and b) LPCE sample showing differences in reflectivity after CET.

### 5.2.2 Crystallinity of Oxide formed by Chemical Etching

The Raman spectrum for the LPCE surface is shown in Figure 5.6 compared to the untreated HAZ spectrum and the original CE spectrum. After the CE treatment, no evidence of any crystalline Ni appears in the Raman spectrum. Data from several scans taken across the LPCE surface are provided in Appendix II: Experimental Data for Raman Tests. However, the LPCE surface showed slightly increased crystallinity of Ti compared to that of the original CE

surface. This may be an indication that the surface is close to being over etched. It is important to verify that this degree of crystallinity is not detrimental to the overall stability of the oxide surface.



**Figure 5.6: Representative Raman spectra of the CE surface, the untreated HAZ region, and the LPCE surface.**

### **5.2.3 Corrosion Resistance of Chemically Etched Surface**

Representative cyclic polarization curves for CE, 5LPO, and LPCE are shown in Figure 5.7. After CE, the breakdown potential and repassivation potential improve to  $1.092 \pm 0.007$  V and  $0.974 \pm 0.017$  V, respectively. This is slightly lower than the  $1.170 \pm 0.025$  V breakdown potential and  $1.027 \pm 0.018$  V repassivation potential of the original CE surface. The difference in potentials may be due to the fact that the post-process CET is significantly shorter in duration than the original CET in order to avoid over etching the original CE surface. Another factor could be that surface roughness is increased on the LPCE samples. Optimisation of the post-process CET stills need to be doned.

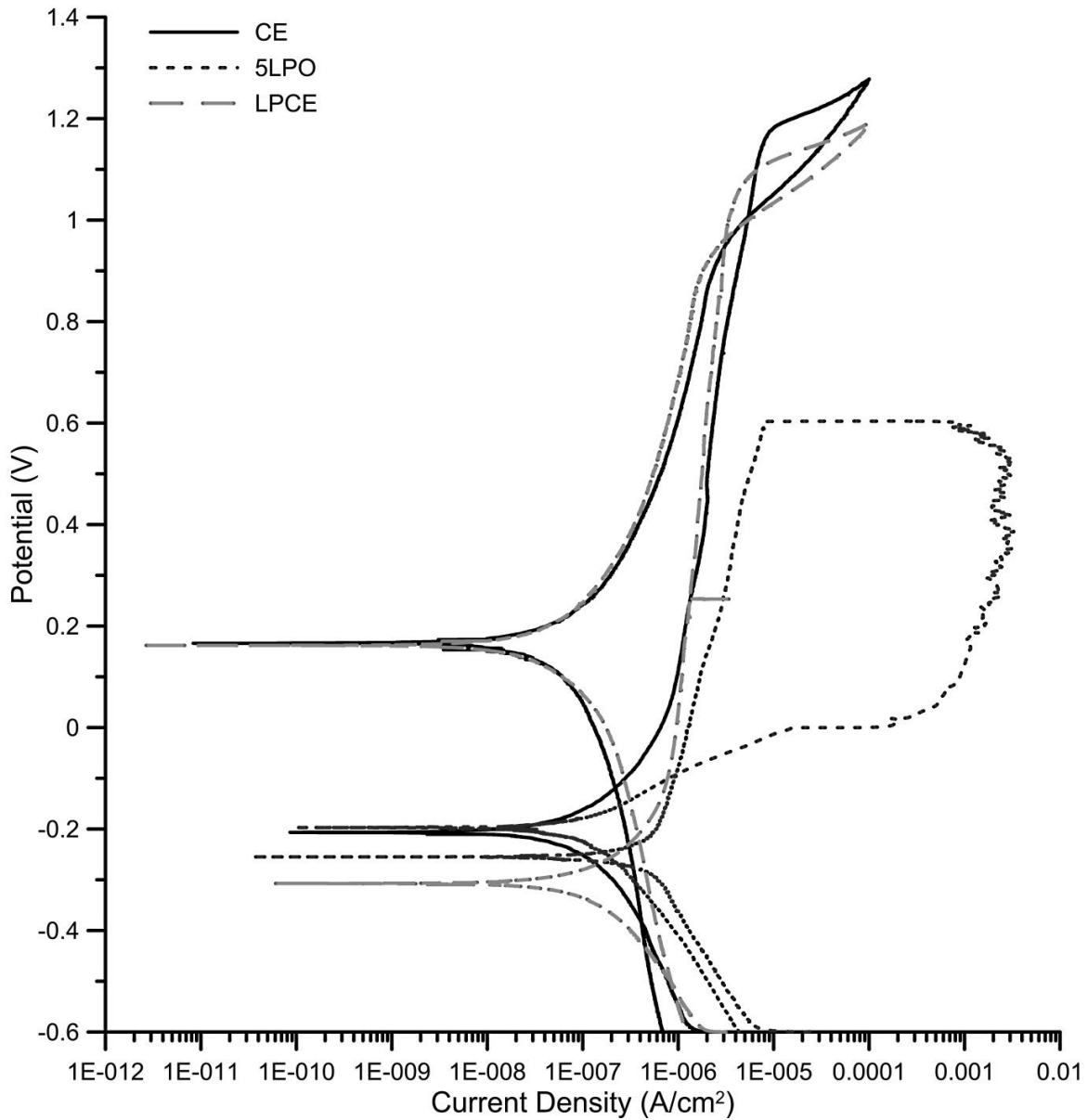


**Figure 5.7: Representative potentiodynamic cyclic polarization curves for CE, 5LPO and LPCE**

## 5.2 Boiling Water

Since  $E_{\text{corr}}$  is significantly lower for the LPMP samples and  $E_{\text{break}}$  is slightly lower than desired for the LPCE samples, an additional post-process treatment is used to further improve the corrosion performance of the surface oxides. As mentioned earlier, the BW method cannot be applied directly after LP. However, once the crystalline oxide has been removed, BW can be used to further enhance the surface oxide (see Section 2.2.5 Boiling Water). The BW was

applied to both LPMP samples and LPCE samples to determine how it would improve the oxide properties.

### 5.3.1 Topography of Surfaces after Boiling Water Treatment

The 3D topographical profiles of the LPMPBW and LPCEBW surfaces are shown in Figure 5.8 compared with the surfaces of their untreated counterparts. After BW, the Ra values decrease slightly from 0.71 to 0.67 and from 2.69 to 2.40 for the LPMPBW and LPCEBW samples, respectively. This agrees with previous studies that have observed a smoothing of the surface topography after the BW treatment [29, 93]. This added benefit of the BW treatment should only enhance the corrosion performance, as long as the new oxide grown during the process is still amorphous.

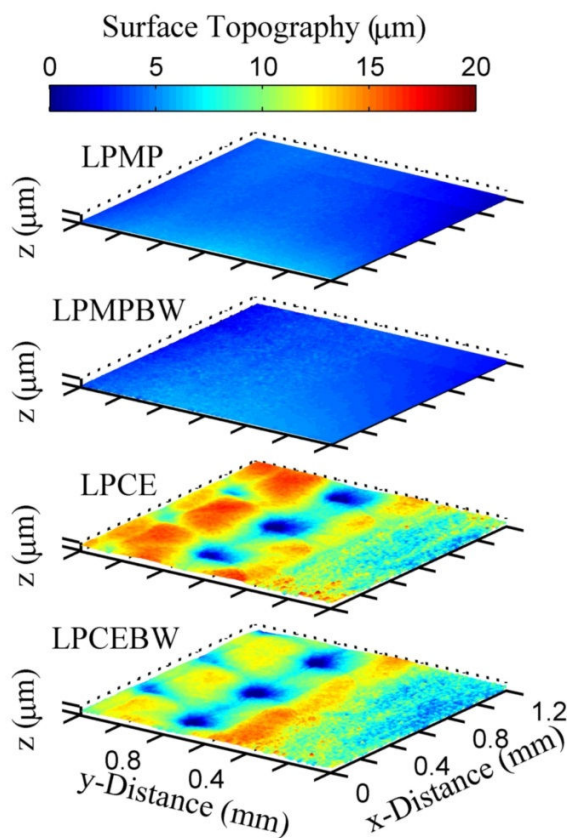


**Figure 5.8: Surface topography maps of LPMP, LPMPBW, LPCE and LPCEBW samples.**

### 5.3.2 Crystallinity of Oxide formed by Boiling Water

The Raman spectra for LPMPBW and LPCEBW are shown in Figure 5.9 compared with their untreated counterparts. After the BW treatment, no significant change in the oxide crystallinity is observed. This is expected since any oxide formed during the BW treatment is typically amorphous. Additional data from several scans taken across the LPCE surface are provided in Appendix II: Experimental Data for Raman Tests. From the Raman results it is unclear if any improvement to the surface has been made, but it is reasonable to assume that no negative effects have been incurred.

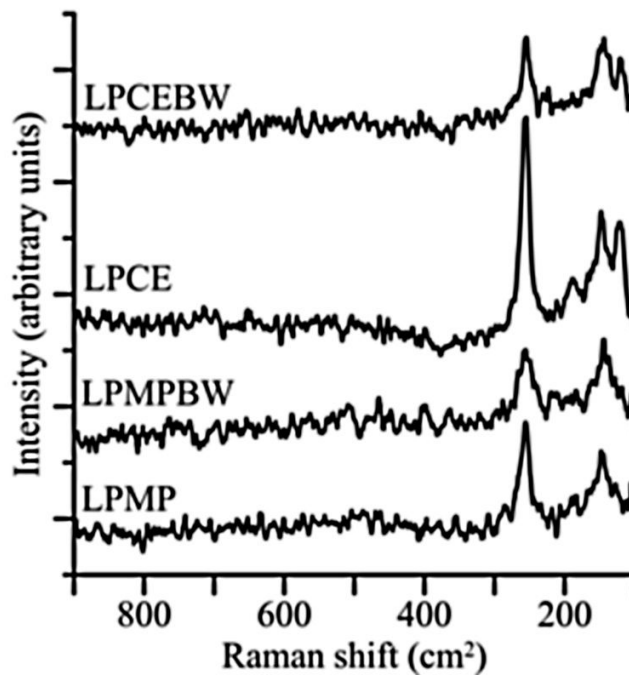


**Figure 5.9: Representative Raman spectra for the LPMP surface, the LPMPBW surface, the LPCE surface and the LPCEBW surface.**

### 5.3.3 Corrosion Resistance of Boiling Water Treated Surfaces

Representative cyclic polarization curves for CE, LPMP, and LPMPBW are shown in Figure 5.10. After BW treatment, the breakdown potential and repassivation potential showed little change. However, the corrosion potential of the LPMPBW surface rises to  $-0.314 \pm 0.032$  V compared to  $-0.461 \pm 0.046$  V of the LPMP surfaces. This suggests that the BW treatment is able to remove some Ni from the surface oxide.

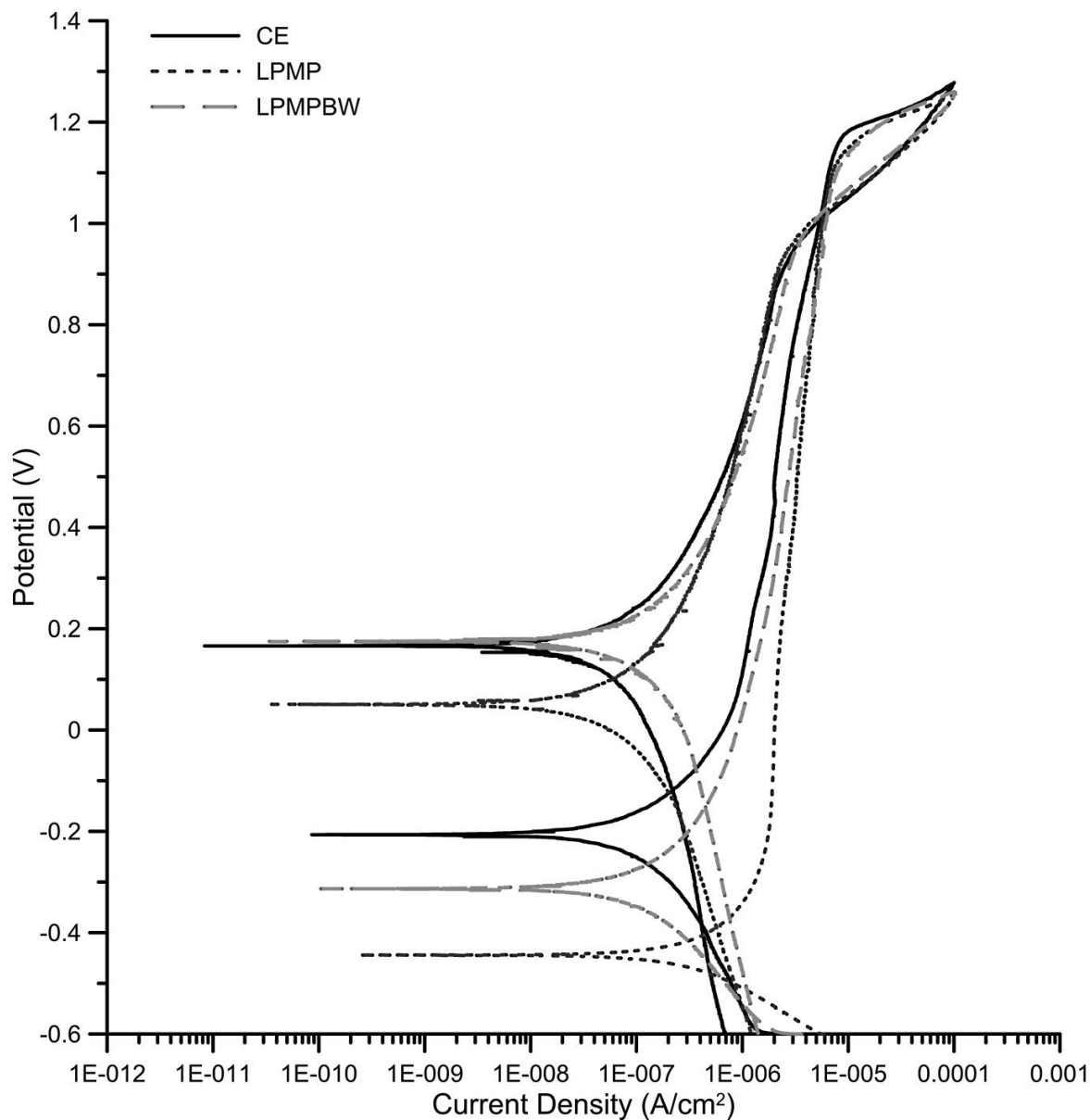


**Figure 5.10: Representative potentiodynamic cyclic polarization curves for CE, LPMP and LPMPBW**

Representative cyclic polarization curves for CE, LPCE and LPCEBW are shown in Figure 5.11. After BW treatment, the breakdown potential and repassivation potential again show little change. Once again, the corrosion potential of the LPCEBW surface increases to  $-0.211 \pm 0.006$  V compared to  $-0.319 \pm 0.027$  V of the LPCE surfaces. This confirms that the BW treatment is again able to remove some Ni from the surface oxide.

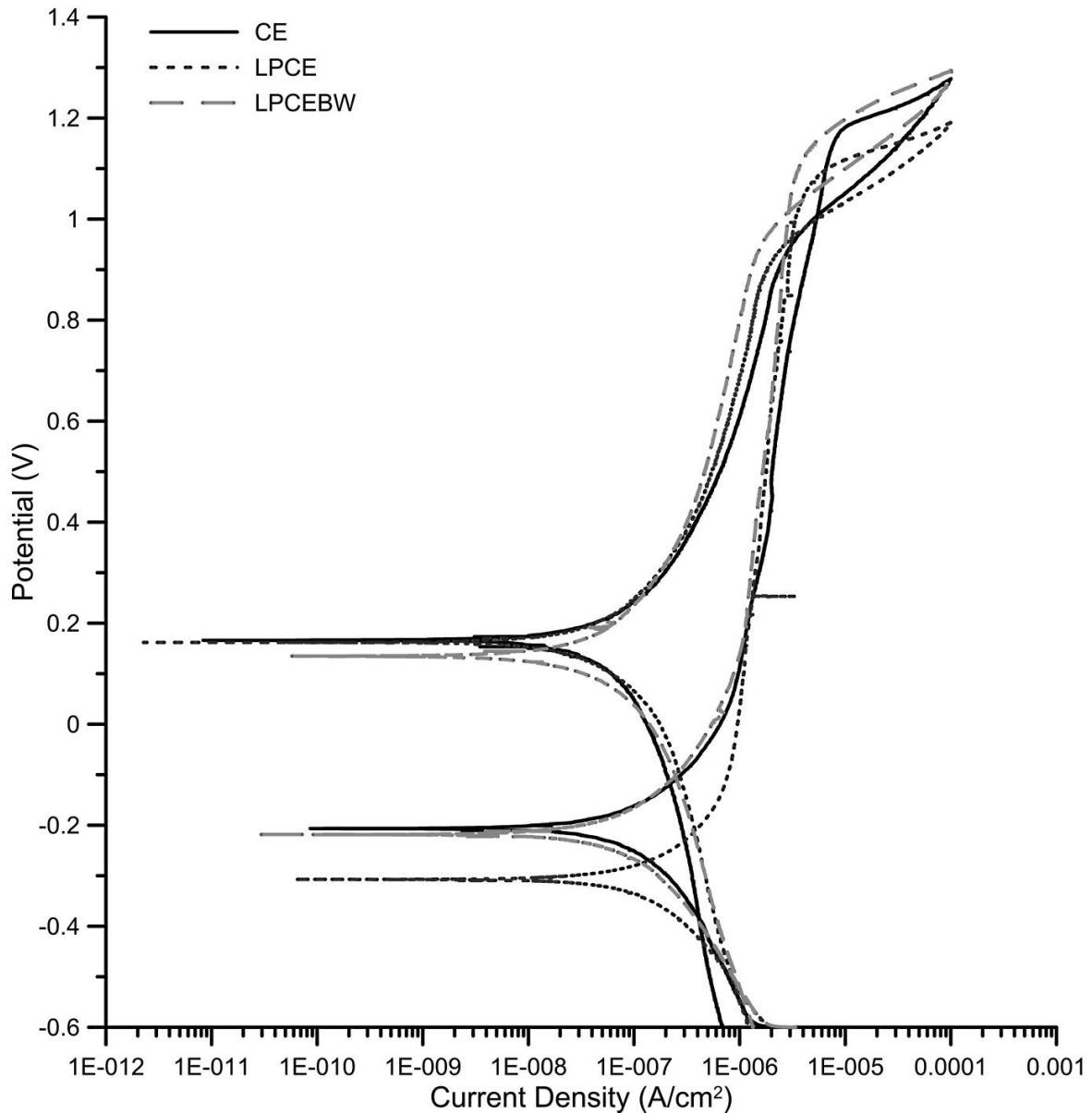


**Figure 5.11: Representative potentiodynamic cyclic polarization curves for CE, LPCE and LPCEBW**

### 5.3 Chapter Summary

This chapter demonstrated how the proper post-process surface treatments can remove the crystallinity that forms during laser processing. Furthermore, the oxide stability was investigated by Raman and cyclic polarization testing. After removal of the oxide crystallinity, the surface uniformity became the dominant factor in the oxide stability. The surfaces with uniform topographies (CE, LPMP, and LPMPBW) had slightly better breakdown potentials

than surfaces with mixed topography (LPCE, LPCEBW). Surfaces treated by the boiling water method had higher corrosion potentials than the untreated surfaces, suggesting that the amount of Ni present in the surface oxide may strongly affect the corrosion potential of the sample. Post-process surface treatments effectively restored the corrosion performance of laser processed NiTi SMA to pre-processed capabilities.

# Chapter 6: Conclusions

The purpose of this work was to better understand how the surface oxide evolves during laser processing to better improve laser-processed NiTi SMAs. Accordingly, the effect of laser pulsing (i.e. energy input) on the oxide structure and stability was investigated experimentally. Additionally, techniques were used to return the oxide to pre-processed standards. The major findings of this thesis are as follows:

## 6.1 Oxide Evolution

1. The SECM proved to be an effective non-destructive method for isolating the region of increased reactivity on the surface of laser-processed NiTi SMAs. Increased reactivity in the HAZ region corresponds well with that reported in previous studies.
2. The increased reactivity observed in the HAZ was determined to result from the increased crystallinity with possible contributions from Ni plume deposits following the heating/cooling cycles that occur during laser processing.
3. The effects of the HAZ on oxide stability were determined by the number of pulses used (*i.e.* the energy input during processing).
  - a. Corrosion performance of the lower energy input samples is dictated by the surface texture.
  - b. Higher energy inputs however had significant effects on the crystallinity in the HAZ region; with enough energy input, corrosion in the HAZ is preferred over crevice corrosion.

## 6.2 Post-process Modifications

1. Raman spectroscopy verified the removal of surface oxide crystallinity by both mechanical polishing and chemical etching of the surface of LP samples
2. After crystallinity, surface structure uniformity seems to be the dominant factor in determining breakdown potentials.
  - a. The surfaces with more uniform topographies (CE, LPMP, and LPMPBW) have slightly higher breakdown potentials.

- b. The surfaces with mixed topographies (LPCE and LPCEBW) exhibited slightly lower breakdown potentials.
3. The boiling water treatment effectively removed Ni from the surface oxide and increased the corrosion potential
4. The post-process surface treatments employed were effective at restoring the corrosion performance of laser-process NiTi SMA to pre-processed capabilities.

## **6.3 Recommendations for Future Work**

This study was a continuation of previous research and utilized the materials and test methods already in place. To gain a better understanding of the material and a more complete idea of the corrosion performance, additional work is required.

### **6.3.1 Alternative Sample Preparation**

An alternative process for sample preparation would be to use an argon-filled glove box and soot sucker during laser processing, Figure 6.1. The argon-filled glove box would reduce the amount of available oxygen during laser processing more effectively than does shielding gas. The soot-sucker would remove material that evolves from the surface before it can redeposit on the sample surface. This should effectively eliminate formation of the Ni plume deposits during laser processing. Preparation of samples by this method will allow for a better understanding as to how much Ni plume deposits affect the surface oxide formation during laser processing.

It would also be worthwhile to investigate the use of electropolishing as a post-process treatment for laser processing. Some success has been reported with electropolishing treatments [80]. It may offer a more suitable solution when dealing with complex geometries that may arise after laser processing. Another alternative surface treatment would be to use a low energy laser source (i.e. femtosecond laser) and remelt the entire surface. The lower energy input would prevent further crystal growth and would not alter the bulk composition. The remelting of the entire surface would create a more uniform surface texture across the retained base material and the laser processed region. What needs to be investigated is whether or not this process would be able to break up the oxide crystals already present in the HAZ

region, since LSM techniques have only been employed on surfaces that already had an amorphous oxide [15, 19].

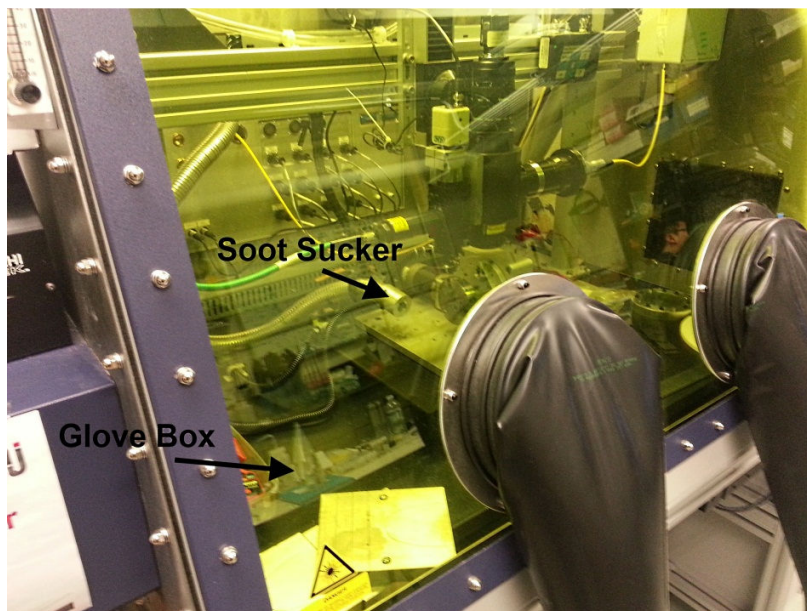


**Figure 6.1: Laser inside of glove box containing argon atmosphere and soot sucker.**

### **6.3.2 Improved Corrosion Test Procedure**

The cyclic polarization test set-up used for this study was a carry-over from previous studies that focused on the use on NiTi-based SMAs for dental applications. For general biomedical applications, a more aggressive solution such as Hanks' solution should be used. This would allow for a more accurate test of real-life applications.

Degassing with nitrogen and scanning at a relatively fast scan rate was done to adhere closely to the ASTM standard [103] and generate data that were comparable to data already available. Bubbling with air or, even better, oxygen would more accurately represent real life biomedical environs. A slower scan rate of 0.0167 or 0.01 mV/s would be more sensitive to pitting. It can be seen from the additional data provided in that there was some evidence of pitting and repassivation before the breakdown potential was reached for several different samples. A slower, long term corrosion study is crucial before the implementation of biomedical applications.

### 6.3.3 Additional Testing Required

In this study, Raman spectroscopy was used to determine the degree of crystallinity of the surface oxide. Due to the nature of the oxide (i.e. very thin, low crystallinity), Raman spectroscopy is not an ideal analysis method. Better characterization of the surface oxide should be done using glancing angle XRD or XPS analysis. These techniques will provide a better understanding of how the surface oxide is changing with different energy inputs.

This study focused on the top side of NiTi SMA sheets. However, the bottom surface should also be investigated for completeness. Even if the energy input is low enough that only partial penetration is achieved (Figure 6.2) the HAZ may reach the bottom surface and crystallize the surface oxide. Alternatively, the energy input may be high enough to melt metal throughout the bulk. The bottom surface would also melt and re-solidify with a crystalline HAZ ring. The bottom surface may also not benefit from the vaporization of Ni, since vaporization occurs only on the top. For these reasons, it is important to characterize the bottom surface of thin NiTi SMA sheets after laser processing.

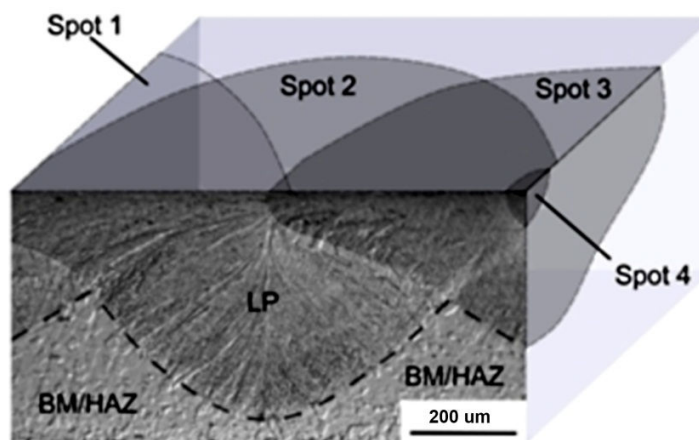


**Figure 6.2: Cross-sectional image of processed sample with partial penetration identifying the LP and BM/HAZ regions. Figure is adapted from [22].**

Also, corrosion fatigue is always a concern for materials as dynamic as NiTi SMAs. However, when the material becomes non-homogenous, the concerns associated with corrosion fatigue increase. Two different corrosion fatigue set-ups should be investigated to test the long term stability of the surface oxide after laser modification. The first test would be constant load in a corrosive environment, simulating the real life application of stents and arch wires. The second

test would be a cyclic fatigue test in a corrosive environment, simulating any type of actuator. Since these laser-processed NiTi SMAs have a non-homogeneous composition, different areas may deform to different extents or at different times when an external stimuli is applied. This could cause more severe damage to the surface oxide than is observed on a homogeneous NiTi SMA.

Before biomedical applications can be realized, additional testing is required. Biocompatibility is not just a measure of corrosion performance. Ni ion release tests must be performed in order to guarantee that patients will not have allergic reactions to the NiTi after these surface treatments have been performed. Some biomedical applications may also require the testing of cytotoxicity and platelet adhesion, among others.

### **6.3.4 Additional Materials**

Dissimilar joining of NiTi SMAs is a crucial element to incorporating these materials into larger working systems. Recent interest has been shown in the welding of NiTi to the Ni alloy MP35N for biomedical applications [124]. Before such a weld can be implemented, the corrosion performance must be characterized to ensure the reliability of the joint.

The present study looked at only NiTi, but NiTiX ternary alloys are sometimes used for their beneficial mechanical properties (see Section 2.1.6 Ternary SMAs). If laser processing is performed with ternary alloys, the stability of the surface oxide must be characterized. The post-process surface treatments used in this study also be investigated to determine if they sufficiently restore the stability of the oxide when these other alloying elements are present in the surface oxide.

## References

1. A.C. Keefe, G.P. McKnight, G.A. Herrera, P.A. Bedegi, Development of a shape memory alloy heat engine through experiment and modeling, in: Proceedings of the ASME 2011 Conference on Smart Materials, Adaptive Structures and Intelligent Systems, Phoenix, Arizona, USA, 18-21 September (2011).
2. T. Luchetti, A. Zanella, M. Biasiotto, A. Saccagno, Electrically Actuated Antiglare Rear-View Mirror Based on Shape Memory Alloy Actuator, *Journal of Materials Engineering and Performance* 18 (2009) 717.
3. A.R. Pelton, D. Stockel, T.W. Duerig, Medical uses of Nitinol, in: Proceedings of the International Symposium on Shape Memory Materials, Kanazawa, Japan, May 1999, Vols. 327-328, *Materials Science Forum*, (2000) 63.
4. D. Stockel, A. Pelton, T. Duerig, Self-expanding Nitinol stents: material and design considerations, *European Radiology* 14 (2004) 292.
5. F. Miura, M. Mogi, Y. Ohura, H. Hamanaka, The super-elastic property of the Japanese NiTi alloy wire for use in orthodontics, *American Journal of Orthodontics and Dentofacial Orthopedics* 90 (1986) 1.
6. T.G. Frank, W. Xu, A. Cuschieri, Instruments based on shape-memory alloy properties for minimal access surgery, interventional radiology and flexible endoscopy, *Minimally Invasive Therapy and Allied Technologies* 9 (2000) 89.
7. T. Duerig, A. Pelton, D. Stöckel, An overview of Nitinol medical device applications, *Material Science and Engineering A* 273-275 (1999) 149.
8. J.M. Jani, M. Leary, A. Subic, M.A. Gibson, A review of shape memory alloy research, applications and opportunities, *Materials and Design* (2014) in press.
9. P. Sevilla, F. Martorell, C. Libenson, J.A. Planell, F.J. Gil, Laser welding of NiTi orthodontic archwires for selective force application, *Journal of Materials Science: Materials in Medicine* 19 (2008) 525.
10. Q. Meng, Y. Liu, H. Yang, B.S. Shariat, T.H. Nam, Functionally graded NiTi strips prepared by laser surface anneal. *Acta Materialia* 60 (2012) 1658.
11. M. Daly, A. Pequegnat, Y. Zhou, M.I. Khan, Fabrication of a novel laser-processed NiTi shape memory microgripper with enhanced thermomechanical functionality, *Intelligent Material Systems and Structures* 24 (2013) 984.

12. M. Daly, A. Pequegnat, Y. Zhou, M.I. Khan, Enhanced thermomechanical functionality of a laser processed hybrid NiTi-NiTiCu shape memory alloy, *Smart Materials and Structures* 21 (2012) 045028.
13. M.I. Khan, A. Pequegnat, Y. Zhou, Multiple memory shape memory alloys, *Advanced Engineering Materials* 15 (2013) 386.
14. F. Villiermaux, M. Tabrizian, L'H. Yahia, M. Meunier, D.L. Piron, Excimer laser treatment of NiTi shape memory alloy biomaterials. *Applied Surface Science* 109-110 (1997) 62.
15. H.C. Man, Z.D. Cui, T.M. Yue, Corrosion properties of laser surface melted NiTi shape memory alloy, *Scripta Materialia* 45 (2001) 1447.
16. Z.D. Cui, H.C. Man, X.J. Yang, The corrosion and nickel release behavior of laser surface-melted NiTi shape memory alloy in Hanks' solution, *Surface & Coatings Technology* 192 (2005) 347.
17. X.J. Yan, D.Z. Yang, Corrosion resistance of laser spot-welded joint of NiTi wire in simulated human body fluids, *Journal of Biomedical Materials Research* 77A (2006) 97.
18. X.J. Yan, D.Z. Yang, X.P. Liu, Electrochemical behavior of YAG laser-welded NiTi shape memory alloy, *Transactions of Nonferrous Metals Society of China* 16 (2006) 572.
19. X.J. Yan, D.Z. Yang, X.P. Liu, Corrosion behavior of a laser-welded NiTi shape memory alloy, *Materials Characterization* 58 (2007) 623.
20. C.W. Chan, H.C. Man, T.M. Yue, Effect of post-weld heat-treatment on the oxide film and corrosion behavior of laser-welded shape memory NiTi wires, *Corrosion Science* 56 (2012) 158.
21. C.W. Chan, H.C. Man, T.M. Yue, Susceptibility to stress corrosion cracking of NiTi laser weldment in Hanks' solution, *Corrosion Science* 57 (2012) 260.
22. A. Pequegnat, A. Michael, J. Wang, K. Lian, Y. Zhou, M.I. Khan, Effects of laser processing on surface characteristics of NiTi shape memory alloys, Submitted to *Corrosion Science*, Mar. 2014, Manuscript No. CORSCI-D-14-00269.
23. Y.T. Hsu, Y.R. Wang, S.K. Wu, C. Chen, Effect of CO<sub>2</sub> laser welding on the shape memory and corrosion characteristics of TiNi alloys, *Metallurgical and Materials Transactions A* 32 (2001) 569-76.

24. G.B. Kauffman, I. Mayo, The story of Nitinol: the serendipitous discovery of the memory metal and its applications, *The Chemical Educator* 2 (1997) 1.
25. L.C. Chang, T.A. Read, Plastic deformation and diffusionless phase changes in metals - The Gold-Cadmium beta phase, in: *AIME Transactions* 189 (1951) 47.
26. M.W. Burkart, T.A. Read, Diffusionless phase change in the Indium-Thallium system, in: *AIME Transactions* 197 (1953) 1516.
27. K. Otsuka, X. Ren, Physical metallurgy of Ti-Ni-based shape memory alloys, *Progress in Materials Science* 50 (2005) 511.
28. T.W. Duerig, K.N. Melton, D. Stockel, C.M. Wayman, *Engineering Aspects of Shape Memory Alloys*, Butterworth-Heinemann Ltd., London (1990).
29. S. Shabalovskaya, J. Anderegg, J. Van Humbeeck, Critical overview of Nitinol surfaces and their modifications for medical applications, *Acta Biomaterialia*, 4 (2008) 447.
30. C.P. Frick, A.M. Ortega, J. Tyber, A.E.M. Maksoud, H.J. Maier, Y. Liu, K. Gall, Thermal processing of polycrystalline NiTi shape memory alloys, *Materials Science and Engineering A*, 405 (2005) 34.
31. P.C. Hall, Resistance welding Ti-rich Nitinol wire, in: *Proceedings of the International Conference on Shape Memory and Superelastic Technologies*, Pacific Grove, California, USA, 30 April-4 May 2000, SMST-2000, SMST The International Organization on Shape Memory and Superelastic Technology, Fremont, CA, USA (2001) 67.
32. M.I. Khan, Pulsed Nd:YAG Laser Processing of Nitinol. PhD thesis, University of Waterloo, Ontario, Canada (2011).
33. R.E. Reed-Hill, R. Abbaschian, *Physical Metallurgy Principles: Third Edition*, PWS Publishing Company, Boston, USA (1994).
34. T.B. Massalski, H. Okamoto, P.R. Subramanian, L. Kacprzak (Ed), *Binary Alloy Phase Diagrams 2<sup>nd</sup> Edition*, ASM International, Materials Park, Ohio, USA (1990).
35. K. Otsuka, C.M. Wayman (Ed), *Shape Memory Materials*, Cambridge University Press, New York, NY, USA (1998).
36. D.C. Lagoudas (Ed), *Shape Memory Alloys: Modeling and Engineering Applications*, Springer (2008).
37. T.V. Philip, P.A. Beck, CsCl-type ordered structures in binary alloys of transition elements, *AIME Transactions* 209 (1957) 1269.

38. K. Otsuka, T. Sawamura, K. Shimizu, Crystal structure and internal defects of equiatomic TiNi martensite, *Physica Status Solidi A* 5 (1971) 457.
39. X. Huang, G.J. Ackland, K. Rabe, Crystal structures and shape-memory behavior of NiTi, *Nature Materials* 2 (2003) 307.
40. E. Hornbogen, Surface upheavals, pseudo martensite, and martensite ghosts, *Praktische Metallographie* 42 (2005) 445.
41. S.P. Gupta, A.A. Johnson, Morphology and crystallography of  $\beta'$  martensite in TiNi alloys, *Materials Transactions, The Japan Institute of Metals* 14 (1973) 292.
42. T. Onda, Y. Bando, T. Ohba, K. Otsuka, Electron microscopy study of twins in martensite in a Ti-50.0at%Ni alloy, *Materials Transactions, The Japan Institute of Metals* 33 (1992) 354.
43. K.N. Melton, O. Mercier, Fatigue of NiTi thermoelastic martensites, *Acta Metallurgica* 27 (1979) 137.
44. American Society for Testing and Materials (ASTM) Standard Terminology for Nickel-Titanium Shape Memory Alloys, ASTM F2005, ASTM International, West Conshohocken, PA (2009).
45. B. Tam, Micro-Welding of Nitinol Shape Memory Alloy, MAsC thesis, University of Waterloo, Ontario, Canada (2010).
46. American Society for Testing and Materials (ASTM) Standard Test Method for Transformation Temperature of Nickel-Titanium by Thermal Analysis, Standard F2004, ASTM International, West Conshohocken, PA (2009).
47. R.F. Hamilton, H. Sehitoglu, Y. Chumlyakov, H.J. Maier, Stress dependence of the hysteresis in single crystal NiTi alloys, *Acta Materialia* 52 (2004) 3383.
48. T.H. Nam, T. Saburi, K. Shimizu, Cu-content dependence of shape memory characteristics in Ti-Ni-Cu alloys, *Materials Transactions, The Japan Institute of Metals* 31 (1990) 959.
49. M. Piao, K. Otsuka, S. Miyazaki, H. Horikawa, Mechanism of the  $A_s$  temperature increase by pre-deformation in thermoelastic alloys, *Materials Transactions, Japan Institute for Materials* 34(1993) 919.

50. A. Pequegnat, Novel Laser Based NiTi Shape Memory Alloy Processing Protocol for Medical Device Applications, PhD Thesis, University of Waterloo, Waterloo, Ontario, Canada (2012).
51. Y. Liu, Z. Xie, J. Van Humbeeck, L. Delaey, Some results on the detwinning process in NiTi shape memory alloys, *Scripta Materialia*, 41 (1999) 1273.
52. S. Miyazaki, K. Otsuka, Y. Suzuki, Transformation pseudoelasticity and deformation behavior in a Ti-50.5at%Ni alloy, *Scripta Metallurgica* 15 (1981) 287.
53. A.R. Pelton, J. DiCello, S. Miyazaki, Optimisation of processing and properties of medical grade Nitinol wire, *Minimally Invasive Therapy Allied Technologies* 9 (2000) 107.
54. D. Favier, Y. Liu, L. Orgéas, A. Sandel, L. Debove, P. Comte-Gaz, Influence of thermomechanical processing on the superelastic properties of a Ni-rich Nitinol shape memory alloy, *Materials Science and Engineering A* 429 (2006) 130.
55. K. Otsuka, K. Shimizu, Pseudoelasticity and shape memory effects in alloys, *International Metals Reviews* 31 (1986) 93.
56. S. Miyazaki, Y. Ohmi, K. Otsuka, Y. Suzuki, Characteristics of deformation and transformation pseudoelasticity in Ti-Ni alloys, *Journal de Physique Colloques* 43 (1982) 255.
57. W. Tang, Thermodynamic study of the low-temperature phase, B19' and martensitic transformation in near equiatomic Ti-Ni shape memory alloys, *Metallurgical Materials Transactions A* 28 (1997) 537.
58. S. Miyazaki, T. Hashinaga, A. Ishida, Martensitic transformations in sputter deposited Ti-Ni-Cu shape memory alloy thin films, *Thin Solid Films* 281 (1996) 364.
59. K.H. Eckelmeyer, The effect of alloying on the shape memory phenomenon in Nitinol, *Scripta Metallurgica* 10 (1976) 667.
60. H.C. Donkersloot, J.H.N. Van Vucht, Martensitic transformations in gold-titanium, palladium-titanium and platinum-titanium alloys near the equiatomic composition, *Journal of the Less Common Metals*, 20 (1970) 83.
61. D.R. Angst, P.E. Thoma, M.Y. Kao, The effect of hafnium content on the transformation temperatures of Ni<sub>49</sub>Ti<sub>51</sub>- xHf<sub>x</sub> shape memory alloys, *Journal de Physique IV* 5 (1995) 747.

62. D.R. Lide (Ed), CRC Handbook of Chemistry and Physics 84<sup>th</sup> Edition, CRC Press, Inc., Boca Raton, Florida, USA (2003).
63. V. Schroeder, Evolution of the passive film on mechanically damaged nitinol, *Journal of Biomedical Materials Research A* 90 (2009) 1.
64. L. Zhu, J.M. Fino, A.R. Pelton, Oxidation of Nitinol, in: *Proceedings of Smart Materials and Superelastic Technologies*, California, USA (2003).
65. S.A. Shabalovskaya, Surface, corrosion and biocompatibility aspects of nitinol as an implant material, *Bio-Medical Materials and Engineering* 12 (2002) 69.
66. D.J. Wever, A.G. Veldhuizen, J. de Vries, H.J. Busscher, D.R.A. Uges, J.R. van Horn, Electrochemical and surface characterization of a nickel-titanium alloy, *Biomaterials* 19 (1998) 761.
67. A.R. Pelton, A. Mehta, L. Zhu, C. Trepanier, V. Imbeni, S. Robertson, M. Barney, A. Minor, TiNi oxidation: kinetics and phase transformations, in: J.M. Howe, D.E. Laughlin, J.K. Lee, U. Dahmen, W.A. Soffa (Ed), *Solid-to-Solid Transformations in Inorganic Materials 2005 – Vol. 2: Phase Transformations in Novel Systems or Special Materials*, TMS, (2005) 1029.
68. R.A. Zavanelli, A.S. Guilherme, G.E. Pessanha-Henriques, M. Antonio de Arruda Nobilo, M.F. Mesquita, Corrosion-fatigue of laser-repaired commercially pure titanium and Ti-6Al-4V alloy under different test environments, *Journal of Oral Rehabilitation* 31 (2004) 1029.
69. S.A. Shabalovskaya, G.C. Rondelli, A.L. Undisz, J.W. Anderegg, T.D. Burleigh, M.E. Rettermayr, The electrochemical characteristics of native Nitinol surface, *Biomaterials* 30 (2009) 3662.
70. D.T.K.Kwok, M. Shulz, T. Hu, C. Chu, P. Chu, Surface treatments of nearly equiatomic NiTi alloy (Nitinol) for surgical implants, in: A. Laskovski (Ed), *Biomedical Engineering, Trends in Materials Science*, InTech, Rijeka, Croatia (2011) 269.
71. O. Cissé, O. Savadogo, M. Wu, L'H. Yahia, Effect of surface treatment of NiTi alloy on its corrosion behavior in Hanks' solution, *Journal of Biomedical Materials Research* 61 (2001) 339.
72. C.M. Chan, S. Trigwell, T. Duerig, Oxidation of an NiTi alloy, *Surface and Interface Analysis* 15 (1990) 349.

73. A. Undisz, F. Schrepel, W. Wesch, M. Rettenmayr, In situ observation of surface oxide layers on medical grade Ni-Ti alloy during straining, *Journal of Biomedical Materials Research A* 88 (2009) 1000.
74. S. Shabalovskaya, J. Anderegg, F. Laab, P.A. Thiel, G. Rondelli, Surface conditions of Nitinol wires, tubing, and as-cast alloys: the effect of chemical etching, aging in boiling water, and heat treatment, *Journal of Biomedical Materials Research A: Applied Biomaterials* 65 (2003) 193.
75. D. Vojtech, J. Kubasek, M. Voderova, P. Seda, A. Michalcova, Study of mechanical, fatigue and corrosion, properties of the superelastic Ni-Ti alloy, in: *Proceedings of the 20<sup>th</sup> Anniversary International Conference on Metallurgy Materials*, Czech Republic, EU (2011) 1.
76. D. Vojtech, M. Voderova, J. Fojt, P. Novak, T. Kubasek, Surface structure and corrosion resistance of short-time heat-treated NiTi shape memory alloy, *Applied Surface Science*, 257 (2010) 1573.
77. D.A. Armitage, D.M. Grant, Characterisation of surface-modified nickel titanium alloys, *Materials Science and Engineering A* 249 (2003) 89.
78. C.W. Bale, P. Chartrand, S.A. Degterov, G. Eriksson, K. Hack, R. Ben Mahfoud, J. Melancon, A.D. Pelton, S. Petersen, FactSage thermochemical software and databases, *Calphad* 26 (2002) 189.
79. S.A. Shabalovskaya, J.W. Anderegg, Surface spectroscopic characterization of NiTi nearly equiatomic shape memory alloys for implants, *Journal of Vacuum Science and Technology A* 13 (1995) 2624.
80. S. Trigwell, R.D. Hayden, K.F. Nelson, G. Selvaduray, Effects of treatment on the surface chemistry of NiTi alloy for biomedical applications, *Surface and Interface Analysis* 26 (1998) 483.
81. N. Munroe, C. Pulletikurthi, W. Haider, Enhanced biocompatibility of porous Nitinol, *Journal of Materials Engineering and Performance* 18 (2009) 765.
82. P. Filip, J. Lausmaa, J. Musialek, K. Mazanec, Structure and surface of NiTi human implants, *Biomaterials* 22 (2001) 2131.

83. K'I. Yokoyama, Y. Yazaki, J'I. Sakai, Inhibition of hydrogen embrittlement of Ni-Ti superelastic alloy in acid fluoride solution by hydrogen peroxide addition, *Journal of Biomedical Materials Research A* 98 (2011) 404.
84. A. Michiardi, C. Aparicio, J.A. Planell, F.J. Gil, New oxidation treatment of NiTi shape memory alloys to obtain Ni-free surfaces and to improve biocompatibility, *Journal of Biomedical Materials Research A: Applied Biomaterials* 77 (2006) 249.
85. O. Kubaschewski, B.E. Hopkins, *Oxidation of Metals and Alloys*, Butterworths, London, UK (1953).
86. W. Haider, N. Munroe, Assessment of Corrosion Resistance and Metal Ion Leaching of Nitinol Alloys, *Journal of Materials Engineering and Performance* 20 (2011) 812.
87. Z. Huan, L.E. Fratila-Apachitei, I. Apachitei, J. Duszcyk, Effect of aging treatment on the *in vitro* nickel release from porous oxide layers on NiTi, *Applied Surface Science* 274 (2013) 266.
88. S.A. Shabalovskaya, Physiochemical and biological aspects of nitinol as a biomaterial, *International Materials Reviews* 46 (2001) 233.
89. C.L. Chu, C.Y. Chung, P.K. Chu, Surface oxidation of NiTi shape memory alloy in boiling aqueous solution containing hydrogen peroxide, *Materials Science and Engineering A* 417 (2006) 104.
90. S.A. Shabalovskaya, J.W. Andereg, A. Undisz, M. Rettenmayr, G.C. Rondelli, Corrosion resistance, chemistry, and mechanical aspects of Nitinol surface formed in hydrogen peroxide solutions, *Journal of Biomedical Materials Research B: Applied Biomaterials* 100 (2012) 1490.
91. B. Thierry, M. Tabrizian, C. Trepanier, O. Savadogo, L. Yahia, Effect of surface treatment and sterilization processes on the corrosion behavior of NiTi shape memory alloy, *Journal of Biomedical Materials Research* 51 (2000) 685.
92. L. Tan, W.C. Crone, Surface characterization of NiTi modified by plasma source ion implantation, *Acta Materialia* 50 (2002) 4449.
93. S. Shabalovskaya, J. Andereg, G. Rondelli, W. Vanderlinden, S. De Feyter, Comparative *in vitro* performances of bare Nitinol surfaces, *Bio-Medical Materials Engineering* 18 (2008) 1.

94. R. Cornut, C. Lefrou, New analytical approximation of feedback approach curves with microdisk SECM tip and irreversible kinetic reaction at the substrate, *Journal of Electroanalytical Chemistry* 621 (2008) 178.
95. J.A. Von Fraunhofer, C.H. Banks, *Potentiostat and its Applications*, Butterworth & Co. Ltd., London (1972).
96. D.A. Jones, *Principles and Prevention of Corrosion: Second Edition*, Prentice-Hall, Inc., Upper Saddle River, NJ (1992).
97. W.W. Duley, *Laser Welding*, John Wiley & Sons, Inc. (1999).
98. C. Dawes, *Laser Welding*, McGraw-Hill, New York, NY (1992).
99. R.C. Crafer, P.J. Oakley (Ed), *Laser Processing in Manufacturing*, Chapman & Hall, New York, NY (1993).
100. S.S. Charschan (Ed), *Laser in Industry*, Van Nostrand Reinhold Company, New York, NY (1972).
101. Elliot Biro, *Weldability of Plated thin sheet and Cu by Pulsed Nd:YAG Laser welding*, MASC thesis, University of Waterloo, Ontario, Canada.
102. J.R. Ferraro, K. Nakamoto, C.W. Brown, *Introductory Raman Spectroscopy*, Academic Press, Boston, MA (2003).
103. American Society for Testing and Materials (ASTM) Standard Test Method for Conducting Cyclic Polarization Measurements to Determine the Corrosion Susceptibility of Small Implant Devices, Standard F2129-08, ASTM International, West Conshohocken, PA (2008).
104. American Society for Testing and Materials (ASTM) Standard Test Method for Making Potentiostatic and Potentiodynamic Anodic Polarization Measurements, Standard G5-94, ASTM International, West Conshohocken, PA (2004).
105. American Society for Testing and Materials (ASTM) Standard Test Method for Conducting Cyclic Potentiodynamic Polarization Measurements for Localized Corrosion Susceptibility of Iron-, Nickel-, or Cobalt-Based Alloys, Standard G61-86, ASTM International, West Conshohocken, PA (2009).
106. American Society for Testing and Materials (ASTM) Standard Practice for Calculation of Corrosion Rates and Related Information from Electrochemical Measurements, Standard G102-89, ASTM International, West Conshohocken, PA (1999).

107. A.J. Bard, F.-R. F. Fan, J. Kwak, O. Lev, Scanning Electrochemical Microscopy. Introduction and Principles, *Analytical Chemistry*, 61 (1989) 132.
108. G. Wittstock, M. Burchardt, S.E. Pust, Y. Shen, C. Zhao, Scanning electrochemical microscopy for direct imaging of reaction rates, *Angewandte Chemie International Edition* 46 (2007)1584.
109. A. Kiani, M.A. Apluche-Aviles, P.K. Eggers, M. Jones, J.J. Gooding, M.N. Paddon-Row, A.J. Bard, Scanning electrochemical microscopy. Effect of defects and structure on electron transfer through self-assembled monolayers, *Langmuir* 24 (2008) 2841.
110. A. Maho, J. Denayer, J. Delhalle, Z. Mekhalif, Electro-assisted assembly of aliphatic thiol, dithiol and dithiocarboxylic acid monolayers on copper, *Electrochimica Acta* 56 (2011) 3954.
111. H. Hazimeh, S. Nunige, R. Cornut, C. Lefrou, C. Combellas, F. Kanoufi, Surface reactivity from electrochemical lithography: illustration in the steady-state reductive etching of perfluorinated surfaces, *Analytical Chemistry* 83 (2011) 6106.
112. T. Matrab, F. Hauquier, C. Combellas, F. Kanoufi, Scanning electron microscopy investigation of molecular transport and reactivity within polymer brushes, *ChemPhysChem* 11 (2010) 670.
113. N. Casillas, S. Charlebois, W.H. Smyrl, H.S. White, Pitting corrosion of titanium, *Journal of The Electrochemical Society* 141 (1994) 636.
114. S.B. Basame, H.S. White, Scanning electrochemical microscopy: measurement of the current density at microscopic redox-active sites on titanium, *The Journal of Physical Chemistry B* 102 (1998) 9812.
115. A. Schulte, S. Belger, M. Etienne, W. Schuhmann, Imaging localised corrosion of NiTi shape memory alloys by means of alternating current scanning electrochemical microscopy (AC-SECM), *Materials Science and Engineering A* 378 (2004) 523.
116. S.E. Pust, D. Scharnweber, C.N. Kirchner, G. Wittstock, Heterogeneous distribution of reactivity on metallic biomaterials: scanning probe microscopy studies of the biphasic Ti alloy Ti6Al4 V, *Advanced Materials* 19 (2007) 878.
117. S. Belger, A. Schulte, C. Hessing, M. Pohl, W. Schuhmann, Alternating current scanning electrochemical microscopy (AC-SECM) studies on the surface of electrochemically

- polished NiTi shape memory alloys, *Materials Science and Engineering Technology* 35 (2004) 276.
118. D. Ruhlig, H. Gugel, A. Schulte, W. Theisen, W. Schuhmann, Visualization of local electrochemical activity and local nickel ion release on laser-welded NiTi/steel joints using combined alternating current mode and stripping mode SECM. *Analyst* 133 (2008) 1700.
  119. D.J.M. Bevan, I.E. Grey, B.T.M. Willis, The crystal structure of  $\beta$ -U<sub>4</sub>O<sub>9-y</sub>, *Journal of Solid State Chemistry* 61 (1986) 1.
  120. G. Frederico, N. Lech, T. Lionel, Channeling investigation of the crystalline structure of U<sub>4</sub>O<sub>9-y</sub>, *Physical Review B* 74 (2006) 184114.
  121. F. Garrido, A.C. Hannon, R.M. Ibberson, L. Nowicki, B.T.M. Willis, Neutron diffraction studies of U<sub>4</sub>O<sub>9</sub>: comparison with EXAFS results, *Inorganic Chemistry* 45 (2006) 8408.
  122. G.S. Firstov, R.G. Vitchev, H. Kumar, B. Blanpain, J. Van Humbeeck, Surface oxidation of NiTi shape memory alloy, *Biomaterials* 23 (2002) 4863.
  123. L.E. Eiselstein, Corrosion of Shape Memory and Superelastic Alloys, in: R.W. Revie (Ed), *Uhlig's Corrosion Handbook 3rd Edition*, Ottawa, ON, Canada (2011) 529.
  124. B. Panton, A. Michael, A. Pequegnat, M. Daly, Y.N. Zhou, M.I. Khan, An innovative laser-processed NiTi self-biasing linear actuator, in: *Proceedings of the ASME 2013 Conference on Smart Materials, Adaptive Structures and Intelligent Systems*, Snowbird, Utah, USA (2013).

## Appendix I: Additional SECM Analysis

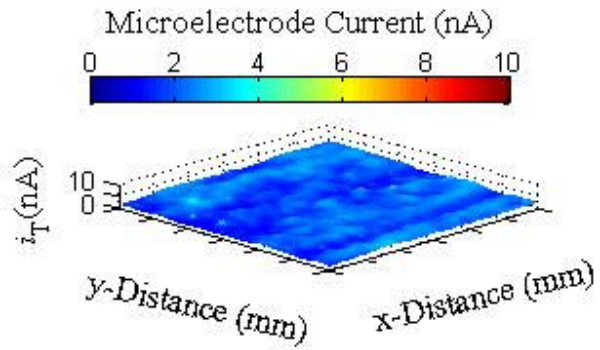


Figure A-I.1: SECM feedback image of a typical CE surface.

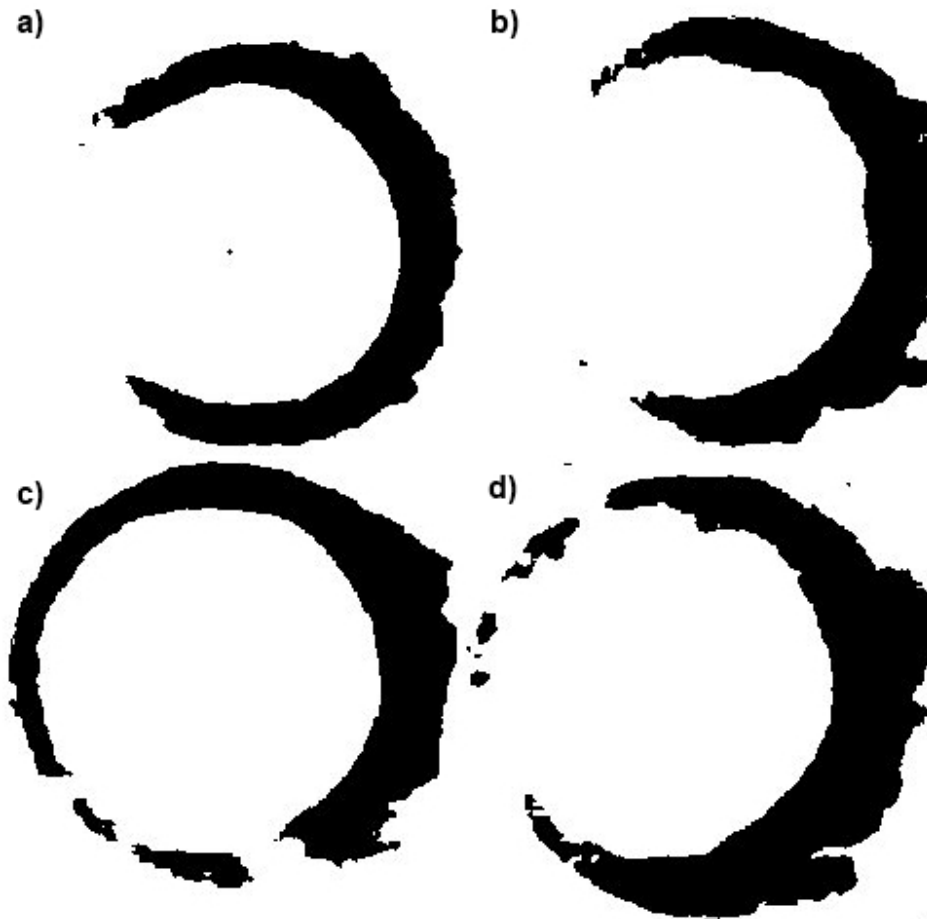


Figure A-I.2: Surface areas of reactive regions estimated from SECM feedback maps for a) 1LP, b) 3LP, c) 4LP and d) 5LP. Black regions are conductive areas, white regions are insulating areas.

## Appendix II: Experimental Data for Raman Tests

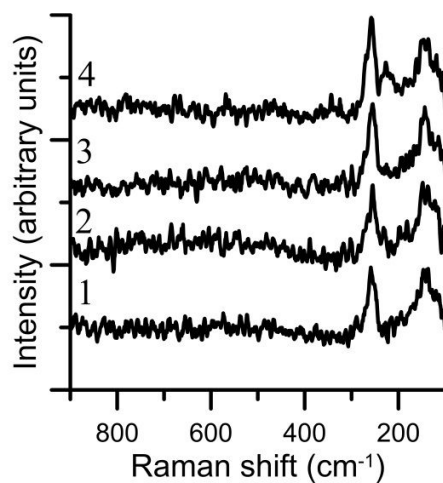


Figure A-II.1: Raman spectra for CE samples 1 to 4.

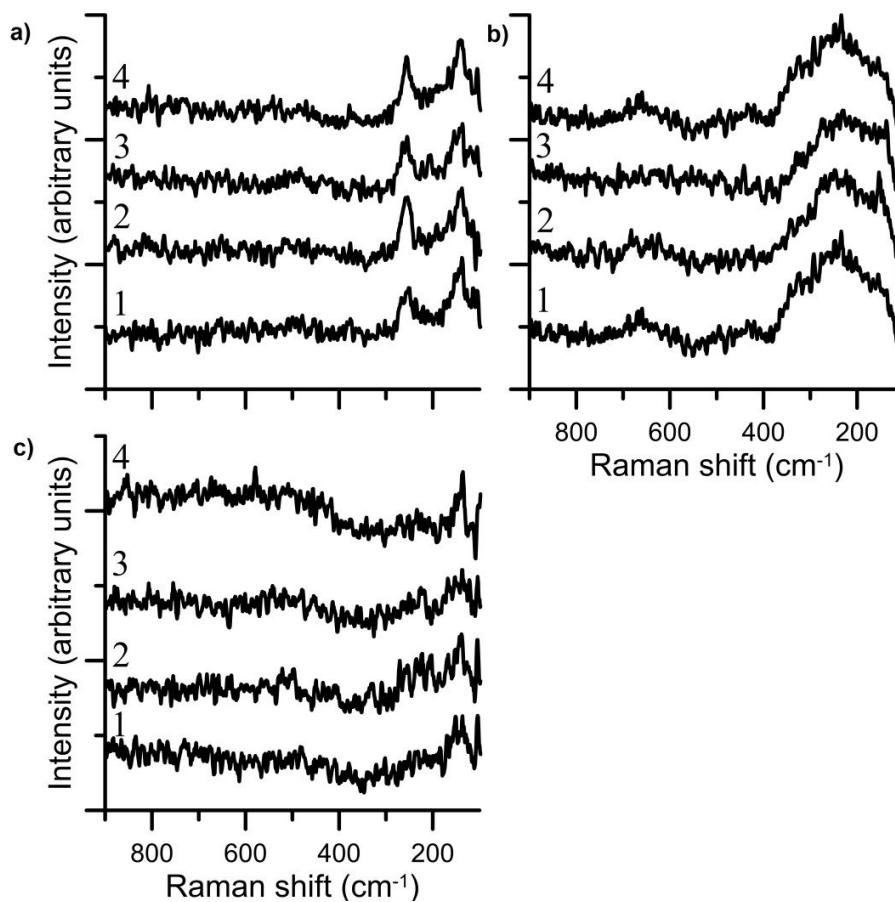
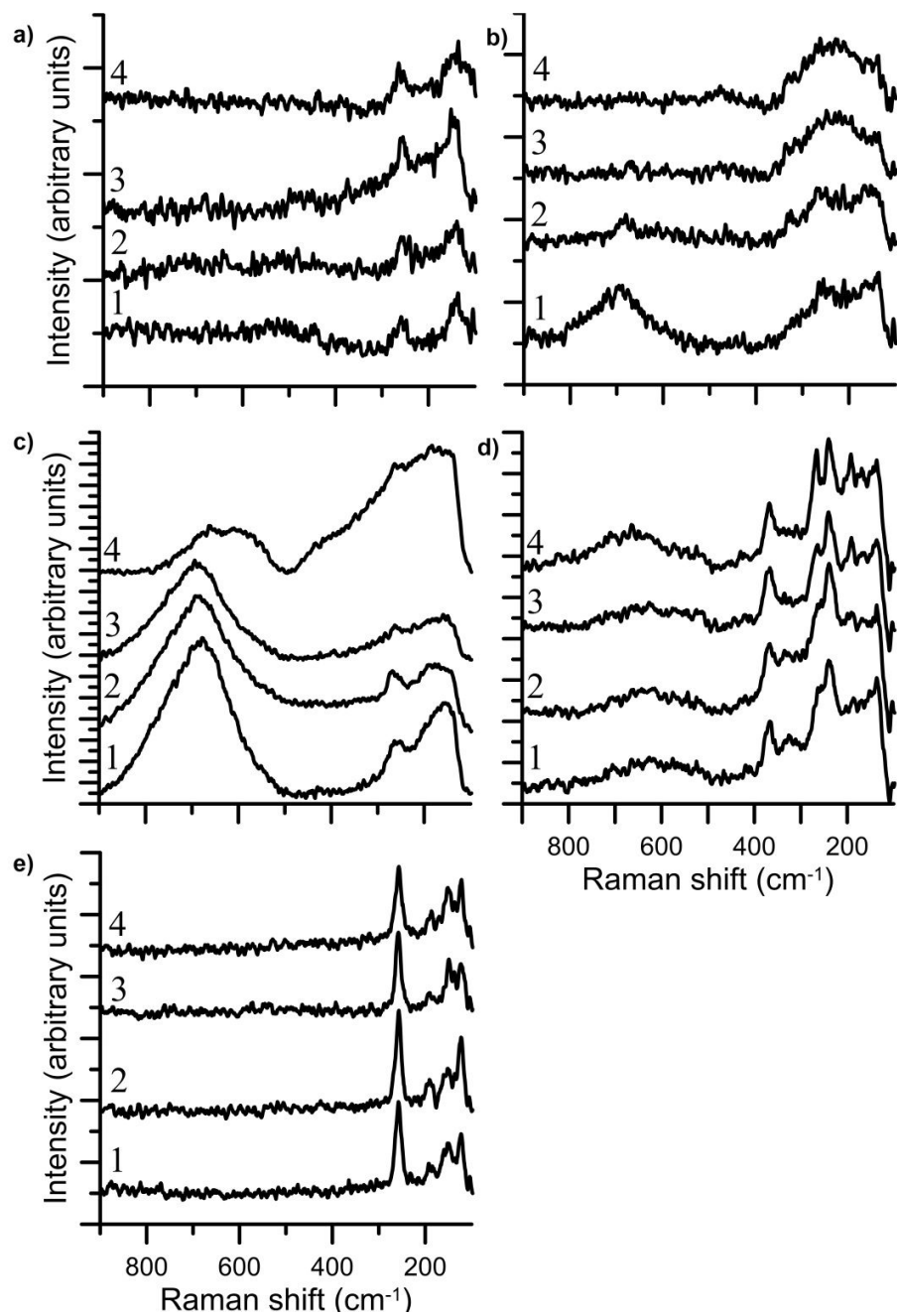
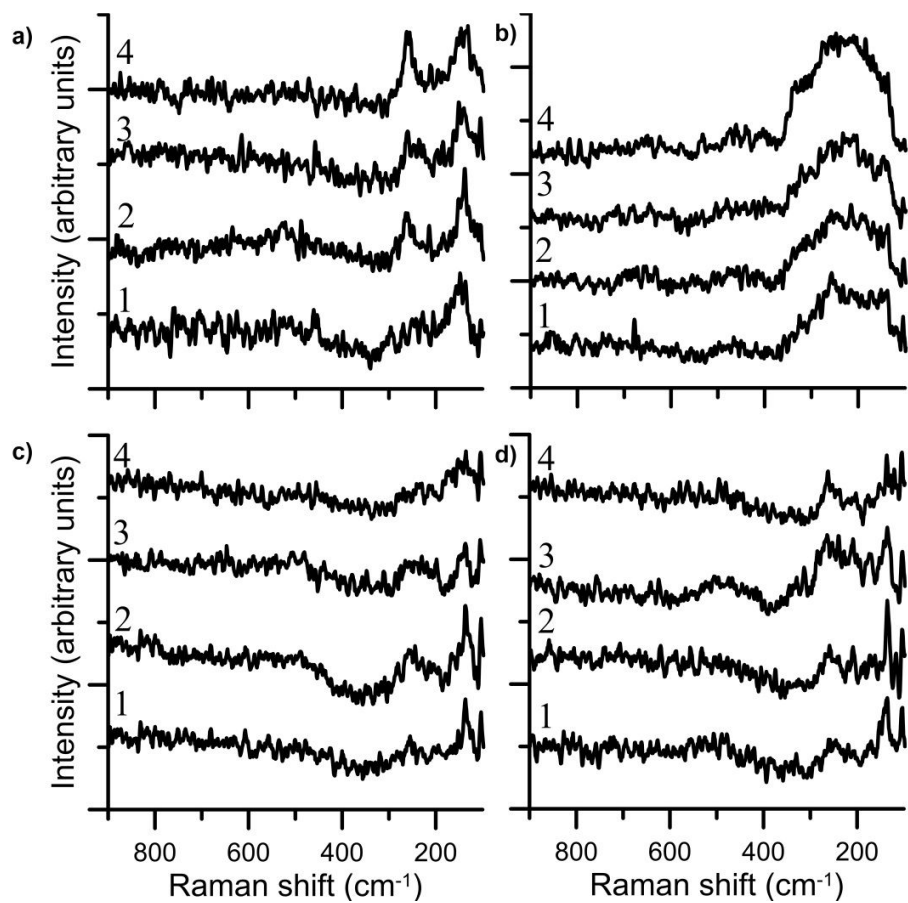


Figure A-II.2: Raman spectra for 1LP samples 1 to 4 in the a) CE region, b) HAZ region and c) LP region.



**Figure A-II.3: Raman spectra for 5LP samples 1 to 4 in the a) CE region, b) HAZ1 region, c) HAZ2 region, d) HAZ3 region and e) LP region.**



**Figure A-II.4: Raman spectra for 1LPO samples 1 to 4 in the a) CE region, b) outer HAZ region, c) LP region and d) the inner HAZ region.**

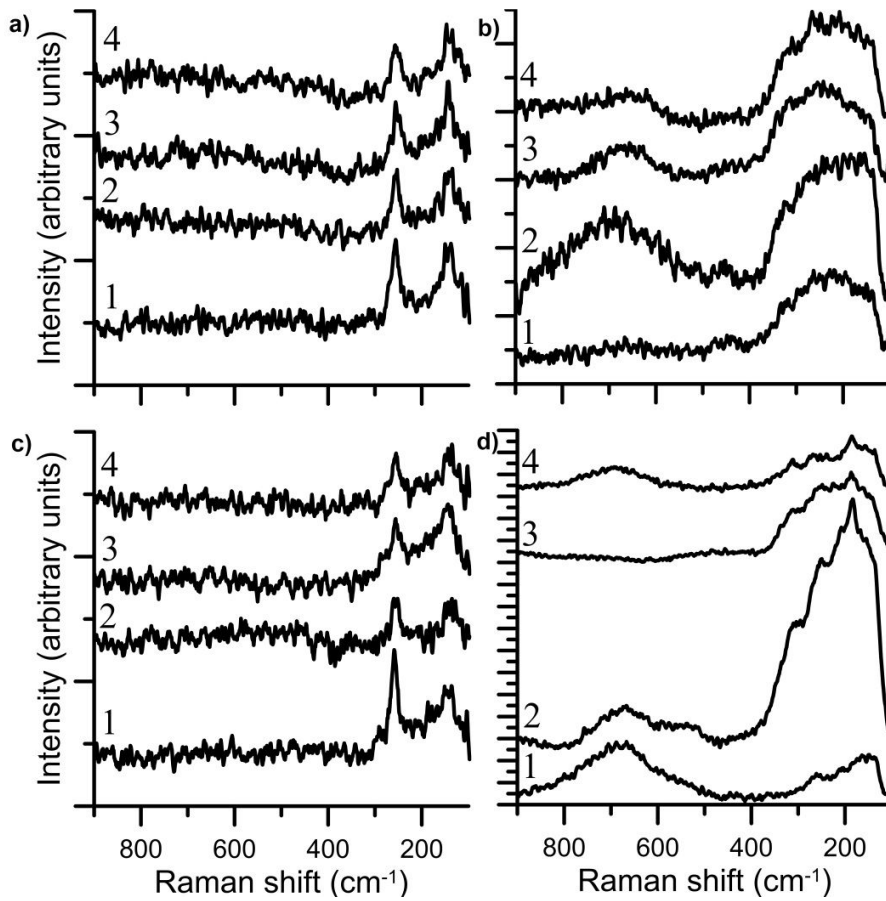


**Figure A-II.5: Raman spectra for 5LPO samples 1 to 4 in the a) CE region, b) outer HAZ region, c) LP region and d) the inner HAZ region.**

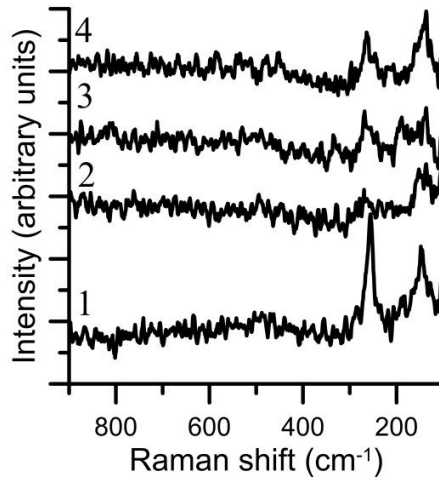


**Figure A-II.6: Raman spectra for LPMP samples 1 to 4.**

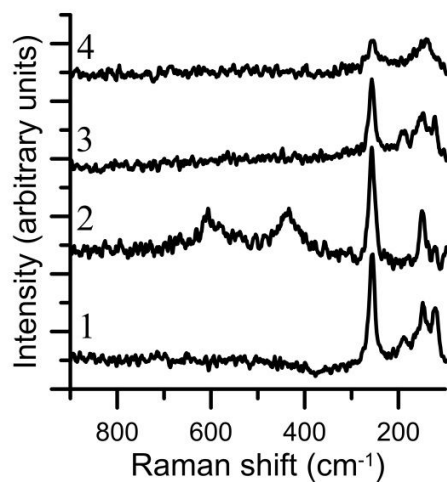


**Figure A-II.7: Raman spectra for LPCE samples 1 to 4.**

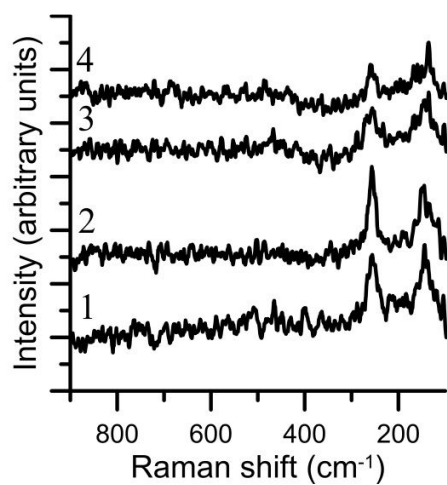


**Figure A-II.8: Raman spectra for LPMPBW samples 1 to 4.**

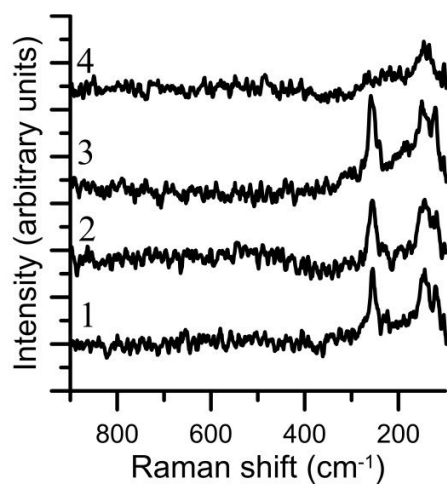


**Figure A-II.9: Raman spectra for LPCEBW samples 1 to 4.**

### Appendix III: Experimental Data for Cyclic Polarization Tests

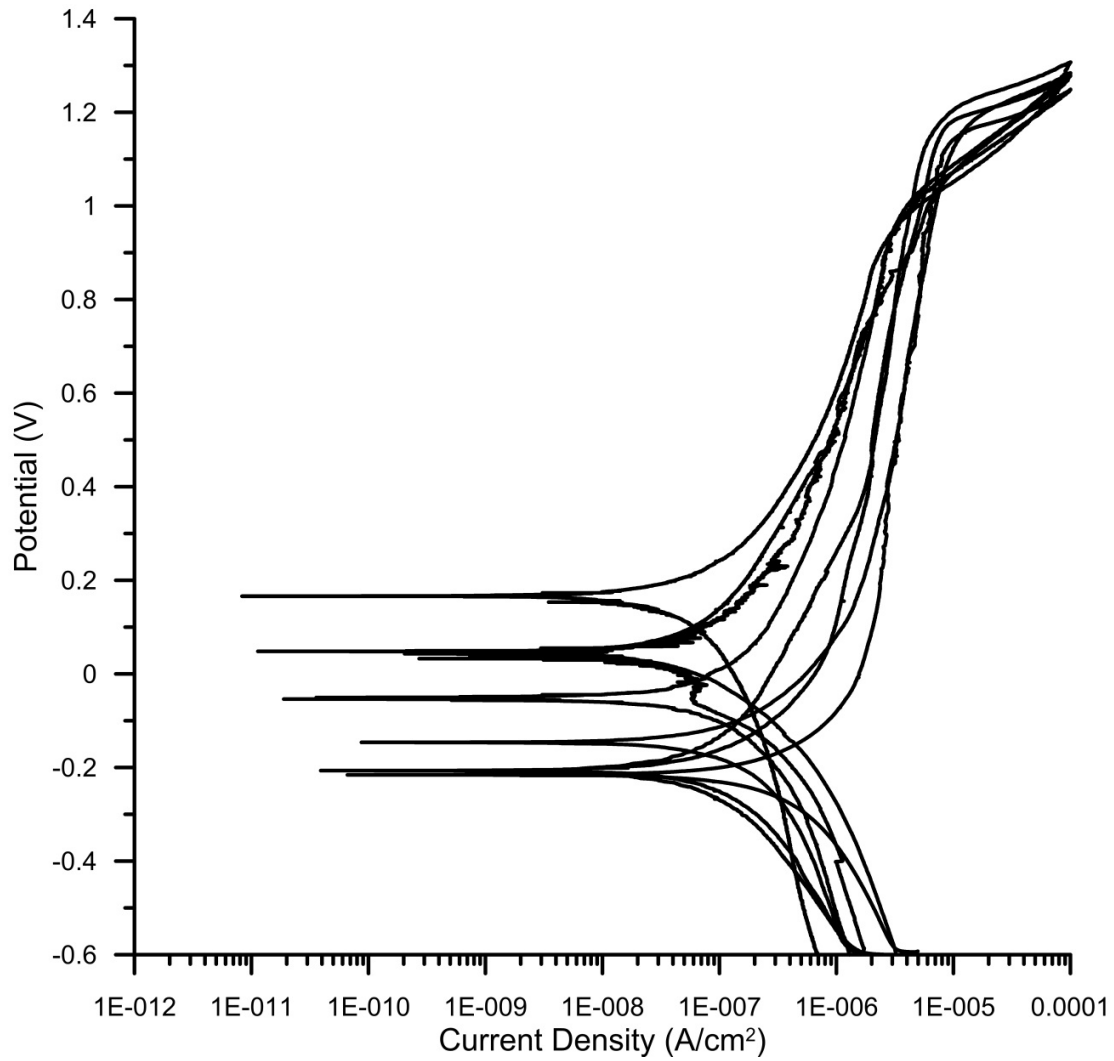
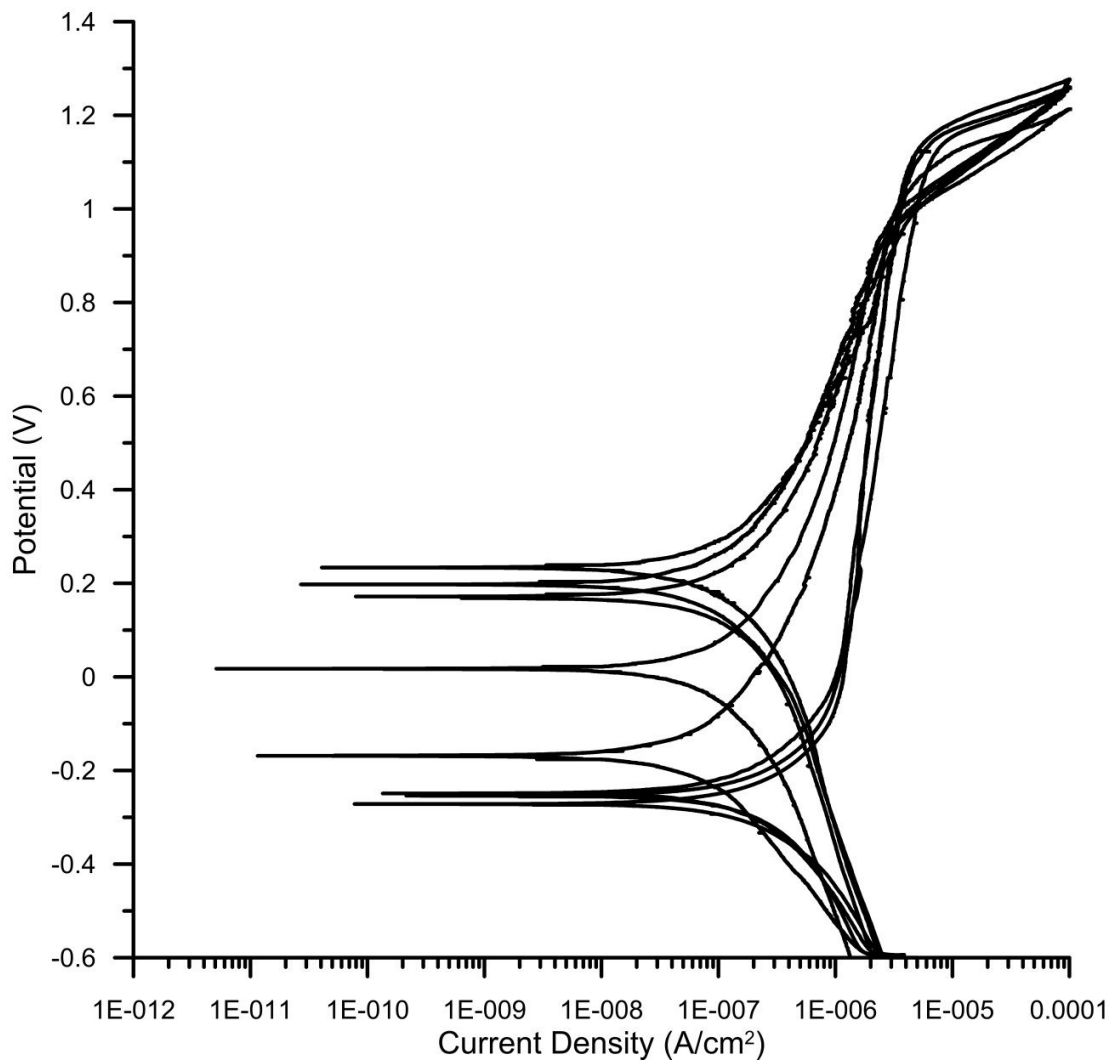


Figure A-III.1: Cyclic polarization curves for CE samples 1 to 4.

Table A-III.1: Cyclic Polarization Values for CE

Sample	$E_{\text{corr}}$ (V)	$i_{\text{corr}}$ ( $\mu\text{A}/\text{cm}^2$ )	$E_{\text{break}}$ (V)	$E_{\text{prot}}$ (V)	$i_{\text{prot}}$ ( $\mu\text{A}/\text{cm}^2$ )
CE 1	-0.206	1.15	1.164	1.007	5.44
CE 2	-0.146	2.81	1.181	1.044	7.77
CE 3	-0.207	0.29	1.197	1.015	4.46
CE 4	-0.216	3.86	1.139	1.040	7.01
Average	-0.194	2.03	1.170	1.027	6.17
Std. Dev.	0.032	1.61	0.025	0.018	1.50



**Figure A-III.2: Cyclic polarization curves for 1LP samples 1 to 4.**

**Table A-III.2: Cyclic Polarization Values for 1LP**

<b>Sample</b>	<b><math>E_{\text{corr}}</math> (V)</b>	<b><math>i_{\text{corr}}</math> (<math>\mu\text{A}/\text{cm}^2</math>)</b>	<b><math>E_{\text{break}}</math> (V)</b>	<b><math>E_{\text{prot}}</math> (V)</b>	<b><math>i_{\text{prot}}</math> (<math>\mu\text{A}/\text{cm}^2</math>)</b>
1LP 1	-0.168	0.20	1.090	0.945	2.80
1LP 2	-0.249	1.91	1.131	0.966	3.46
1LP 3	-0.272	1.99	1.135	0.990	3.45
1LP 4	-0.254	2.39	1.127	0.995	4.95
Average	-0.236	1.62	1.121	0.974	3.67
Std. Dev.	0.046	0.97	0.021	0.023	0.91

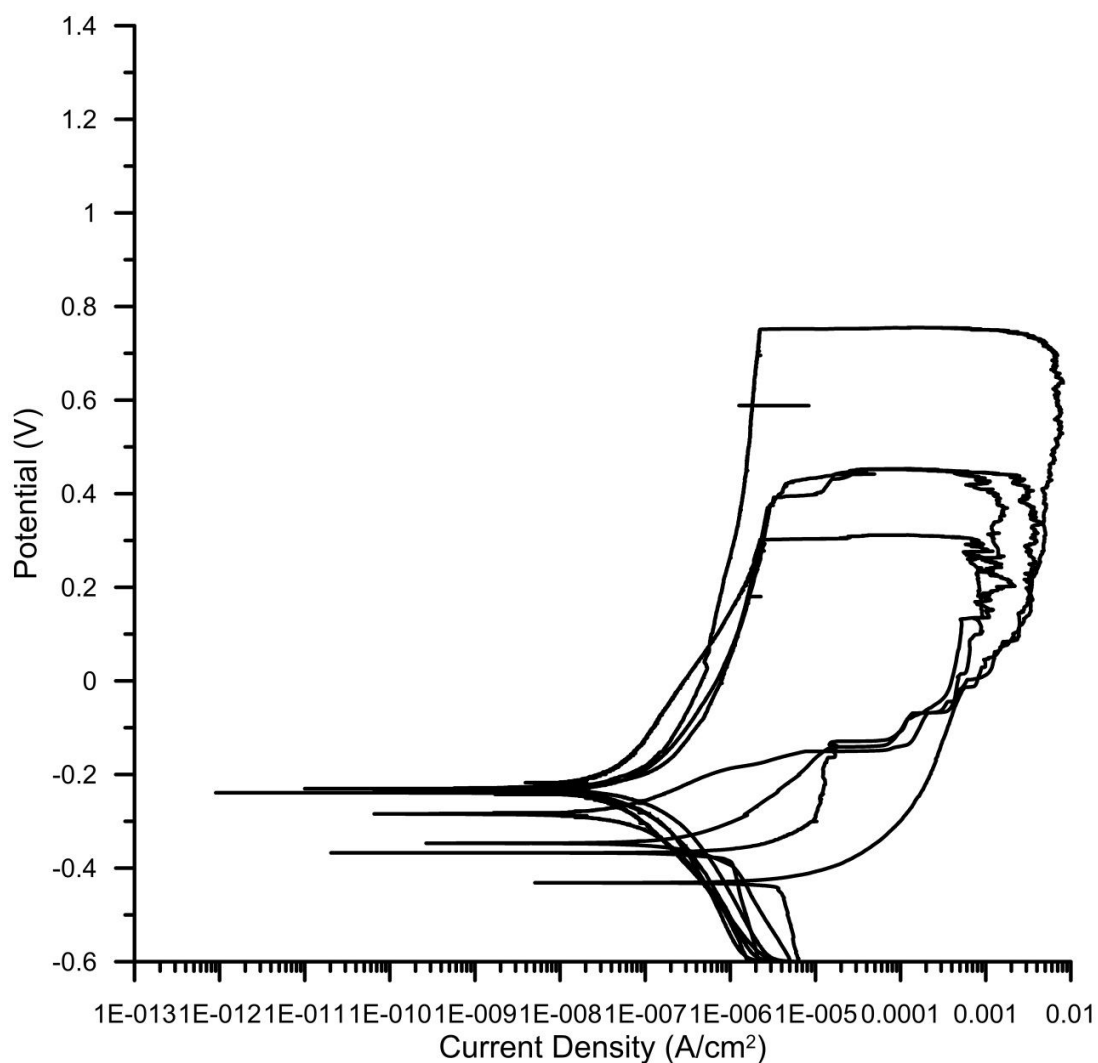


**Figure A-III.3: Cyclic polarization curves for 5LP samples 1 to 4.**

**Table A-III.3: Cyclic Polarization Values for 5LP**

Sample	$E_{\text{corr}}$ (V)	$i_{\text{corr}}$ ( $\mu\text{A}/\text{cm}^2$ )	$E_{\text{break}}$ (V)	$E_{\text{prot}}$ (V)	$i_{\text{prot}}$ ( $\mu\text{A}/\text{cm}^2$ )
5LP 1	-0.230	0.57	0.304	n/a	n/a
5LP 2	-0.233	3.84	0.752	n/a	n/a
5LP 3	-0.239	2.19	0.455	n/a	n/a
5LP 4	-0.231	3.47	0.395	n/a	n/a
Average	-0.233	2.52	0.477	n/a	n/a
Std. Dev.	0.004	1.48	0.194	n/a	n/a

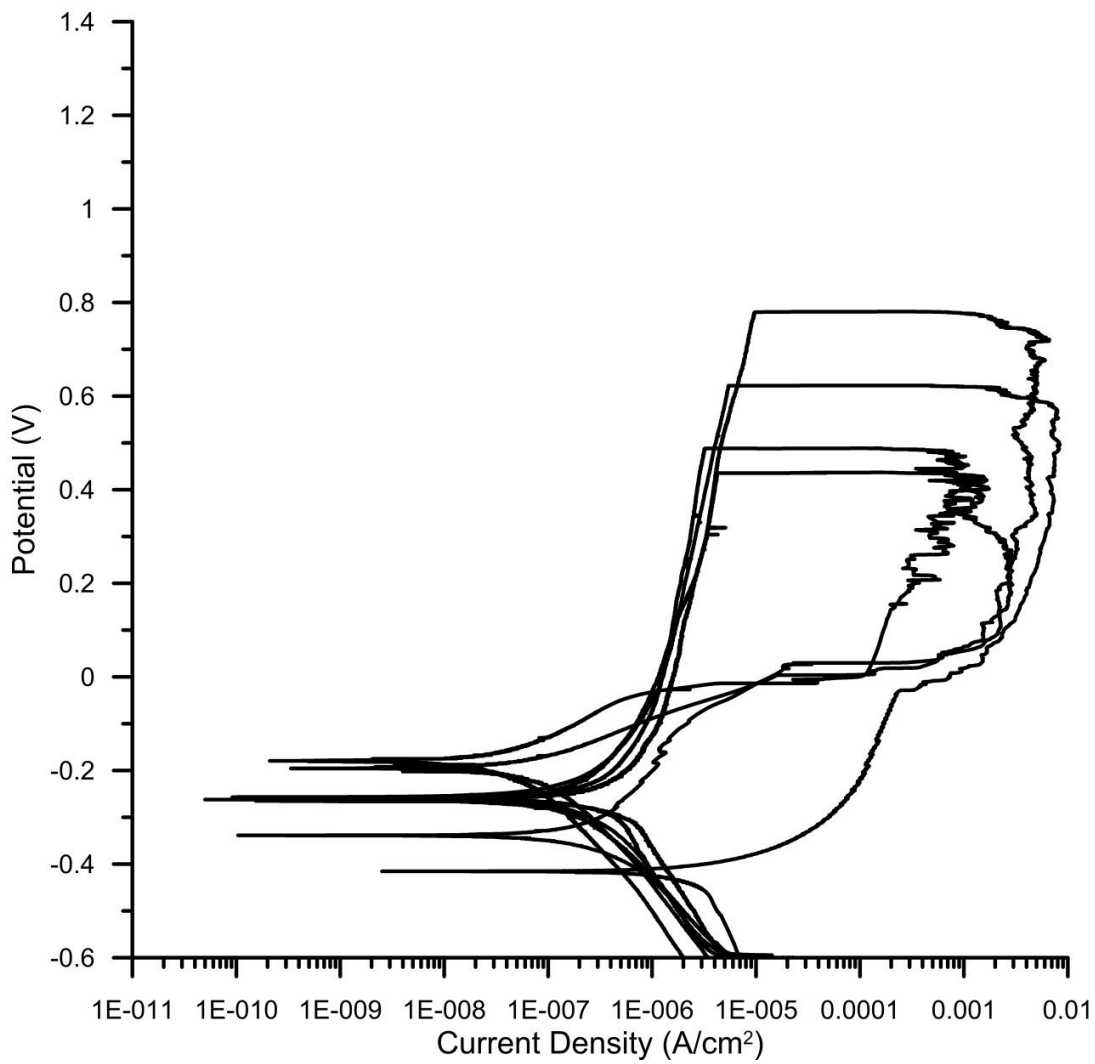
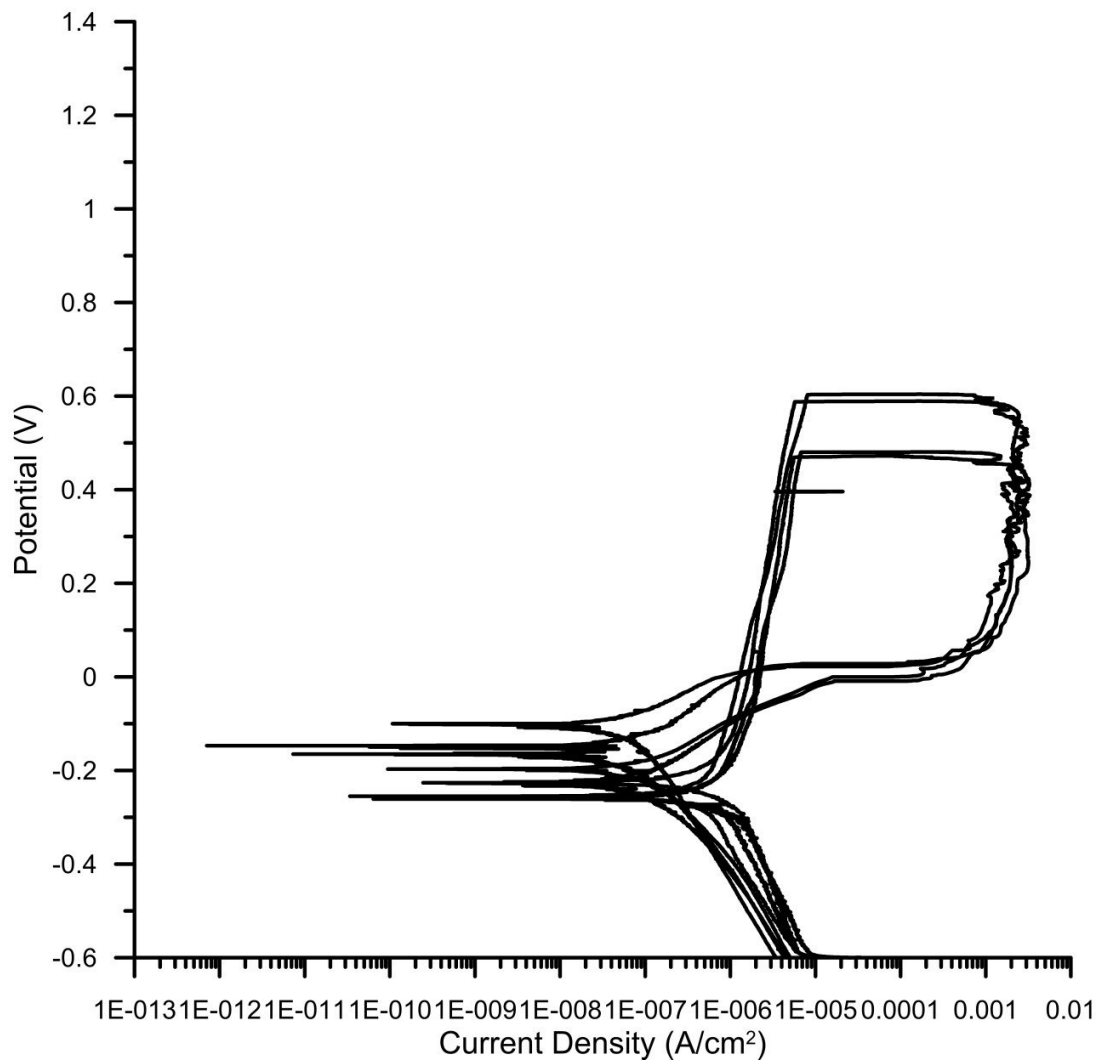


Figure A-III.4: Cyclic polarization curves for 1LPO samples 1 to 4.

Table A-III.4: Cyclic Polarization Values for 1LPO

Sample	$E_{\text{corr}}$ (V)	$i_{\text{corr}}$ ( $\mu\text{A}/\text{cm}^2$ )	$E_{\text{break}}$ (V)	$E_{\text{prot}}$ (V)	$i_{\text{prot}}$ ( $\mu\text{A}/\text{cm}^2$ )
1LPOV 1	-0.265	5.10	0.436	-0.102	6.94
1LPOV 2	-0.259	21.40	0.488	-0.029	11.71
1LPOV 3	-0.262	12.80	0.779	n/a	n/a
1LPOV 4	-0.256	8.79	0.622	n/a	n/a
Average	-0.261	12.02	0.581	-0.066	9.32
Std. Dev.	0.004	7.00	0.153	0.052	3.38



**Figure A-III.5: Cyclic polarization curves for 5LPO samples 1 to 4.**

**Table A-III.5: Cyclic Polarization Values for 5LPO**

<b>Sample</b>	<b><math>E_{\text{corr}}</math> (V)</b>	<b><math>i_{\text{corr}}</math> (<math>\mu\text{A}/\text{cm}^2</math>)</b>	<b><math>E_{\text{break}}</math> (V)</b>	<b><math>E_{\text{prot}}</math> (V)</b>	<b><math>i_{\text{prot}}</math> (<math>\mu\text{A}/\text{cm}^2</math>)</b>
5LPOV 1	-0.226	31.40	0.592	0.012	16.67
5LPOV 2	-0.259	113.00	0.469	-0.075	17.94
5LPOV 3	-0.255	46.50	0.600	-0.092	0.10
5LPOV 4	-0.259	26.30	0.479	0.017	20.63
Average	-0.250	54.30	0.535	-0.035	13.83
Std. Dev.	0.016	40.06	0.071	0.057	9.30

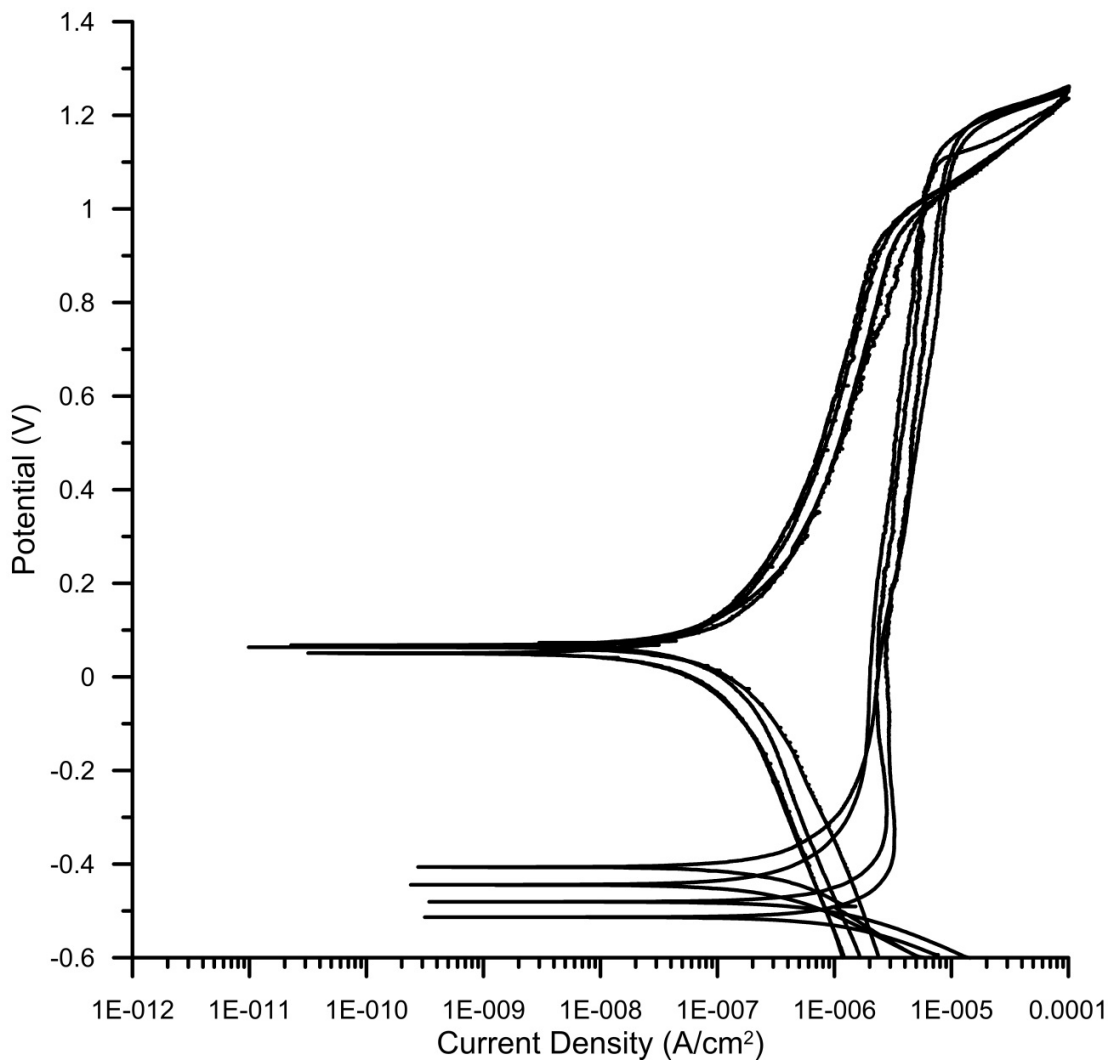


Figure A-III.6: Cyclic polarization curves for LPMP samples 1 to 4.

Table A-III.6: Cyclic Polarization Values for LPMP

Sample	$E_{\text{corr}}$ (V)	$i_{\text{corr}}$ ( $\mu\text{A}/\text{cm}^2$ )	$E_{\text{break}}$ (V)	$E_{\text{prot}}$ (V)	$i_{\text{prot}}$ ( $\mu\text{A}/\text{cm}^2$ )
LPMP 1	-0.406	1.67	1.164	1.036	9.13
LPMP 2	-0.481	2.62	1.077	1.019	5.92
LPMP 3	-0.444	1.51	1.139	1.023	5.92
LPMP 4	-0.513	2.24	1.168	1.028	8.23
Average	-0.461	2.01	1.137	1.027	7.30
Std. Dev.	0.046	0.51	0.042	0.007	1.63

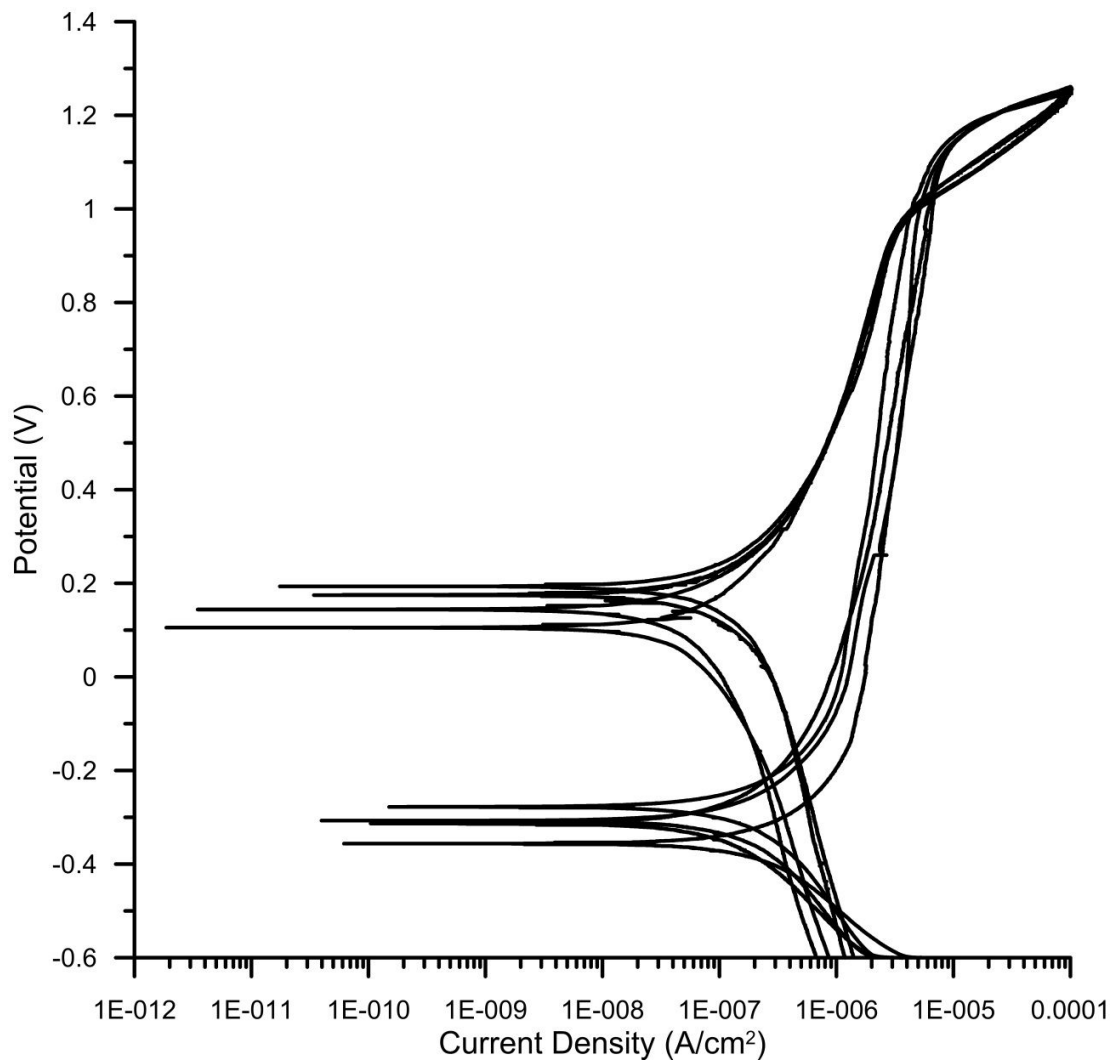


Figure A-III.7: Cyclic polarization curves for LPMPBW samples 1 to 4.

Table A-III.7: Cyclic Polarization Values for LPMPBW

Sample	$E_{\text{corr}}$ (V)	$i_{\text{corr}}$ ( $\mu\text{A}/\text{cm}^2$ )	$E_{\text{break}}$ (V)	$E_{\text{prot}}$ (V)	$i_{\text{prot}}$ ( $\mu\text{A}/\text{cm}^2$ )
LPMPBW 1	-0.278	68.90	1.156	0.982	42.44
LPMPBW 2	-0.307	23.30	1.160	1.019	53.79
LPMPBW 3	-0.313	6.76	1.168	1.032	64.42
LPMPBW 4	-0.356	16.60	1.148	1.023	68.62
Average	-0.314	28.89	1.158	1.014	57.32
Std. Dev.	0.032	27.52	0.008	0.022	11.72

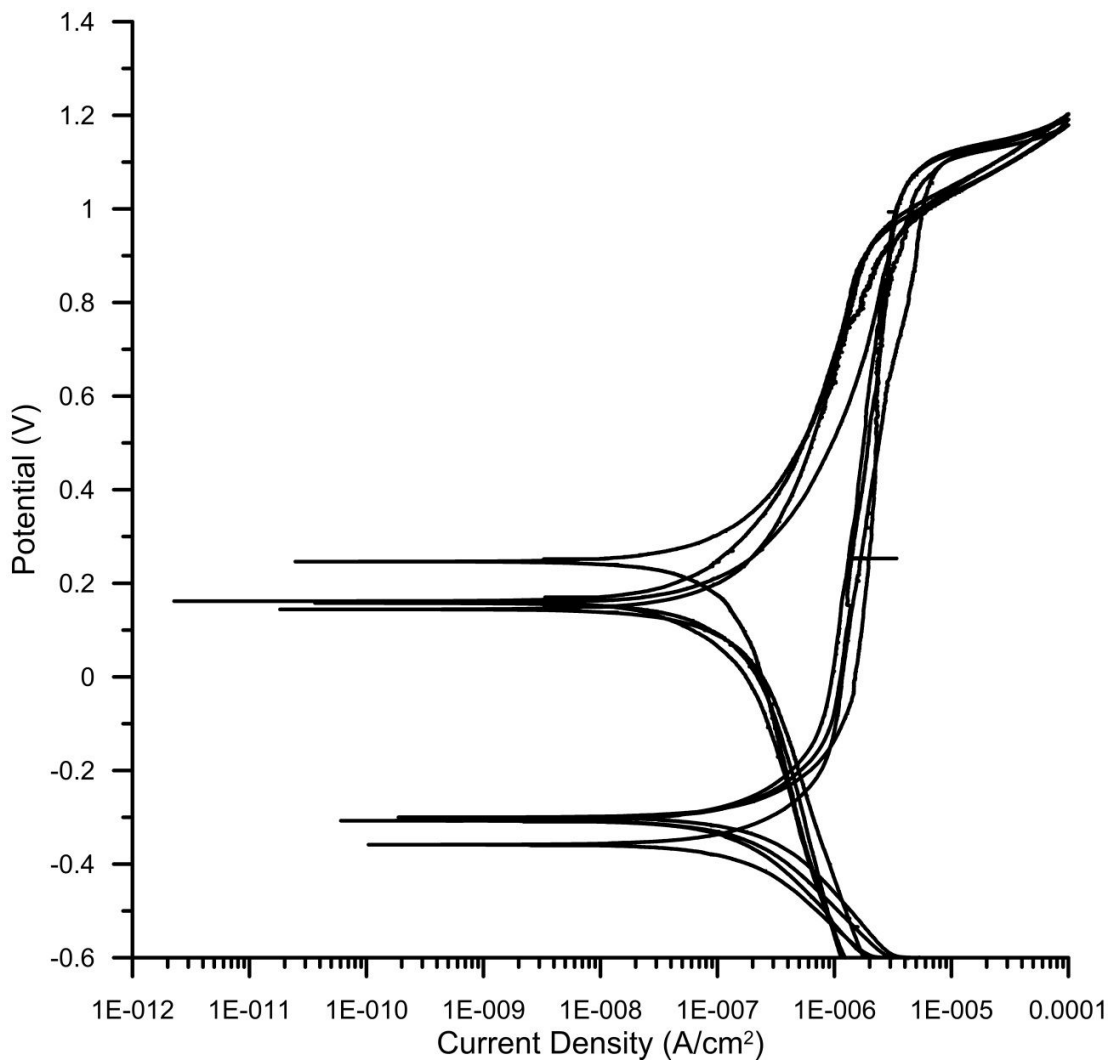


Figure A-III.8: Cyclic polarization curves for LPCE samples 1 to 4.

Table A-III.8: Cyclic Polarization Values for LPCE

Sample	$E_{\text{corr}}$ (V)	$i_{\text{corr}}$ ( $\mu\text{A}/\text{cm}^2$ )	$E_{\text{break}}$ (V)	$E_{\text{prot}}$ (V)	$i_{\text{prot}}$ ( $\mu\text{A}/\text{cm}^2$ )
LPCE 1	-0.308	19.30	1.083	0.962	31.19
LPCE 2	-0.307	12.40	1.097	0.976	32.83
LPCE 3	-0.300	30.40	1.090	0.959	41.39
LPCE 4	-0.359	8.96	1.097	0.997	57.37
Average	-0.319	17.77	1.092	0.974	40.70
Std. Dev.	0.027	9.46	0.007	0.017	11.98

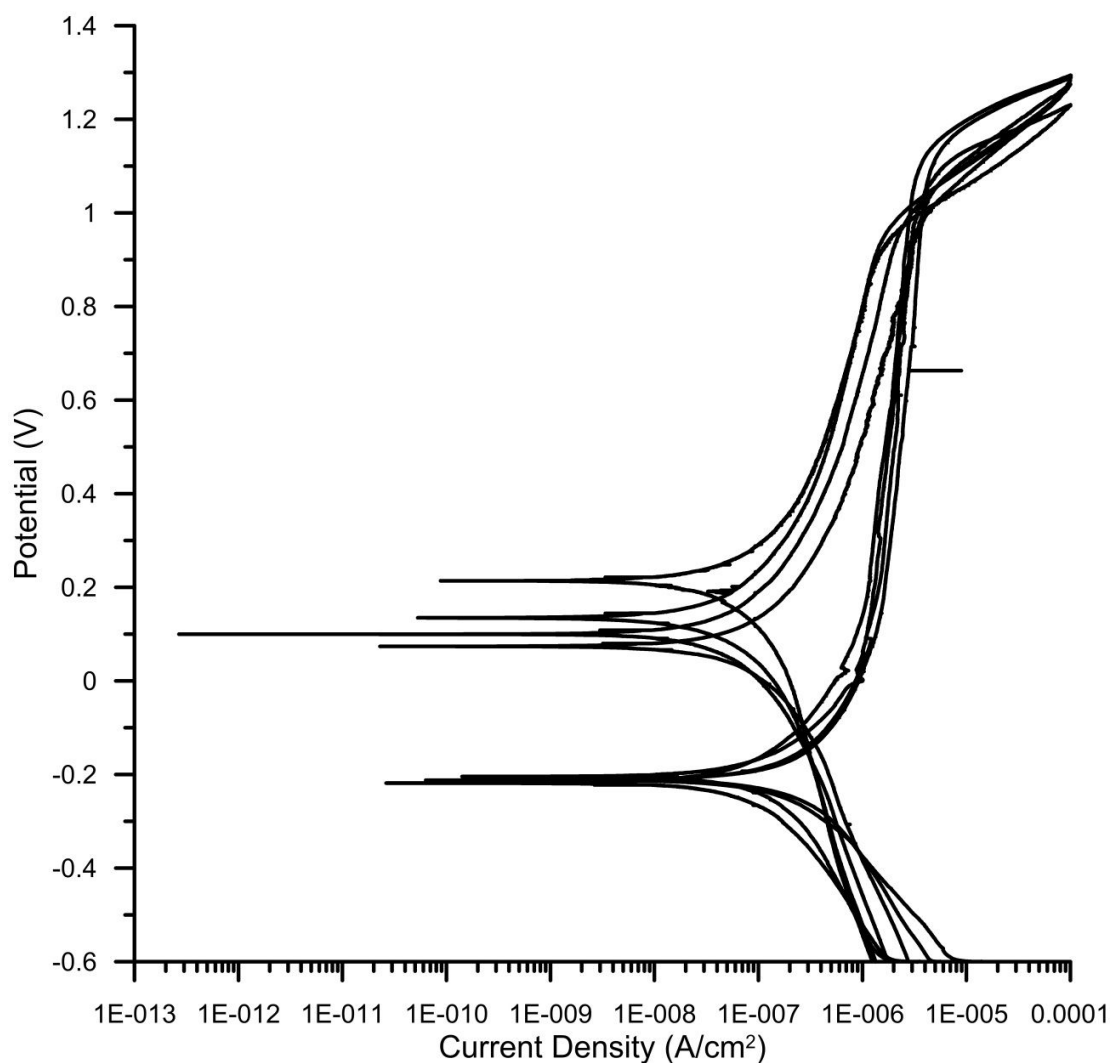


Figure A-III.9: Cyclic polarization curves for LPCEBW samples 1 to 4.

Table A-III.9: Cyclic Polarization Values for LPCEBW

Sample	$E_{\text{corr}}$ (V)	$i_{\text{corr}}$ ( $\mu\text{A}/\text{cm}^2$ )	$E_{\text{break}}$ (V)	$E_{\text{prot}}$ (V)	$i_{\text{prot}}$ ( $\mu\text{A}/\text{cm}^2$ )
LPCEBW 1	-0.211	13.70	1.168	1.028	39.17
LPCEBW 2	-0.212	8.50	1.052	0.974	35.34
LPCEBW 3	-0.204	122.00	1.090	0.995	33.53
LPCEBW 4	-0.218	12.20	1.189	1.015	29.24
Average	-0.211	39.10	1.125	1.003	34.32
Std. Dev.	0.006	55.31	0.065	0.024	4.12



## Glossary of Terms

$\alpha$	Parameter used to calculate $I_{T,con}$
$\beta$	Parameter used to calculate $I_{T,con}$
$d\sigma$	Change in critical stress to induce martensite [MPa]
$\epsilon_0$	Transformational strain [m/m]
$\Lambda$	Dimensionless substrate kinetics parameter
$\sigma$	Tensile stress [MPa]
$\sigma_m$	Stress required to induce a martensitic transformation [MPa]
$\sigma_r$	Reversible martensitic transformation stress [MPa]
$\sigma_s$	Slip stress [MPa]
$\sigma_{SIM}$	Critical stress to induce martensite [MPa]
$\tau$	Shear stress [MPa]
$A$	Exposed surface area [cm <sup>2</sup> ]
$A_f$	Austenite phase transformation finish temperature [°C]
$A_s$	Austenite phase transformation start temperature [°C]
AC	Autoclave
AC-SECM	Alternating current scanning electrochemical microscopy
ASTM	American Society for Testing and Materials
BHP	Boiling hydrogen peroxide
BW	Boiling water
C	Concentration of redox-active mediator [M]

CE	Chemically etched
CET	Chemical etching treatment
CFH	Cubic feet per hour
CP	Commercially pure
d	Distance from ME to surface [ $\mu\text{m}$ ]
dT	Change in temperature [K]
D	Diffusion coefficient of redox-active mediator [ $\text{cm}^2/\text{s}$ ]
DSC	Differential scanning calorimetry
$e^-$	Symbol representing one electron
$e_{\text{H}^+/\text{H}_2}$	Half-cell potential for hydrogen [V]
$e_{\text{M}/\text{M}^+}$	Half-cell potential for species M [V]
$E_{\text{break}}$	Potential at which passive layer destabilizes, pitting occurs [V]
$E_{\text{corr}}$	Potential at which reactions switch from cathodic to anodic [V]
$E_{\text{pp}}$	Potential at which the surface becomes passive [V]
$E_{\text{prot}}$	Potential at which the return scan crosses $i_{\text{pass}}$ and pitting should no longer occur
$E_{\text{T}}$	Working potential of ME [V]
EP	Electropolish
EW	Alloy equivalent weight
$f_i$	The mass fraction of the $i^{\text{th}}$ element in the alloy
F	Faraday's constant [ $\text{A}\cdot\text{s}/\text{mol}$ ]
FcMeOH	Ferrocenylmethanol

$\Delta G$	Free energy of formation [kJ/mol]
$\Delta H$	Latent heat of transformation [kJ/m <sup>3</sup> ]
HAZ	Heat affected zone
HPS	Hydrogen peroxide soak
HT	Heat treatment
$i$	Current density [ $\mu\text{A}/\text{cm}^2$ ]
$i_{0,\text{H}^+/\text{H}_2}$	Exchange current density equivalent to the reversible rate at equilibrium for hydrogen [ $\mu\text{A}/\text{cm}^2$ ]
$i_{0,\text{M}/\text{M}^+}$	Exchange current density equivalent to the reversible rate at equilibrium for species M [ $\mu\text{A}/\text{cm}^2$ ]
$i_{\text{corr}}$	Corrosion current density [ $\mu\text{A}/\text{cm}^2$ ]
$i_{\text{crit}}$	Critical current density achieved before passivation occurs [ $\mu\text{A}/\text{cm}^2$ ]
$i_{\text{pass}}$	Current density in the passive region [ $\mu\text{A}/\text{cm}^2$ ]
$i_{\text{prot}}$	Current density at which the return scan crosses over $i_{\text{pass}}$ [ $\mu\text{A}/\text{cm}^2$ ]
$I_{\text{corr}}$	Total anodic current [ $\mu\text{A}$ ]
$i_{\text{T}}$	Measured current at ME [nA]
$i_{\text{T},\infty}$	Current at ME tip in bulk solution [nA]
$I_{\text{T}}$	Dimensionless current at $i_{\text{T}}$
$I_{\text{T,con}}$	Theoretical positive feedback current
$I_{\text{T,ins}}$	Theoretical negative feedback current
$I_{\text{T}}^{\text{k}}$	Theoretical dimensionless current
ICP AES	Inductively coupled plasma atomic emission spectroscopy

IMC	Intermetallic compound
k	Rate constant [cm/s]
$k_{\text{eff}}$	Effective heterogeneous charge transfer rate [cm/s]
L	Normalized distance between the ME and NiTi surface
LASER	Light Amplification by Stimulated Emission of Radiation
LP	Laser processed
LPCE	Laser processed and chemically etched
LPCEBW	Laser processed, chemically etched, and boiled in water
LPMP	Laser processed and mechanically polished
LPMPBW	Laser processed, mechanically polished, and boiled in water
LPO	Laser processed overlapping
LSM	Laser surface melt
M	Representation of element being oxidized
$M_d$	Temperature at which shape memory alloy deforms through slip rather than stress-induced martensitic transformation [ $^{\circ}\text{C}$ ]
$M_f$	Martensite phase transformation finish temperature [ $^{\circ}\text{C}$ ]
$M_s$	Martensite phase transformation start temperature [ $^{\circ}\text{C}$ ]
ME	Microelectrode
MP	Mechanical polish
n	Valence number
$n_i$	The valence of the $i^{\text{th}}$ element in the alloy

N	Number of topography data points measured
Nd:YAG	Neodymium-doped yttrium aluminum garnet
NiTi	Nickel-Titanium alloy
OCP	Open circuit potential
PBS	Phosphate buffer solution
PE	Pseudoelasticity or Pseudoelastic effect
QRE	Quasi-reference electrode
$r_{\text{glass}}$	Radius of insulating borosilicate glass capillary of SECM probe tip [ $\mu\text{m}$ ]
$r_{\text{T}}$	Radius of active ME of SECM probe tip [ $\mu\text{m}$ ]
$R_{\text{a}}$	Arithmetic average of the roughness of the profile [ $\mu\text{m}$ ]
RG	Ratio of $r_{\text{glass}}$ to $r_{\text{T}}$
SECM	Scanning electrochemical microscope
SHE	Standard hydrogen electrode
SIM	Stress induced martensite
SMA	Shape memory alloy
SME	Shape memory effect
T	Temperature [K]
$W_i$	The atomic weight of the $i^{\text{th}}$ element in the alloy
XPS	X-ray photoelectron spectroscopy
XRD	X-ray diffraction
$Z_i$	Height from mean at the $i^{\text{th}}$ location [ $\mu\text{m}$ ]